

Search for Exotic Phases of Matter Through Computer Simulations

by

Youssef H. Kora

A thesis submitted in partial fulfillment of the requirements for the degree of

Doctor of Philosophy

Department of Physics
University of Alberta

© Youssef H. Kora, 2021

Abstract

The search for new phases of matter and their quantitative characterization is one of the central goals of condensed matter physics. To that end, quantum Monte Carlo is a tremendously powerful toolbox that enables the simulation of assemblies of interacting bosons, allowing the exact calculation of thermodynamic, structural, and superfluid properties. In this thesis, we utilize these techniques to carry out first-principles computations to study the phase diagrams of a diverse set of quantum many-body systems, from condensed hydrogen to superfluid helium to ultracold gases with a variety of inter-particle interactions. Within this framework, we also compute dynamical properties in imaginary time and perform analytical continuation to extract real-time information.

Preface

The entirety of this work constitutes the original thesis research of Youssef Kora, under the supervision of Professor Massimo Boninsegni.

Chapter 3 of this work has been published as Y. Kora, M. Boninsegni, D. T. Son and S. Zhang, *Proc. Natl. Acad. Sci.*, vol. 117, p. 27231, 2020.

Chapter 4 of this work has been published as Y. Kora and M. Boninsegni, *J. Low Temp. Phys.*, vol. 197, p. 337, 2019.

Chapter 5 of this work has been published as Y. Kora and M. Boninsegni, *Phys. Rev. A*, vol. 101, p. 023602, 2020.

Chapter 6 of this work has been published as Y. Kora and M. Boninsegni, *Phys. Rev. B*, vol. 98, p. 134509, 2018.

Chapter 7 of this work has been published as Y. Kora and M. Boninsegni, *Phys. Rev. B*, vol. 103, p. 014505, 2021.

All of the papers listed are collaborative works between individuals who contributed equally to the writing and research effort. The codes used were written by Dr. Boninsegni and myself.

Acknowledgements

I would foremost like to acknowledge my deep gratitude to my supervisor, Professor Massimo Boninsegni, for his mentorship, support, passion, and insight over the course of my graduate studies. I would also like to thank my committee members: Professor Joseph Maciejko, and Professor John Beamish, and my examiners: Professor Richard Sydora and Professor David Feder.

My gratitude also goes to my wife Salma Koshek for her artistic contributions, my parents Hossam Koura and Dina El-Fayoumi for their unwavering support, and my friends Ahmad El-Malky, Mostafa Gohar, and Amin El-Didi for their dedicated proof-reading.

This work was supported by the Natural Sciences and Engineering Research Council of Canada, a Simons Investigator grant (DTS) and the Simons Collaboration on Ultra-Quantum Matter, which is a grant from the Simons Foundation (651440, DTS). Computing support of Compute Canada and of the Flatiron Institute are gratefully acknowledged. The Flatiron Institute is a division of the Simons Foundation..

Table of Contents

1	Introduction	1
2	Research Methodology: Path Integral Monte Carlo	11
2.1	Path Integrals	12
2.2	Quantum Statistics	14
2.2.1	Thermal Wavelength	16
2.2.2	Permutation Sampling in Conventional PIMC	17
2.3	Worm Algorithm	18
2.4	Thermodynamic Estimators	20
2.5	Dynamical Correlations	23
3	Tuning the Quantumness of Simple Bose Systems: A Universal Phase Diagram	28
3.1	Introduction	28
3.2	Theoretical Framework	31
3.2.1	Model	31
3.2.2	Methodology	32
3.3	Results	36
3.3.1	Overview	36
3.3.2	Low Λ regime	39
3.3.3	Intermediate Λ regime	40
3.3.4	Low Λ regime	42

3.4	Conclusions	43
4	Patterned Supersolids in Dipolar Bose Systems	45
4.1	Introduction	45
4.2	Model	46
4.3	Calculation	48
4.4	Results	49
4.4.1	Phase diagram	49
4.4.2	Supersolid	51
4.4.3	Superfluid	53
4.5	Conclusions	55
5	Dipolar Bosons in One Dimension: The Case of Longitudinal Dipole Alignment	57
5.1	Introduction	57
5.2	Model	58
5.3	Calculation	61
5.4	Results	62
5.5	Conclusions	69
6	Dynamic structure factor of superfluid ^4He from quantum Monte Carlo: Maximum Entropy revisited	70
6.1	Introduction	70
6.2	Model and QMC Calculation	72
6.3	Results	73
6.4	Conclusions	81
7	Roton Excitation in Overpressurized Superfluid ^4He	83
7.1	Introduction	83
7.2	Model	84

7.3	Calculation	85
7.4	Results	89
7.5	Conclusions	93
8	Conclusions	95
	Bibliography	99

List of Tables

- 7.1 Superfluid (ρ_s) and condensate fraction (n_0), as well as the computed value of the pressure (P , in bars) for metastable superfluid ${}^4\text{He}$ at $T = 1$ K at different densities above the melting density. Statistical errors (in parentheses) are on the last digit. Also shown for comparison is the computed pressure for the equilibrium crystalline (*hcp*) phase. . . 92

List of Figures

2.1	An example of identical particle exchanges in one spatial dimension and periodic boundary conditions. The many-particle paths are periodic in the imaginary time interval $0 < u < \beta$	15
2.2	Explicit construction of a permutation of two identical particles in a conventional PIMC algorithm.	17
2.3	Example configuration in the G-sector, i.e., the configuration space associated with the single-particle Matsubara Green's function. The red lines are the closed world lines that are familiar from conventional PIMC. The blue line is the worm; an open world line with two dangling ends, referred to as Ira (I) and Masha (M).	19
2.4	The superfluid fraction $\rho_S(T)$ for ^4He at saturated vapor pressure (SVP), modeled by the Aziz potential. The results are computed using the worm algorithm for various system sizes, namely $N=64$ (filled circles), $N=128$ (open circles), $N=256$ (filled squares), $N=512$ (diamonds), $N=1024$ (triangles down), and $N=2048$ (triangles left). The solid line is the experimental result. Reproduced from Ref. [82].	21
2.5	Finite size scaling analysis for the quantity $\langle W^2 \rangle / 3 = \hbar^2 \rho_S L / m T$, for ^4He at SVP, modeled by the Aziz potential. The horizontal solid line is the known $U(1)$ universality class value for the winding number fluctuations at the critical point. Reproduced from Ref. [82].	22

2.6	Posterior probability for the regularization parameter α (top) and for the the goodness-of-fit parameter χ^2 (bottom), obtained from the Metropolis random walk in $\{\mathbf{S}, \alpha\}$ -space as described in the text. This particular result refers to the $q = 1.756 \text{ \AA}^{-1}$ wave vector in superfluid ^4He at $T = 1 \text{ K}$ and saturated vapor pressure.	27
3.1	The pressure as a function of specific volume at temperatures of 0.1 (crosses), 0.2 (squares), 0.32 (circles), 0.4 (stars), and 0.5 (diamonds). This serves as a tool for detecting coexistence between two phases of different densities, as explained in the text. This particular result is for LJ boson ^3He . Inset: Same as main graph but with a smaller P scale and only $T = 0.32$. Different symbols distinguish the superfluid phase (empty), the normal phase (filled), and the gas phase (grey).	32
3.2	The pressure-temperature phase diagram of LJ ^4He . Solid and dashed lines represent the experimentally determined phase boundaries. Solid lines correspond to first order transition, and dashed to second order.	35
3.3	Ground state and liquid-gas critical temperature of the system as a function of Λ . The liquid-gas critical temperature (T_{LG} , diamonds) is determined by the procedure discussed in Sec. 1.B and illustrated for $X = 3$ in Fig. 3.1. Also shown are the superfluid (T_λ , circles) and Bose-Einstein (T_{BEC} , boxes) transition temperatures of homogeneous fluids, as well as the melting temperatures (T_{M} , stars) of crystals. T_λ , T_{BEC} , and T_{M} are computed by holding the density fixed at the ground state equilibrium value. When not shown, statistical uncertainties are smaller than the size of the symbols. Lines are guides to the eye.	36

3.4	The ground state equilibrium density of the system as a function of the inverse de Boer parameter. The intercept at $\rho_{\text{eq}} = 0$ shows the minimum nuclear mass that remains self-bound at zero temperature; the red square is an exact result obtained from the two-body scattering length [107, 108]. Inset: examples of the equation of state at $\Lambda = 0.1815, 0.242, 0.363$, respectively from bottom to top.	37
3.5	The pressure-temperature phase diagram of LJ boson ^8He ($\Lambda = 0.09075$). The solid line, drawn as a guide to the eye, corresponds to the first order transition. The low-pressure vapor region is not visible on this scale.	39
3.6	(a) The pressure-temperature phase diagram of LJ boson ^3He ($\Lambda = 0.242$). (b) Same as (a) but with a zoom into the lower pressure portion. Lines are drawn schematically based on the discrete data points to guide the eye. Solid lines correspond to first order transition, and dashed to second order.	40
3.7	The pressure-temperature phase diagram of ^2He ($\Lambda = 0.363$). The main graph shows a zoom of the low pressure region, while the inset gives a more global view. Lines are to guide the eye. Solid lines correspond to first order phase transition, and dashed to second order.	43
4.1	(a) Ground state phase diagram of the system in the (ρ, σ) plane. Each phase is determined through simulations as explained in the text. (b) Superfluid fraction (xy plane) of the system at $\rho = 100$ and $\sigma = 0.18$ as a function of temperature, and for two system sizes.	50

4.2	Density maps of the system at density $\rho = 100$ for $\sigma = 0.12$ (a), and $\rho = 1$ for $\sigma = 0.33$ (b), integrated along the z -direction (i.e., the direction of dipole moment alignment). Brighter areas indicate higher density. The maps are obtained from particle world lines of a single configuration. In (a), the physics of the system is dominated by the potential energy, and the ground state is essentially the classical one, consisting of an array of particle-thin, parallel filaments. In (b), the ground state is a crystal of droplets with frequent quantum mechanical exchanges among adjacent droplets, leading to a finite superfluid response (as such, displaying supersolid behavior).	51
4.3	Density maps of the system at density $\rho = 100$, for $\sigma = 0.18$ (a), and $\rho = 19$, for $\sigma = 0.22$ (b), integrated along the z -direction. Brighter areas indicate higher density. These maps are obtained from particle world lines of a single configuration.	53
4.4	Elementary excitation spectra of a system of dipolar bosons for different values of the repulsive radius σ near the superfluid-supersolid transition, computed using eq. 4.6. Results shown here are for $\rho = 1$ (a) and $\rho = 100$ (b), in the low temperature limit. Statistical errors are smaller than the size of the symbols. Solid lines are fits to the data using Padé approximants, and are only meant as a guide to the eye. Insets show the corresponding in-plane static structure factor $S(q)$, averaged over all directions. In (a), yellow circles refer to $\sigma = 0.33$, for which crystal order appears, i.e., the system is in the supersolid phase. In (b), this happens at $\sigma = 0.18$	55

5.1 (a) Energy per particle $e(\rho)$ at $\sigma = 0.10$ as a function of density in the $T \rightarrow 0$ limit. Statistical errors are smaller than the size of the symbols. Solid line is a quartic fit to the data. (b) Logarithm of the negative energy per particle in the $T \rightarrow 0$ limit, as a function of σ . Circles are the results of the simulations, solid line is a fit based on eq. 5.7 (see text). 63

5.2 Ground state pair correlation functions $g(x)$ for the system at $\sigma = 0.10$ (a) and $\sigma = 0.60$ (b), each at two different system sizes N and temperatures T , at the computed equilibrium densities, namely $\rho = 17$ (0.6) for $\sigma = 0.10$ (0.60) Statistical errors are smaller than the size of the symbols. 65

5.3 (a) The static structure factor at the equilibrium density for various values of σ , in the low temperature limit. Statistical errors are smaller than the size of the symbols. (b) Example of extraction of the Luttinger parameter K based on eq. 5.6, for $\sigma = 0.26$ 66

5.4 The Tomonaga-Luttinger parameter of the system as a function of σ (a) and the equilibrium density ρ (b). The red dashed line is $K = 1$, the Tonks-Girardeau limit. Statistical errors are smaller than size of the symbols. Solid lines are guides to the eyes. 67

5.5 (a) The Tomonaga-Luttinger parameter of the system as a function of ρ for two values of $\sigma > \sigma_c$. The shaded area corresponds to the region of the phase diagram where phase coexistence occurs. The color gradient reflects the fact that the exact boundary of the green region was not precisely calculated. (b) Energy per particle $e(\rho)$ at $\sigma = 1$ as a function of the density. The shaded area corresponds to the range of densities where the system is found to feature phase coexistence. Statistical errors are smaller than size of the symbols. 68

- 6.1 Typical $F(\mathbf{q}, \tau)$ results computed in a simulation of superfluid ${}^4\text{He}$ at $T = 1$ K at density $0.021834 \text{ \AA}^{-3}$. Results shown here are for the wave vectors $q = 1.075 \text{ \AA}^{-1}$ (bottom curve), $q = 1.756 \text{ \AA}^{-1}$ (middle curve) and $q = 1.964 \text{ \AA}^{-1}$ (top curve). When not shown, statistical errors are smaller than the size of the symbols. 74
- 6.2 $S(\mathbf{q}, \omega)$ in superfluid ${}^4\text{He}$ at $T = 1$ K (at SVP) for the roton wave vector ($q = 1.963 \text{ \AA}^{-1}$), computed by inversion of QMC data based on MaxEnt (eq. 2.27, squares). Statistical errors on $S(\mathbf{q}, \omega)$ are smaller than the sizes of the symbols; the error bar on the square represents the *standard deviation* (see text), which has similar values for the two data points adjacent to the peak, and is comparable to, or smaller than, symbol sizes for all other data points. Circles show experimental data from Ref. [66] (only the coherent part is shown) at $T = 1.3$ K for the wave vector $q = 1.90 \text{ \AA}^{-1}$ 75
- 6.3 $S(\mathbf{q}, \omega)$, defined as \mathbf{S}_o (eq. 2.27) and computed as illustrated in the text, for superfluid ${}^4\text{He}$ at $T = 1$ K for the roton wave vector at SVP (diamonds, $q = 1.963 \text{ \AA}^{-1}$) and at 25 bars (circles, $q = 2.081 \text{ \AA}^{-1}$). Statistical errors on $S(\mathbf{q}, \omega)$ are comparable to the sizes of the symbols for both curves. 76
- 6.4 $S(\mathbf{q}, \omega)$ in superfluid ${}^4\text{He}$ for the roton wave vector ($q = 1.963 \text{ \AA}^{-1}$) calculated through the inversion of QMC data based on four different methods. Hexagons show the result of the inversion using MaxEnt (eq. 2.27), whereas squares show that with $\alpha = 0$ (which amounts to standard χ^2 fitting). Stars show the result of the inversion using GIFT [137] for the wave vector $q = 1.977 \text{ \AA}^{-1}$ at $T = 0$ K. Dark circles show the result of χ^2 -minimization using simulated annealing (SA) [138] for the wave vector $q = 1.91 \text{ \AA}^{-1}$ at $T = 0.8$ K. 77

6.5 $S(\mathbf{q}, \omega)$ in superfluid ${}^4\text{He}$ for the wave vector $q = 1.756 \text{ \AA}^{-1}$ calculated through the inversion of QMC data based on three different methods. Hexagons show the result of the inversion using MaxEnt (eq. 2.27). Stars show the result of the inversion using GIFT [137] for the wave vector $q = 1.755 \text{ \AA}^{-1}$ at $T = 0 \text{ K}$. Dark circles show the result of χ^2 -minimization using simulated annealing (SA) [138] for the wave vector $q = 1.76 \text{ \AA}^{-1}$ at $T = 1.2 \text{ K}$. Diamonds show experimental data from Ref. [66] (only the coherent part is shown) at $T = 1.3 \text{ K}$ for the wave vector $q = 1.70 \text{ \AA}^{-1}$ 78

6.6 $S(\mathbf{q}, \omega)$ in superfluid ${}^4\text{He}$ for the maxon wave vector ($q = 1.075 \text{ \AA}^{-1}$). Squares show the result calculated through the inversion of QMC data based on MaxEnt (eq. 2.27). Stars show the result of the inversion using GIFT [137, 145], calculated for the wave vector $q = 1.107 \text{ \AA}^{-1}$ at $T = 0 \text{ K}$. Circles show experimental data from Ref. [66] (only the coherent part is shown) at $T = 1.3 \text{ K}$ for the wave vector $q = 1.10 \text{ \AA}^{-1}$. Statistical errors are of the order of the symbol sizes. The error bar on the square data point close to the peak represents a typical standard deviation. 79

7.1 Instantaneous density map of a system of $N = 256$ ${}^4\text{He}$ atoms (view is along the z direction) in a cubic box, at $T = 1 \text{ K}$ and density 0.0336 \AA^{-3} . Clearly, in this case the system has crystallized. 87

7.2 Pair correlation function of ${}^4\text{He}$ at $T = 1 \text{ K}$ and a density of $\rho = 0.0319 \text{ \AA}^{-3}$, for both the metastable superfluid and the equilibrium (*hcp*) crystalline phase (darker curve). 88

7.3 One-body density matrix of the metastable liquid phase of ${}^4\text{He}$ at $T = 1$ K and at various increasing densities (higher density shown by lower curve). The lowest density for which results are shown is the equilibrium density, the highest (bottom curve) 0.0336 \AA^{-3} . The straight line through the peaks of the bottom curve illustrates the consistency of the data with exponential decay. 89

7.4 Condensate fraction (n_0) of the metastable liquid phase of ${}^4\text{He}$ at $T = 1$ K, as a function of density (squares). Also shown are the ground state estimates of Ref. [62] (circles). 90

7.5 The superfluid fraction of the metastable fluid phase of ${}^4\text{He}$ at $T = 1$ K, as a function of density. 91

7.6 The dynamic structure factor $S(\mathbf{q}, \omega)$ of superfluid ${}^4\text{He}$ at $T = 1$ K, evaluated at densities of ρ_{eq} ($q_R = 1.963 \text{ \AA}^{-1}$, circles), $\rho = 0.0293 \text{ \AA}^{-3}$ ($q_R = 2.159 \text{ \AA}^{-1}$, diamonds), and $\rho = 0.0319 \text{ \AA}^{-3}$ ($q_R = 2.219 \text{ \AA}^{-1}$, squares). The standard deviation associated with the inversion process is shown only for the peaks of the curves, with the understanding that the adjacent points have comparable or smaller standard deviations. 93

7.7 The roton energy of superfluid ${}^4\text{He}$ as a function of density, at $T = 1$ K. 94

Chapter 1

Introduction

One of the major themes of modern physics is the prediction of macroscopic properties and phases of thermodynamic assemblies of atoms and molecules directly from first principles. A famous quote by Weisskopf from 1977 captures the aspiration, and also underscores the challenge: “Assume that a group of intelligent theoretical physicists have lived in closed buildings from birth that they never had occasion to see natural structures... What would they be able to predict from a fundamental knowledge of quantum mechanics? They would predict the existence of atoms, of molecules, of solid crystals, both metals and insulators, of gases, but most likely not the existence of liquids.” [1]. Although Weisskopf focused on liquids, his remark highlighted the broader difficulty in treating inter-particle interactions and emergent phenomena. Interestingly, factoring in the possibility of computer simulations would almost certainly have changed this assessment. Simulations using simple models of atomic interactions allow one to make predictions of equilibrium structure and thermodynamic properties of many systems, including those of liquids.

The rapid increase of modern computing power and development of computational algorithms have greatly expanded the role of computer simulations and computation, now encompassing many subareas of physics, chemistry, materials science, etc. Despite early fears expressed, e.g., by Dirac that “the exact application of these laws leads to equations much too complicated to be soluble” [2], we are now in the

position to apply the fundamental laws of quantum mechanics to a large number of many-body systems, with precision sufficient for fruitful comparison with experiment. Of particular interest in the understanding of how quantum-mechanical effects alter the qualitative behavior of the system predicted classically. For systems obeying Fermi statistics, it is not yet possible to *systematically* reach the accuracy necessary for reliable predictions of new reactions, new structures, or new phases of matter; indeed, this remains a grand challenge. However, if the constituent particles obey Bose statistics, one has access to the exceedingly powerful toolbox of quantum Monte Carlo (QMC) simulations, which contains the most reliable tools to investigate the physics of quantum many-body systems in thermal equilibrium. In Ch. 2, we describe these methods and show how they enable us to obtain exact numerical estimates of thermodynamic averages of relevant physical observables. In the remaining chapters, we apply these methods in a series of investigations of a number of relevant physical systems that manifest a wide variety of rich physics.

A chief example of this type of condensed matter system is helium. Helium is unique among all substances, in that it does not solidify at low temperature, under the pressure of its own vapor. Its most common isotope, ^4He , undergoes a phase transition at a temperature of 2.17 K from a normal liquid to a liquid capable of flowing without dissipation (*superfluid*). Both the fact that no crystallization occurs and the superfluid transition are understood as consequences of Bose statistics [3, 4], which ^4He atoms (composite particles of zero total spin) obey. At higher temperature, ^4He shows a behavior typical of other fluids, e.g., it has a liquid-gas critical point at temperature about 5.19 K and pressure 227 kPa.

The phase diagram of ^4He is well understood owing to a wealth of experimental measurements [5, 6] and theoretical studies [7] throughout the decades. One interesting question to ask is how general some of the properties of ^4He are among Bose systems featuring the same kind of interaction, or how they might evolve with the mass of the particles and the interaction parameters, or whether new phases might

arise. In Ch. 3, we address this question through a comprehensive study of a model which allows us to not only reproduce the well-known phase diagram of ^4He , but also study a much broader class of systems in which we can tune the strength of quantum mechanical effects. This allows us to explore the evolution of the topology of the familiar pressure-temperature phase diagram of ^4He as we make the system more (and less) quantum.

On one extreme lies the classical limit, in which inter-particle interactions dominate the physics, and quantum delocalization and the exchange of identical particles are suppressed. As a consequence, these systems invariably crystallize at zero temperature. This regime is descriptive of most substances found in nature, including parahydrogen, which solidifies at a temperature of 13.8 K under the pressure of its own vapor, even in reduced dimensions [8]. As we make the system more quantum mechanical, we encounter a transition into a regime with phase diagrams that feature a liquid ground state. This is the regime in which ^4He lies, making it unique among the naturally occurring substances. Moving further in that direction leads to richer and more interesting behavior as quantum effects are further amplified. Beyond another critical point, the systems become unbound at zero temperature, and as we move further towards that extreme the system becomes increasingly descriptive of ultracold gases. This remarkably general, albeit simple model is described extensively in Ch. 3, and the results of our calculations are presented and discussed.

It is of little surprise that this broad class of systems features such a wide variety of thermodynamic phases, ranging from crystals to normal fluids to superfluids and gases. However, one phase for which we did not find any evidence at any portion of any phase diagram and at any level of quantumness, was the ever-elusive supersolid phase. As its name suggests, the supersolid is a phase of matter that features the properties of both a solid and a superfluid. In more technical terms, it is a phase that spontaneously breaks both continuous translational and global $U(1)$ symmetries, thus featuring simultaneously crystalline order and flow without dissipation (for a review

of supersolids see, for instance, Ref. [9]).

Supersolid behavior in a crystal of ^4He , once deemed the most promising candidate, has so far eluded unambiguous observation. Not only has our study in Ch. 3 reinforced the notion of the absence of a supersolid phase in ^4He , it also serves as powerful evidence of its absence in all systems featuring the same kind of interaction. In Ch. 4 we turn our attention to a class of systems that features a very different kind of interaction, namely dipolar bosons, which have been suggested as a likely physical setting for the realization of the supersolid phase in various experimental [10, 11] and theoretical [12–14] works.

Dipolar gases have been the focus of extensive experimental and theoretical research in recent times, motivated by the possibility that yet unobserved, exotic phases of matter may be underlain by the distinctive character of the inter-particle interaction, both long ranged and anisotropic [15]. In particular, the experimental achievement of Bose-Einstein Condensation of atomic systems with large magnetic moments [16–24] suggests that one might be able to predict and observe phases featuring more than one type of order. In Ref. [14], for instance, it is contended that, if dipole moments are aligned, an ordered array of filaments (or prolate droplets) constitutes the ground state of the system in rather broad conditions, and preliminary evidence of global phase coherence among such droplets was offered for specific values of density and interaction parameters.

The appearance of filaments in this system is understood to be the result of the competition between the attractive part of the dipolar interaction, and the presence of a short range repulsion which prevents the system from collapsing. Such a repulsive part is often modeled theoretically through the so-called scattering length approximation. Because the scattering length is experimentally controllable and can be varied by means of the Feshbach resonance (see, for instance, Ref. [25]), the possibility arises of exploring the quantum phase diagram of the system in its entirety, at least within known limitations (e.g., three-body recombination) [26–29]. This motivated

us to conduct a comprehensive theoretical study of the bulk phase diagram of the system at low temperature based on reliable, first principle computational methods, aimed at helping in the design and interpretation of present and future experiment.

We present this investigation in Ch. 4. We utilized QMC simulations to study the ground state phase diagram of a system of aligned dipolar bosons, and with the inclusion of a two-body repulsive potential of varying range. The system was shown to display a supersolid phase in a relatively broad region of the phase diagram, featuring different crystalline patterns depending on the density and on the range of the repulsive part of the interaction (scattering length). The supersolid phase is sandwiched between a classical crystal of parallel filaments and a homogeneous superfluid phase. We showed that a “roton” minimum appears in the elementary excitation spectrum of the superfluid as the system approaches crystallization. The predictions of this study are in quantitative agreement with experimental results.

Next, we turn our attention to lower dimensions. The system of dipolar bosons in reduced dimensions retains significant fundamental interest, at least from a theoretical perspective, and has been extensively studied in recent times [30–32]. Of particular interest is the case in 1D, as the physics of one-dimensional many-body systems has been the subject of intense theoretical investigation for decades. A number of exact solutions and/or rigorous physical statements have been obtained [33], and there exists a well-established, universal theoretical framework that describes 1D systems, known as Luttinger Liquid Theory (LLT). Considerable effort has been devoted to the realization in the laboratory of systems that may approach the 1D limit, in order to test the most important predictions of the existing theory.

Experimentally, the quasi-1D limit can be probed in different ways and/or physical settings. For example, mass flux in solid ^4He [34, 35] is speculated to be essentially one-dimensional in nature, and scenarios have been proposed to the effect that a 3D supersolid phase of ^4He may arise in a network of interconnected superfluid dislocations [36]. Alternatively, one can adsorb gases made of small atoms or molecules,

such as helium, inside carbon nanotubes [37, 38], or in porous glasses such as vycor, in which particle motion is confined to within $\sim 1 \text{ \AA}$ in two directions [39]. This has motivated theoretical studies of hardcore fluids such as ^4He [40, 41] and parahydrogen (p-H₂) [8] in strictly 1D, as well as inside a single nanotube [42–44], or in the interstitial channel of a bundle of nanotubes [45]. More recently, experimental advances in cold atom physics appear now to enable not only systematic, controllable confinement of particles, but also the tuning of the inter-particle interactions through the Feshbach resonance as mentioned above. This paves the way to the experimental validation of the existing theory, to an unprecedented degree of accuracy.

Motivated by these possibilities, we studied through QMC simulations the low-temperature phase diagram of dipolar bosons confined to one dimension, with dipole moments aligned along the direction of particle motion. As in our model in Ch. 4, we added a hardcore repulsive potential of varying range (σ) to the dipolar interaction, in order to ensure stability of the system against collapse. In the $\sigma \rightarrow 0$ limit, the physics of the system is dominated by the potential energy and the ground state is quasi-crystalline; as σ is increased, the attractive part of the interaction weakens, and the equilibrium phase evolves from quasi-crystalline to a non-superfluid liquid. At a critical value σ_c , the kinetic energy becomes dominant and the system undergoes a quantum phase transition from a self-bound liquid to a gas. In the gaseous phase with $\sigma \rightarrow \sigma_c$, at low density attractive interactions bring the system into a “weak” superfluid regime. However, gas-liquid coexistence also occurs, as a result of which no topologically protected superfluid regime is realized. Our theoretical framework and results are discussed extensively in Ch. 5.

The next problem we look at is that of analytic continuation in QMC. In principle, QMC not only provides an accurate way to study thermodynamic properties, it also allows one to obtain dynamical properties, at least within the linear response approximation. This is accomplished by computing correlation functions in imaginary time from which spectral functions can be inferred through an inverse Laplace transforma-

tion.

Unfortunately, the inversion is mathematically ill-posed, and because QMC data are inevitably affected by statistical uncertainties, an unambiguous determination of the spectral function is usually not possible. In some cases, prior knowledge about the physics of the system may constrain the set of possible solutions, allowing for a reliable reconstruction; for example, one may know that the spectral function is dominated by one or two well-defined peaks, and simply fit the QMC data accordingly (see, for instance, Ref. [46]).

In the general case, however, when no such knowledge is available, a large number of very different images will be consistent with the QMC data. Thus, one will typically resort to some kind of “regularization” scheme (RS), aimed at retaining only those images whose non-trivial structure is *truly warranted by the data*. Consequently, any RS will inevitably tend to soften some of the sharpest features; for example, distinct, isolated peaks will be broadened, to reflect the inherent uncertainty arising from the finite precision of the data and the ill-posedness of the problem.¹

A popular RS, in the context of inversion of QMC data, is the Maximum Entropy method (MaxEnt) [47, 48], which has been applied to the determination of spectral functions of various lattice many-body Hamiltonians [49–53] as well as of the dynamic structure factor in normal and superfluid ^4He [54]. In general, MaxEnt has yielded quantitatively reliable results for some of the main aspects of the reconstructed images, i.e., the positions of the peaks, and therefore the determination of the excitation spectrum; on the other hand, the quantitative accuracy of predictions concerning, e.g., the widths of the peaks, and the ensuing ability to resolve adjacent peaks, was less satisfactory, although in most cases the limiting factor was the quality of the QMC data, rather than the RS adopted to extract the images. Alternative

¹This should be regarded *not* as a limitation, but rather as a *quality* of the RS, as one ought not ascribe any physical significance to sharp, distinct features that could be spurious, in conformity with the accepted “Occam’s razor” principle; credence should be lent only to those sharp features that remain consistently robust as the quality of the underlying data improves.

RS have been proposed in the course of the years, the context of QMC simulations [55–59], displaying some advantages over others for specific applications, but no comprehensive, systematic comparison had been carried out.

In Ch. 6, we present an investigation in which we undertake that problem. We used the Maximum Entropy Method (MaxEnt) to estimate the dynamic structure factor of superfluid ^4He at $T = 1$ K, by inverting imaginary-time density correlation functions computed by quantum Monte Carlo (QMC) simulation. Our procedure consisted of a Metropolis random walk in the space of all possible spectral images, sampled from a probability density which includes the entropic prior, in the context of the so-called “classic” MaxEnt, first proposed in Ref. [54]. We also compare with recent work by other authors and show that, contrary to what is often stated, sharp features in the reconstructed image are not “washed out” by the entropic prior if the underlying QMC data have sufficient precision. Only *spurious* features that tend to appear in a straightforward χ^2 minimization are suppressed.

The success of this investigation encouraged us to utilize our methodologies to further study the dynamical properties of ^4He . In Ch. 7, we explore the behavior of the roton excitation in the overpressurized system. As mentioned above, helium is the only element in nature that does not crystallize at zero temperature under the pressure of its own vapor; instead, its thermodynamic equilibrium phase is a superfluid. A pressure of around 25 bars must be applied in order to stabilize a hexagonal closed-packed crystalline phase. It is possible, however, to realize experimentally metastable liquid phases of helium at pressures higher than that of crystallization [60, 61]. This allows one to study the superfluid response of the system over a significantly greater range of pressure.

Theoretical studies have shown that at temperature $T = 0$ the condensate fraction remains finite in the overpressurized liquid, decaying exponentially with density [62]. The predicted resilience of the overpressurized superfluid phase of ^4He is understood to be a direct consequence of quantum-mechanical exchanges involving a macroscopic

fraction of all particles in the system (an effect also referred to as "quantum jamming") [4].

Of particular interest is whether superfluidity persists all the way to the limit of existence of a metastable overpressurized fluid. This limit is identified by a value of density, referred to as *spinodal*, above which only the crystalline phase occurs. It is speculated that the energy of the minimum of the excitation spectrum of superfluid ^4He at finite wave vector, known as the *roton*, should vanish at the spinodal density [63, 64].

The roton energy as a function of pressure has been measured experimentally in the equilibrium fluid phase up to a pressure of 20 bars [65–67], as well as in various porous media, in which the fluid phase can be stabilized above the bulk freezing pressure, as crystallization is suppressed by the tight confinement [68]. The highest pressure at which superfluidity has been observed in porous media is ~ 37 bars, where the roton mode disappears [69, 70]. However, no measurement of the roton energy in the overpressurized bulk superfluid, which has been predicted to exist at much higher pressures, has to our knowledge been carried out yet.

Besides the outstanding theoretical issue mentioned above, namely the behavior of the roton energy on approaching the spinodal, the parallel behavior of the superfluid and condensate fraction at finite temperature, as a function of pressure, is also of interest; there have been ground state studies of the condensate fraction of overpressurized superfluid ^4He , but it is known that the superfluid fraction must be equal to 100% in the ground state of a translationally invariant system [71]. Furthermore, since the excitation spectrum can be probed by neutron scattering measurements, knowledge of the roton energy as a function of density and pressure can be used to gain information about the local environment experienced by the fluid in confinement or in restricted geometries.

We therefore carried out a theoretical investigation of overpressurized superfluid phases of ^4He by means of quantum Monte Carlo (QMC) simulations, which we

present in Ch. 7. As a function of density, we study structural and superfluid properties, and estimate the energy of the roton excitation by inverting imaginary-time density correlation functions computed by QMC, using Maximum Entropy. We estimate the pressure at which the roton energy vanishes to be about 100 bars, which we identify with the spinodal density, i.e., the upper limit for the existence of a metastable superfluid phase.

Chapter 2

Research Methodology: Path Integral Monte Carlo

In this chapter, we describe the research methodology utilized in this thesis, and the computational approach we use to carry out the calculations.

In the investigations presented here, we are interested in systems that are modeled as collections of point-like Bose particles. Each of these systems is described by a quantum-mechanical many-body Hamiltonian that is, in general, quite intractable analytically, due to the strength of the interactions between the particles.

Our method of choice is Path Integral Monte Carlo (PIMC), which casts the problem in such a way that we may rely on the help of the computer to solve it. This allows for direct, first principle, numerically exact calculation of the physical quantities of interest such as thermodynamic properties, structural correlations, superfluid properties, and even dynamical properties to a certain extent.

This method equips us with the ability to make such computations at *finite* temperature, in an arbitrary number of dimensions, and with an accuracy that may be rendered arbitrarily small in an amount of time that grows *polynomially* with the number of particles. These luxuries are not afforded by alternative numerical approaches, which are either limited to i) small system sizes, such as exact diagonalization, ii) zero temperature, such as variational wave methods involving a trial wave function [72], or iii) lower dimensions, such as the Density Matrix Renormalization Group [73].

In the coming subsections, we describe the details of the method, and the computational approaches and algorithms it entails.

2.1 Path Integrals

We start by recalling the basic formalism of quantum statistical mechanics. For a system of a fixed number of particles N in thermal equilibrium with a reservoir at temperature T , the thermal expectation value of a physical observable A is given by

$$\langle \hat{A} \rangle = \frac{\text{Tr}(\hat{A}\hat{\rho})}{\text{Tr}(\hat{\rho})} = \frac{\int dR dR' A(R)\rho(R, R', \beta)}{\int dR \rho(R, R, \beta)} \quad (2.1)$$

where we have expressed the traces in coordinate representation, with $R \equiv \mathbf{r}_1\mathbf{r}_2\dots\mathbf{r}_N$, i.e., the collective positions of all N particles in the configuration, and $\beta = 1/T$ (in units where the Boltzmann constant, k_B , is set to unity). The many-body density matrix, $\rho(R, R, \beta)$, is given by

$$\rho(R, R', \beta) = \langle R | e^{-\beta\hat{H}} | R' \rangle \quad (2.2)$$

where \hat{H} is the quantum-mechanical many-body Hamiltonian describing the system. The denominator of eq. 2.1 is the partition function Z .

The problem of calculating the RHS of eq. 2.1 often amounts to knowledge of the density matrix $\rho(R, R, \beta)$, which is in general inaccessible except for the simplest systems. The method of path integration, a formulation of quantum mechanics first introduced by Feynman [74], enables us to circumvent this problem by constructing the so-called Euclidean action, defined as

$$S[R(\tau)] = \int_0^{\beta\hbar} d\tau \left(\sum_{i=1}^N \frac{m}{2\hbar^2} \left(\frac{d\mathbf{r}_i}{d\tau} \right)^2 + V(R(\tau)) \right) \quad (2.3)$$

where m is the mass of the particles, \hbar is the Planck constant, and the new variable τ is defined as the imaginary time coordinate. The first term represents the kinetic energy, related to path curvature, and the second represents the potential energy

along the path, which is determined by the inter-particle interactions. This allows one to express the partition function as

$$Z \propto \int DR(\tau) e^{-S[R(\tau)]} \quad (2.4)$$

where the functional integral sums over all possible β -periodic N -particle paths starting (and ending) at all possible many-body configurations. Each path $R(\tau)$ may therefore be attributed a probability proportional to the generalized Boltzmann factors $\exp\{-S[R(\tau)]\}$ and sampled through the well-known Metropolis Algorithm [75]. This allows one to evaluate eq. 2.1 as statistical averages along these paths.

The first step in the numerical approach is to discretize the continuous action integral in eq. 2.3. The continuous many particle path is therefore only considered at M discrete time slices, i.e., $R(\tau) \equiv \{R_0, R_1, \dots, R_{M-1}\}$, with $R_M = PR_0$ to respect the β -periodicity (P denotes permutations of particle labels). The finite time step $\delta\tau = \beta/M$ results in an inevitable error, which may be rendered arbitrarily small by appropriate choice of $\delta\tau$. This allows us to approximate the discretized action as

$$S[R(\tau)] \approx \sum_{i=1}^N \sum_{l=0}^{M-1} \frac{m(\mathbf{r}_{il} - \mathbf{r}_{il+1})^2}{2\delta\tau\hbar^2} + \delta\tau \sum_l V(R_l) \quad (2.5)$$

We may now sample the discrete paths $R(\tau)$ from the probability distribution

$$P \propto e^{-S[R(\tau)]} = \prod_{i=1}^N \prod_{l=0}^{M-1} \rho_0(\mathbf{r}_{il}, \mathbf{r}_{il+1}, \delta\tau) \prod_{l=0}^{M-1} e^{-U(R_l, \delta\tau)} \quad (2.6)$$

where ρ_0 denotes the free-particle density matrix [76], given by

$$\rho_0(\mathbf{r}_{il}, \mathbf{r}_{il+1}, \delta\tau) = \left(\frac{2\pi\hbar^2\delta\tau}{m} \right)^{-d/2} \exp \left[-\frac{m(\mathbf{r} - \mathbf{r}')^2}{2\hbar^2\delta\tau} \right] \quad (2.7)$$

where d is the dimensionality of space, and

$$U(R_l, \delta\tau) = \delta\tau V(R_l) \quad (2.8)$$

in the simplest approximation, i.e., the potential energy does not depend on the time step. For reasons of computational efficiency, it is often desirable to work with a more

accurate approximation for the density matrix. In most of the work presented in this thesis, we utilize the so-called fourth-order approximation for the high-temperature density matrix (see, for instance, Ref. [77]), which has the form

$$\rho_4(R_l, R_{l+1}, \delta\tau) = A_F(R_l, R_{l+1}, \delta\tau) e^{-\tilde{U}(R_l, \delta\tau)} \quad (2.9)$$

where

$$A_F(R, R', \delta\tau) = \prod_{i=1}^N \rho_0(\mathbf{r}_i, \mathbf{r}'_i, \delta\tau) \quad (2.10)$$

$$\tilde{U}(R_l, \delta\tau) = \delta\tau \left[\frac{2V(R_l)}{3} + \tilde{V}(R_l, \delta\tau) \right] \quad (2.11)$$

and

$$\tilde{V}(R_l, \delta\tau) = \frac{2V(R_l)}{3} + \frac{\delta\tau^2}{9m} \sum_{i=1}^N (\nabla_i V(R_l))^2 \quad (2.12)$$

if l is odd, and zero if l is even. $\nabla_i V(R_l)$ is the gradient of the total potential energy for the configuration R with respect to the position of the i th particle. This expression has been shown [78, 79] to be accurate up to terms of order $\delta\tau^4$, hence the name.

2.2 Quantum Statistics

Next, we discuss how quantum statistics and the intrinsic indistinguishability of particles is incorporated into the formalism. As mentioned in Sec. 2.1, the paths are periodic in imaginary time with period β , which means that the configuration $R(\beta = M\delta\tau)$ must have the particles in the same positions as the configuration $R(0)$. However, since the particles are identical, they must be allowed to trade places with each other throughout the period $0 < \tau < \beta$ as long as there are particles at the correct positions at imaginary time $\tau = \beta$. An example is shown in Fig. 2.1, which shows the exchange of four particles in one spatial dimension. In this case, exchanges may only occur through periodic boundary conditions assuming that the particles experience hardcore repulsion at short distances.

This exchange of identical particles in imaginary time is the mechanism through which quantum statistics manifests itself in the physical picture, thereby causing

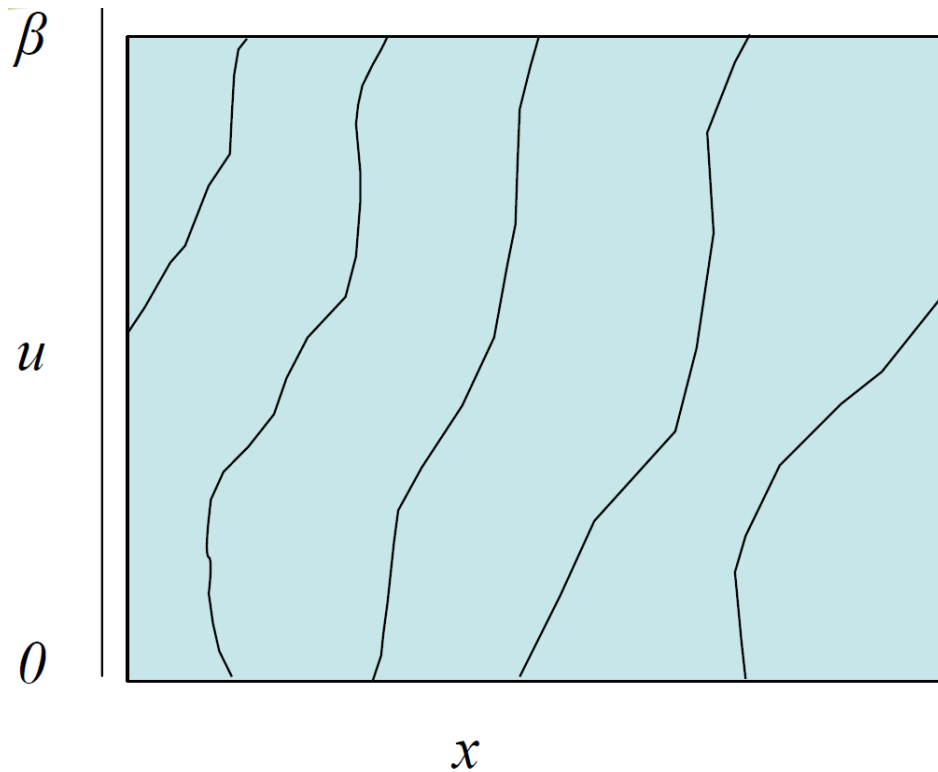


Figure 2.1: An example of identical particle exchanges in one spatial dimension and periodic boundary conditions. The many-particle paths are periodic in the imaginary time interval $0 < u < \beta$.

these systems to behave in a dramatically different way, depending on whether the constituent particles obey Bose or Fermi statistics. It is this essential piece of microscopic physics that gives rise to macroscopic phenomena such as Bose-Einstein condensation and superfluidity in the case of Bose systems.

Incorporating quantum statistics, we may write the thermal expectation value of our physical observable as

$$\langle \hat{A} \rangle \sim \frac{\sum_{paths} \eta^P A(R_{path})}{\sum_{paths} \eta^P} \quad (2.13)$$

where P is the parity of permutation associated with particle exchange, $A(R_{path})$ is the average of the observable \hat{A} computed along the path, and η is $+1$ (-1) for bosons (fermions).

In the case of Fermi statistics, the sums over paths in eq. 2.13 become alternating series of terms which very nearly cancel each other out [76]. Attempting to associate

amplitudes with probabilities in this case causes these series to become exponentially intractable to sum as a function of N and β . This is the well-known Fermi sign problem that makes this method unsuitable to study systems comprising more than a few fermions at a temperature that is not unreasonably high.

On the other hand, systems obeying Bose statistics are not plagued by this problem, as all terms in the sums in eq. 2.13 are strictly non-negative. Only Bose systems are investigated in this work, and therefore we will not further discuss the Fermi sign problem.

2.2.1 Thermal Wavelength

Quantum statistics become important only at low temperature. At sufficiently high temperature, exchanges between particles in imaginary time are inhibited, allowing them to retain their individuality and behave as distinguishable Boltzmannons. One criterion to quantify the importance of exchanges relies on the so-called thermal wavelength, defined as

$$\lambda_T = \frac{\hbar}{\sqrt{mT}} \quad (2.14)$$

which characterizes the “size” of a typical single particle path in imaginary time. In physical terms, it may be thought of as a measure of the quantum mechanical delocalization of a typical particle (in a free system). Exchanges are important when λ_T is of the order of the inter-particle distance $n^{-1/d}$. This criterion is satisfied below the temperature $T_0 \sim \hbar^2 n^{2/d}/m$, commonly known as the degeneracy temperature. As the temperature of the system approaches and falls below T_0 , quantum statistics becomes increasingly essential to the physics. Sufficiently above T_0 , on the other hand, the particle clouds do not experience significant overlap, the identity permutation dominates, and the quantum statistics of the system becomes irrelevant. Since we are often interested in the low temperature physics, it is essential to be able to reliably sample permutations of identical particles.

2.2.2 Permutation Sampling in Conventional PIMC

We now describe the permutation sampling protocol in conventional PIMC [7]. It is essentially achieved through explicit construction, by sampling moves which modify portions of the single particle paths to accomplish the exchange as shown in Fig. 2.2. It is easy to see why this procedure, which requires sampling paths in which the

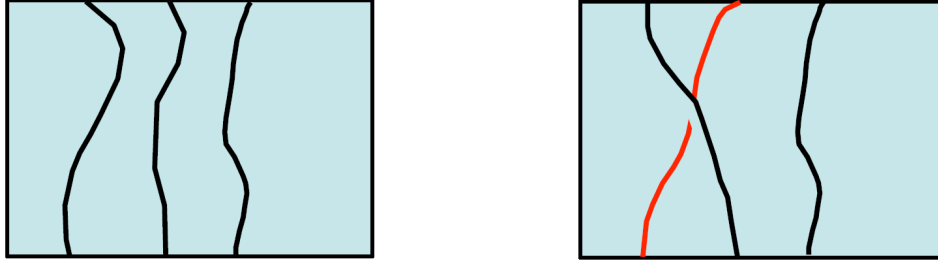


Figure 2.2: Explicit construction of a permutation of two identical particles in a conventional PIMC algorithm.

particles are brought in close proximity to one another as shown in Fig. 2.2, can be highly inefficient. The vast majority of naturally occurring atomic systems feature hardcore repulsion between the constituent atoms, due to the Pauli exclusion principle preventing the overlap of the electronics clouds surrounding the atoms. This leads to a high probability of rejection according to eq. 2.6, and the computational effort required to sample macroscopic permutation cycles scales exponentially with the number of particles.

As mentioned in Sec. 2.2, quantum statistics underlies essential macroscopic phenomena such as Bose-Einstein condensation and superfluidity. The efficient sampling of macroscopic permutation cycles is therefore crucial to the simulation of the low temperature physics of these systems. The superfluid fraction, for instance, is directly related to the winding of paths through the boundaries of the system [80]. It is therefore essential that we are able to sample paths which have a finite winding number around the space, i.e., paths which contain permutations of $\sim N^{1/d}$ particles. This becomes a macroscopic number of particles when attempting to extrapolate to

the thermodynamic limit, and thus the exponential scaling of the effort to sample permutation cycles presents a serious challenge for conventional PIMC. This is one of the main issues which the Worm Algorithm addresses.

2.3 Worm Algorithm

The worm algorithm deals with the permutation cycle sampling problem that plagues conventional PIMC in a remarkable way. The configuration space is generalized from that of the partition function (henceforth referred to as the Z-sector), which contains only closed paths as shown in Figs. 2.1 and 2.2), to that of the one-particle Matsubara Green's function (henceforth referred to as the G-sector), defined as

$$G(\mathbf{r}_1, \mathbf{r}_2, \tau) = \frac{g(\mathbf{r}_1, \mathbf{r}_2, \tau)}{Z} = -\langle \hat{T}[\hat{\psi}(\mathbf{r}_1, \tau)\hat{\psi}^\dagger(\mathbf{r}_2, 0)] \rangle \quad (2.15)$$

where ψ^\dagger and ψ are Bose field operators, \hat{T} is the time ordering operator, and $-\beta \leq \tau \leq \beta$. An example of such a configuration is shown in Fig. 2.3, which contains not only the familiar closed world lines, but also an open world line with two dangling ends, referred to in the literature as Ira (I) and Masha (M).

Expanding the space of configurations to include those corresponding to the G-sector allows us to accomplish non-trivial topological modifications to the world lines that facilitate the sampling of longer permutation cycles, while avoiding the problems that plague conventional PIMC, described in subsection 2.2.2. This is achieved through a series of ergodic and complementary local path updates, the details of which are extensively described in Refs. [81, 82].

Since the worm algorithm allows the accumulation of statistics for both diagonal and off-diagonal correlations simultaneously, it enables the efficient computation of many relevant physical quantities that are not only limited to the energetics and thermodynamics, but also quantities such as superfluid density, structural correlations, and even dynamical correlations to a certain extent. We come back to this in the coming sections.

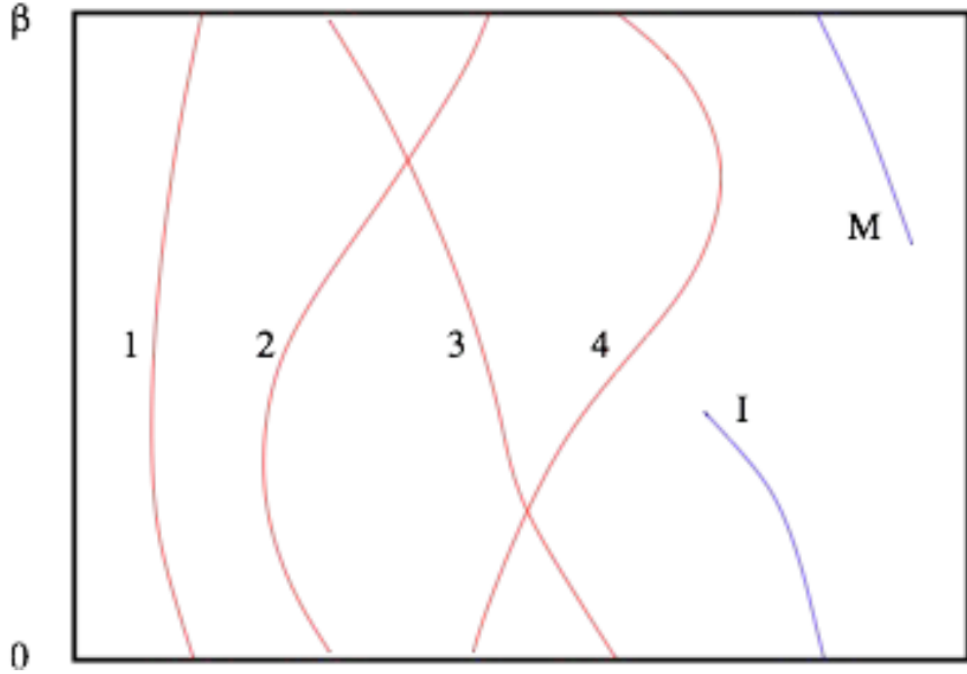


Figure 2.3: Example configuration in the G-sector, i.e., the configuration space associated with the single-particle Matsubara Green’s function. The red lines are the closed world lines that are familiar from conventional PIMC. The blue line is the worm; an open world line with two dangling ends, referred to as Ira (I) and Masha (M).

Another advantage of the worm algorithm is clear upon taking the $\tau \rightarrow 0$ limit of eq. 2.15. In this limit, the Matsubara Green’s function reduces to the one-particle density matrix $n(\mathbf{r}_1, \mathbf{r}_2)$, which is the Fourier transform of the momentum distribution $\tilde{n}(\mathbf{k})$. In a Bose condensed system, $\tilde{n}(\mathbf{k})$ has the form

$$\tilde{n}(\mathbf{k}) = n_0 \delta(\mathbf{k}) + \tilde{n}_{NC}(\mathbf{k}) \quad (2.16)$$

where n_0 denotes the condensate fraction, and $\tilde{n}_{NC}(\mathbf{k})$ refers to the fraction of particles outside of the condensate. In this way, the worm algorithm allows for the inference of the condensate fraction through the computation of off-diagonal correlations in the G-sector.

Versatility is yet another advantage of the worm algorithm. The protocol is not only well-suited in the context of the canonical ensemble, but also in the grand canonical ensemble, where the introduction of a worm facilitates the creation and annihilation

of world lines to reflect fluctuations in the particle number. For the remainder of this thesis, however, we will focus on applications of the worm algorithm in the canonical ensemble, where the number of world lines is constrained to N in the Z-sector (and $N - 1$ and a single worm in the G-sector) in order to study the system at fixed density [83, 84].

2.4 Thermodynamic Estimators

Equipped with the tools described in the previous sections, we are in position to compute thermal expectations values of the quantities of interest as statistical averages over the spacetime configurations generated by the worm algorithm. In this section, we provide examples of some thermodynamic estimators derived in Ref. [79].

The average kinetic energy per particle may be estimated as

$$\langle K \rangle \approx \frac{\hbar}{2\delta\tau} - \frac{1}{4\lambda\delta\tau^2} \langle (\mathbf{r}_l - \mathbf{r}_{l+1})^2 \rangle + \frac{\lambda\delta\tau^2}{9} \langle (\nabla V(R_{2l}))^2 \rangle \quad (2.17)$$

where $\lambda = \hbar^2/2m$, $\langle \dots \rangle$ represents the statistical average along the imaginary time path, $(\mathbf{r}_l - \mathbf{r}_{l+1})^2$ is the square of the distance between two the positions of a particle at adjacent points along the world line, and the gradient of the potential energy in the last term is taken with respect to one of the particles at an even time slice. The potential energy per particle is simply estimated as

$$\langle V \rangle \approx \frac{1}{N} \langle V(R_{2l-1}) \rangle \quad (2.18)$$

Eqs. 2.17 and 2.18 are both approximations that become exact in the $\delta\tau \rightarrow 0$ limit.

The superfluid fraction is computed directly through the well-established winding number estimator, which considers the change in the free energy of the fluid in response to the uniform motion of the boundary [80]. This yields the expression

$$\frac{\rho_s}{\rho} = \frac{\langle W^2 \rangle mT}{3\hbar^2 \rho L} \quad (2.19)$$

where $\mathbf{W} = (W_x, W_y, W_z)$ is the winding number, and L is the system size. It is worth noting that the superfluid fraction is susceptible to finite size effects that are

increasingly prominent as one approaches the critical point, as shown in the example in Fig. 2.4, and thus an extrapolation procedure is required for a precise estimation of the critical temperature for the superfluid transition.

The finite size scaling analysis is performed on $\langle W^2 \rangle / 3$, since it is proportional to

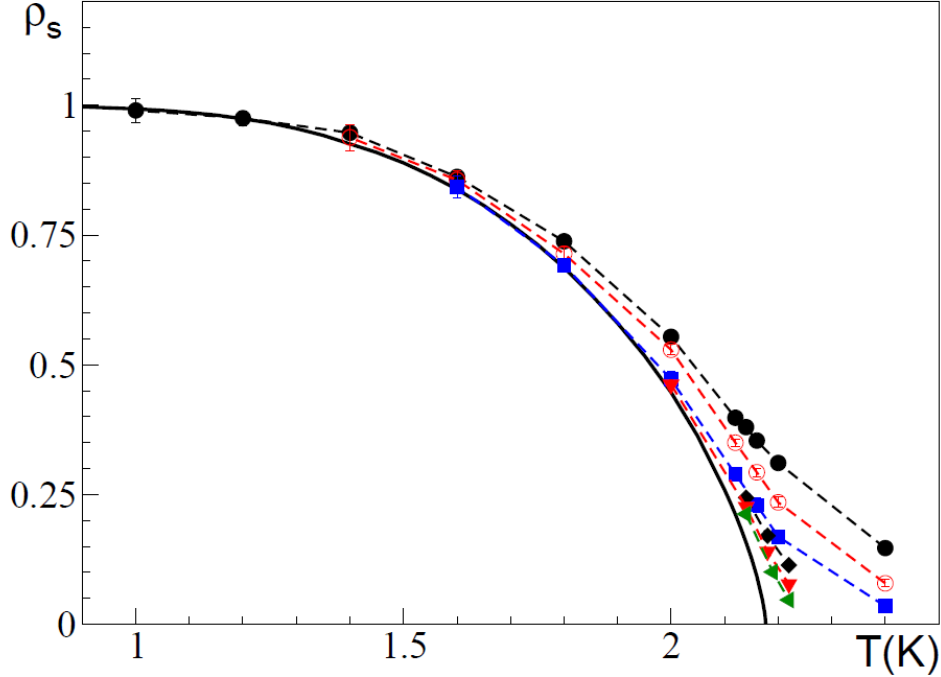


Figure 2.4: The superfluid fraction $\rho_s(T)$ for ${}^4\text{He}$ at saturated vapor pressure (SVP), modeled by the Aziz potential. The results are computed using the worm algorithm for various system sizes, namely $N=64$ (filled circles), $N=128$ (open circles), $N=256$ (filled squares), $N=512$ (diamonds), $N=1024$ (triangles down), and $N=2048$ (triangles left). The solid line is the experimental result. Reproduced from Ref. [82].

the quantity $\rho_s L / mT$, which becomes scale invariant at the critical point [82]. An example of this analysis is shown in Fig. 2.5, in which studying the intersection of these scaling curves yields a fairly precise estimate of the critical temperature of ${}^4\text{He}$ at saturated vapor pressure, modeled using the Aziz potential.

We may also estimate the standard errors on these quantities. Since any expectation value of a physical observable A we compute is a statistical average over configurations X_l generated at M time slices, it is bound to deviate from, and fluctuate around, the true mean of the Gaussian that is approached in the $M \rightarrow \infty$ limit.

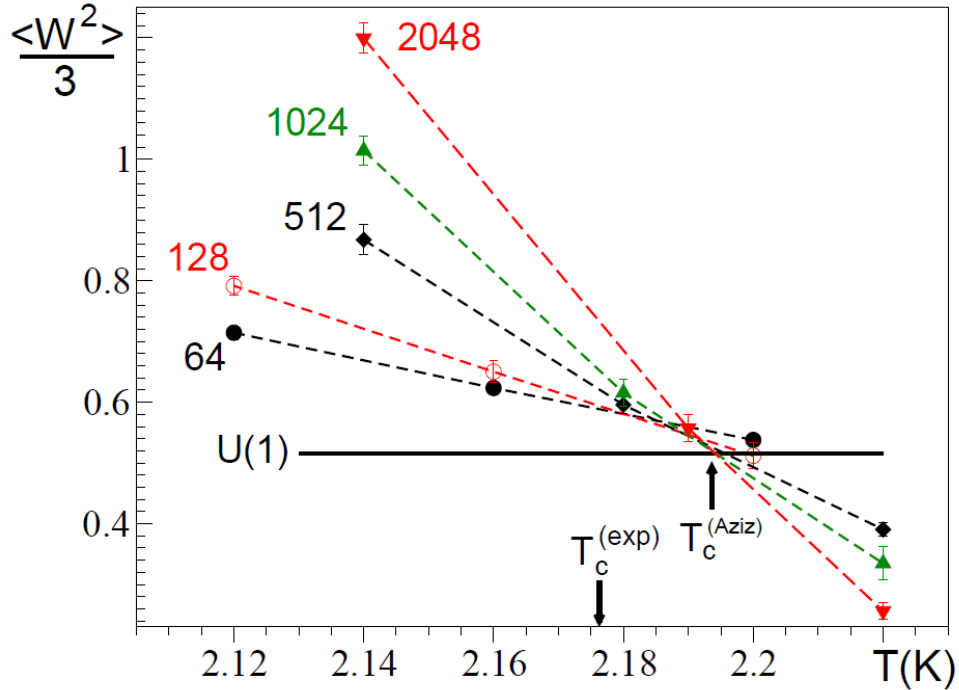


Figure 2.5: Finite size scaling analysis for the quantity $\langle W^2 \rangle / 3 = \hbar^2 \rho_S L / mT$, for ${}^4\text{He}$ at SVP, modeled by the Aziz potential. The horizontal solid line is the known U(1) universality class value for the winding number fluctuations at the critical point. Reproduced from Ref. [82].

The most straightforward estimate of these fluctuations is given by

$$\Delta A = \sqrt{\frac{\sum_{l=1}^M (A(X_l) - \langle A \rangle)^2}{M(M-1)}} \quad (2.20)$$

In general, eq. 2.20 yields an underestimate of the true error, since the configurations X_l are not statistically independent. A more accurate estimate of the error requires that we reduce the autocorrelations between the configurations, which may be accomplished by binning the data and computing averages over these smaller sets of configurations (which would constitute a set of averages that are less correlated than the original data set), and then computing the standard error using this new set of averages.

2.5 Dynamical Correlations

As mentioned in Sec. 2.3, it is also possible to compute dynamical properties (in the linear response regime) within our framework, despite the system being in thermal equilibrium. One such quantity of interest is the dynamic structure factor $S(\mathbf{q}, \omega)$, which describes density fluctuations of wave vector \mathbf{q} . For superfluid ^4He it has been extensively studied experimentally by neutron scattering (for a review, see, for instance, Ref. [70]). It is a direct probe of the elementary excitations (phonons and rotons) that underlie the physical behavior of the system at low temperature [85–87]. $S(\mathbf{q}, \omega)$ is a non-negative function satisfying the relation [88]

$$\langle \omega \rangle = \int_0^\infty d\omega \omega S(\mathbf{q}, \omega) (1 - e^{-\beta\omega}) = \frac{q^2}{2m} \quad (2.21)$$

known as f -sum rule (for the remainder of this section we set $\hbar = 1$).

There is no known QMC scheme allowing for the *direct* calculation of $S(\mathbf{q}, \omega)$. However, it can be shown (see, for instance, Ref. [54]) that

$$F(\mathbf{q}, \tau) = \int_0^\infty d\omega (e^{-\omega\tau} + e^{-\omega(\beta-\tau)}) S(\mathbf{q}, \omega) \quad (2.22)$$

where $0 \leq \tau \leq \beta$ and $F(\mathbf{q}, \tau)$ is the imaginary-time auto-correlation function

$$F(\mathbf{q}, \tau) = \frac{1}{N} \langle \hat{\rho}_{\mathbf{q}}(\tau) \hat{\rho}_{\mathbf{q}}^\dagger(0) \rangle \quad (2.23)$$

with

$$\rho_{\mathbf{q}}(\tau) = \sum_{j=1}^N e^{i\mathbf{q}\cdot\mathbf{r}_j}, \quad (2.24)$$

where the $\{\mathbf{r}_j\}$, $j = 1, 2, \dots, N$ are the positions of the N particles at imaginary time τ along the many-particle path. The quantity $F(\mathbf{q}, \tau)$ is what is actually computed by QMC, for a discrete set of values of τ ; $S(\mathbf{q}, \omega)$ is inferred from $F(\mathbf{q}, \tau)$ through a numerical inversion of eq. 2.22.

The problem with such an inversion lies in the fact that the integral kernel exponentially suppresses the contribution at high frequency of the spectral function to

$F(\mathbf{q}, \tau)$; consequently, $F(\mathbf{q}, \tau)$ is minimally affected by the high frequency behavior of $S(\mathbf{q}, \omega)$. Because $F(\mathbf{q}, \tau)$ is the result of QMC simulations, and therefore possesses finite statistical uncertainties, there will be typically a large set of physically different spectral functions consistent with the numerical data for $F(\mathbf{q}, \tau)$. Most of these solutions are unphysical and/or bear little resemblance to the actual $S(\mathbf{q}, \omega)$. The goal is that of finding a systematic and robust way to weed out spurious solutions, and retaining only a relatively small subset of physical ones, from which at least the most important physical features of $S(\mathbf{q}, \omega)$ may be reliably extracted.

As mentioned above, $F(\mathbf{q}, \tau)$ is computed for the discrete set of imaginary times $l\delta\tau$, $l = 0, 1, \dots, L$, with $2L\delta\tau = \beta$. In order to simplify the notation, for a given value of \mathbf{q} we define $\mathbf{F} \equiv \{F_0, \dots, F_L\}$, with $F_l \equiv F(\mathbf{q}, l\delta\tau)$. Each entry F_l is affected by a statistical uncertainty σ_l , estimated by careful binning analyses of data (see, for instance, Ref. [89]) collected over sufficiently long simulations. We begin by approximating the integral on the right hand side of eq. 2.22 with a sum, i.e., turn eq. 2.22 into a system of algebraic equations that can be expressed in compact matrix form

$$\mathbf{F} = \mathbf{KS}, \quad (2.25)$$

having defined

$$K_{lj} = [e^{-jl\delta\omega\delta\tau} + e^{-j(2L-l)\delta\omega\delta\tau}] \delta\omega, \quad (2.26)$$

$\mathbf{S} \equiv \{S_1, \dots, S_M\}$, $S_j \equiv S(\mathbf{q}, j\delta\omega)$, and $M\delta\omega = \omega_M$, ω_M chosen large enough that $S(\mathbf{q}, \omega)$ can be set to zero for $\omega > \omega_M$, and $\delta\omega$ small enough to achieve the desired frequency resolution. In the studies presented in this thesis, ω_M is between 100 and 300 K, whereas M is between 150 and 400. An important observation is that typically $M > L$, i.e., the system (2.25) is underdetermined, and therefore, in general, no unique solution can be found, quite irrespective of the ill-posedness of the problem and of statistical errors of the computed imaginary-time correlation functions.¹

¹As mentioned in the text, the value of the time step utilized in the QMC calculation is $\epsilon = 1/640$ K⁻¹. There are therefore 320 “time slices” in the imaginary-time interval $0 \leq \tau \leq \beta/2$, but because

We take the same approach as in Ref. [54], based on “classic” MaxEnt (see, for instance, Ref. [48]) and define our “optimal” solution as

$$\mathbf{S}_o \equiv \int d\alpha \int DS \mathbf{S} \mathcal{F}(\alpha, \mathbf{S}) \quad (2.27)$$

where $DS \equiv dS_1 dS_2 \dots dS_M$, and

$$\mathcal{F}(\alpha, \mathbf{S}) = \frac{e^{-\chi^2(\mathbf{S})/2}}{Z_Q} \frac{e^{\alpha \mathcal{S}(\mathbf{S})}}{Z_S(\alpha)} \rho(\mathbf{S}) \quad (2.28)$$

is a prior probability assigned to the generic image \mathbf{S} . Here, α is a non-negative regularization parameter, to which we come back below; Z_Q and $Z_S(\alpha) \propto \alpha^{-M/2}$ are normalization constants;

$$\chi^2(\mathbf{S}') = (\mathbf{F} - \mathbf{F}')^T \mathbf{C}^{-1} (\mathbf{F} - \mathbf{F}') \quad (2.29)$$

is the standard measure of goodness of fit, with $\mathbf{F}' = \mathbf{K}\mathbf{S}'$ and we make the diagonal approximation² for the covariance matrix \mathbf{C} , i.e.,

$$C_{ij} = \sigma_i^2 \delta_{ij}, \quad (2.30)$$

and

$$\mathcal{S}(\mathbf{S}) = - \sum_{i=1}^M f_i \ln(M f_i), \quad (2.31)$$

with $f_i = S_i / (\sum_j S_j)$, is Jaynes’ entropy³ of the image \mathbf{S} [90]; and finally,

$$\rho(\mathbf{S}) \propto \exp\left(-\frac{[\langle \omega \rangle - \omega_{\mathbf{q}}]^2}{2\eta^2 \omega_{\mathbf{q}}^2}\right) \quad (2.32)$$

where $\langle \omega \rangle$ is defined in eq. 2.21, $\omega_{\mathbf{q}} = q^2 / (2m)$ and η is adjusted to enforce that relation (2.21) be satisfied to the desired degree of accuracy (typically $\eta \leq 0.01$).

the fourth-order formula is adopted, only half of them are usable for computation of expectation values of observables. For details, see, for instance, Ref. [79]

²In principle, the diagonal approximation for C is not justified, because QMC data at different imaginary-times are not generated independently, i.e., they are correlated. However, the diagonal approximation often allows for a more stable inversion, and in practice the use of the full covariance matrix does not yield any significant difference in the results. See, for instance, Ref. [54].

³Implicit in the definition (2.31) is the use of a “flat” default model, i.e., one making no *a priori* assumption on the shape of S .

The prior probability (2.28) ascribes greater weight to those spectral functions that are consistent with the data, and therefore have a low value of χ^2 and fulfill the f -sum rule, while at the same time are smoother in character. In other words, sharp features such as isolated peaks should *not* be included unless consistency with the data requires it.

The parameter α can be used to “tune” the relative importance of the entropic prior in $\mathcal{F}(\mathbf{S})$; in the limit $\alpha \rightarrow 0$, one is performing conventional χ^2 -fitting; on the other hand, as α grows the entropic prior becomes increasingly important. The question arises of how to choose the value of α . In “historic” MaxEnt, one adjusts α so that on average, the value of $\chi^2 \sim L$. As mentioned above, we adopt the “classic” MaxEnt approach, in which α is treated as a random variable, and assigned a prior probability distribution $p(\alpha)$, which is incorporated in the normalization constant $Z_S(\alpha)$.

We evaluate the multidimensional integral in eq. 2.27 by Monte Carlo, just as in Ref. [54]. Specifically, we perform a random walk in $\{\mathbf{S}, \alpha\}$ -space, using the Metropolis algorithm to sample the probability density given by eq. 2.28. We achieve that through few elementary moves, designed to satisfy the usual detailed balance condition. Specifically, we randomly attempt either one of the following:

1. the displacement of an elementary amount of area, equal to $\gamma \delta S$, where $0 \leq \gamma \leq 1$ is a uniform random number, from a randomly selected channel j to another one, randomly selected among $j - p, \dots, j - 1, j + 1, \dots, j + p$.
2. the addition or subtraction of $\gamma \delta S'$ from a randomly selected channel j .
3. the change of α by an amount $(1/2 - \gamma) \delta \alpha$.

Proposed moves are accepted or rejected based on the usual Metropolis test, making use of eq. 2.28 in the acceptance ratio.⁴ The parameters δS , $\delta S'$, $\delta \alpha$ and p are adjusted to ensure a 50% acceptance rate. The move attempting to change the value

⁴Obviously, moves attempting to make any of S_j or α negative are automatically rejected.

of α is typically attempted every $\sim M$ attempts to perform either one of the first two moves.

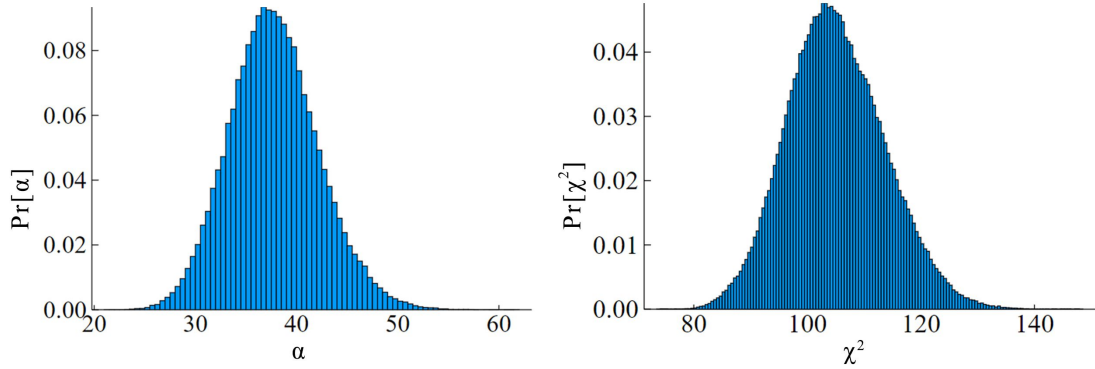


Figure 2.6: Posterior probability for the regularization parameter α (top) and for the the goodness-of-fit parameter χ^2 (bottom), obtained from the Metropolis random walk in $\{\mathbf{S}, \alpha\}$ -space as described in the text. This particular result refers to the $q = 1.756 \text{ \AA}^{-1}$ wave vector in superfluid ^4He at $T = 1 \text{ K}$ and saturated vapor pressure.

The posterior probability of α , $Pr[\alpha]$, as well as the χ^2 distribution $Pr[\chi^2]$, are obtained from the random walk, just as in Ref. [54]. Fig. 2.6 shows a typical result.

The optimal image \mathbf{S}_o (eq. 2.27), determined as an average over the images generated in the random walk, is affected by a statistical error, that can be estimated in the standard way and can be rendered sufficiently small upon using a relatively modest amount of CPU time. More significant, however, given the inherent uncertainty of the inversion, is the *standard deviation* associated with the fluctuation of the values S_i around their averages; we report them in Ch. 6 along with some example results of these calculations.

Chapter 3

Tuning the Quantumness of Simple Bose Systems: A Universal Phase Diagram

3.1 Introduction

We begin our journey by considering a category of systems whose main characteristics are *simplicity* and *generality*. This broad class of condensed matter systems is well described by pair-wise, central interactions among constituent particles (e.g., atoms), featuring *a*) a strong repulsion at short inter-particle separations (from Pauli exclusion principle, acting to prevent electrons from different atomic or molecular clouds from overlapping spatially) and *b*) a weak attractive tail at long distances, arising from mutually induced electric dipole moments. A widely used approximate model to describe such an interaction is the Lennard-Jones (LJ) potential:

$$V_{LJ}(r) = 4\epsilon \left[\left(\frac{\sigma}{r} \right)^{12} - \left(\frac{\sigma}{r} \right)^6 \right], \quad (3.1)$$

where ϵ is the depth of the attractive well, σ is the characteristic range of the interaction, and r is the separation between the two particles. Despite its simplicity, the LJ potential effectively accounts for the physical behavior of a large number of simple liquids, such as the well-characterized ^4He .

The challenge we undertake in this chapter is that of generalizing our understanding of the properties of ^4He to a wider class of Bose systems featuring the same kind

of interaction. Specifically, we are interested in how the behavior of these system might evolve as we control the strength of quantum mechanical effects by tuning the parameters of our model, such as the mass of the particles. One might ask, for instance, what the phase diagrams of the various (bosonic) isotopes of helium might look like, and how they would connect to the well-known phase diagram of ^4He .

A theoretical description of a system of interacting bosons based on the LJ potential constitutes a simple but remarkably general framework in which such questions can be addressed. On taking ϵ (σ) as our unit of energy (length), the Hamiltonian is fully parametrized by the dimensionless parameter¹

$$\Lambda = \frac{\hbar^2}{m\epsilon\sigma^2}, \quad (3.2)$$

whose magnitude expresses the relative importance of the kinetic and potential energies. The larger the value of Λ , the more significant the quantum effects in the dynamics of the particles, and the higher the temperature to which they can be expected to persist. Conversely, in the $\Lambda \rightarrow 0$ limit, the potential energy dominates, and the behavior of the system is largely classical.

In order to make this argument more quantitative, we note that for ^4He , $\epsilon \equiv \epsilon_{\text{He}} = 10.22\text{ K}$ and $\sigma \equiv \sigma_{\text{He}} = 2.556\text{ \AA}$, i.e., $\Lambda = 0.18$, which is the second highest value among naturally occurring substances (the highest being 0.24 for the lighter helium isotope, ^3He , a fermion). For comparison, for a fluid of parahydrogen molecules, i.e., spin-zero bosons of mass one half of that of a ^4He atom, $\epsilon = 34.16\text{ K}$ and $\sigma = 2.96\text{ \AA}$, yielding $\Lambda = 0.08$. In stark contrast to helium, fluid parahydrogen crystallizes at a temperature $T=13.8\text{ K}$, well above that at which Bose-Einstein condensation might take place. Although quantum effects are observable [92] near melting, there is no evidence of a superfluid phase, even in reduced dimensions, where quantum effects are amplified [93].

One might wonder what the phase diagram may be if Λ should be significantly

¹The Λ parameter used here is proportional to the square of the well-known de Boer parameter [91].

greater than the helium value of ~ 0.2 . This may seem like a purely academic question, given that helium is an “outlier” among naturally occurring substances. However, there are avenues that may allow experimental realizations of LJ Bose systems with larger Λ values. Confined assemblies of ultracold atoms, in which the interaction can be “tuned” by means of techniques such as the Feshbach resonance (see, for instance, Ref. [25]), may provide a test for some of the predictions, at least in the low density limit.

Moreover, there are intriguing possibilities with exotic atoms, in which one or more electrons are replaced by other subatomic particles of the same charge, such as muons [94]; recently, a long-lived “pionic helium” has been created [95]. A more radical approach consists of replacing *all* electrons [96, 97]; for example, a “muonic” version of a given element of mass M has an equivalent mass M_{eq} given by [98]

$$M_{eq} = \left(1 + \frac{Z m_\mu}{A m_N}\right) \frac{m_e}{m_\mu} M \quad (3.3)$$

where m_μ and m_e are the masses of the muon and the electron respectively. The replacement of electrons by muons causes *a*) a shrinkage of the range (σ) of the interparticle potential by a factor of m_μ/m_e (~ 200) and *b*) an increase in the well depth (ϵ) by the same factor, resulting in a 200-fold increase of Λ — sufficient to bring even systems made of heavier elements, e.g., Ne, whose condensed phase displays essentially classical physical behavior, into the highly quantum regime.

In this chapter, we present a comprehensive study of the universal phase diagram of LJ Bose systems. We used state-of-the-art quantum Monte Carlo (QMC) methods to compute numerically exact thermodynamic averages of relevant physical observables at finite temperatures. Given the presence of both strong interactions and large quantum effects in these systems, systematically accurate many-body computations are crucial for reliable predictions. We mapped out the complete thermodynamic phase diagram as a function of pressure and temperature, varying the parameter Λ to explore a variety of physical regimes ranging from almost entirely classical, to the

ultra-quantum.

The remainder of this chapter is organized as follows: in Sec. 3.2 we describe the model of the system, and briefly summarize the methodology we utilized. In Sec. 3.3, we present and discuss our results in several subsections separated by the different regimes of Λ , and we finally outline our conclusions in Sec. 3.4.

3.2 Theoretical Framework

3.2.1 Model

We consider an ensemble of N identical particles of mass m obeying Bose statistics, enclosed in a cubic box of volume V , with periodic boundary conditions in the three directions. The density of the system is therefore $\rho = N/V$. Particles interact via the LJ potential. As mentioned in Sec. 3.1, we take the characteristic length σ as our unit of length, and the well depth ϵ as that of energy. The dimensionless quantum-mechanical many-body Hamiltonian reads as follows:

$$\hat{H} = -\frac{1}{2}\Lambda \sum_i^N \nabla_i^2 + 4 \sum_{i<j}^N \left(\frac{1}{r_{ij}^{12}} - \frac{1}{r_{ij}^6} \right), \quad (3.4)$$

where the first (second) sum runs over all particles (pairs of particles), and $r_{ij} \equiv |\mathbf{r}_i - \mathbf{r}_j|$ is the distance between particles i and j . In these reduced units, Λ is the only parameter of the Hamiltonian, and therefore, its numerical value univocally determines the nature of its equilibrium phase, at any values of pressure and temperature.

In discussing our results, we shall at times find it useful to refer to a particular system, not in terms of its value of Λ , but rather of its “equivalent helium mass” X , defined as the mass of a hypothetical helium isotope (^XHe , always assumed to be a boson) which yields the same value of Λ . That is, a system of mass M characterized

by LJ interaction parameters of ϵ and σ has

$$X = M \frac{\epsilon}{\epsilon_{\text{He}}} \left(\frac{\sigma}{\sigma_{\text{He}}} \right)^2. \quad (3.5)$$

Thus, the mathematical description of the system can also be equivalently parametrized in terms of X , instead of Λ .

3.2.2 Methodology

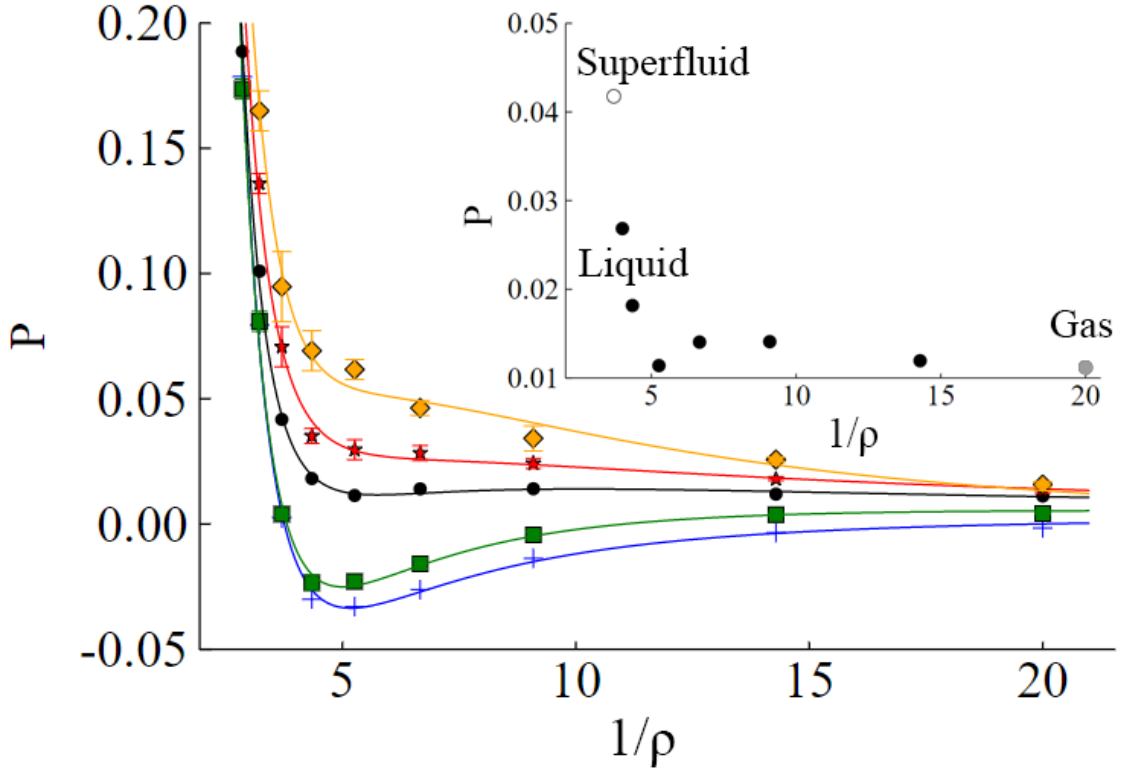


Figure 3.1: The pressure as a function of specific volume at temperatures of 0.1 (crosses), 0.2 (squares), 0.32 (circles), 0.4 (stars), and 0.5 (diamonds). This serves as a tool for detecting coexistence between two phases of different densities, as explained in the text. This particular result is for LJ boson ${}^3\text{He}$. Inset: Same as main graph but with a smaller P scale and only $T = 0.32$. Different symbols distinguish the superfluid phase (empty), the normal phase (filled), and the gas phase (grey).

As mentioned above, we carry out systematic many-body calculations of the system described in subsection 3.2.1 using QMC simulations. Specifically, we make use of the well-established continuous-space worm algorithm described in Ch. 2.

Note that, while there has been considerable simulation work on classical LJ fluids, previous work on quantum systems has been mostly limited to variational ground state studies [99, 100]. Indeed, the pioneering simulations of the superfluid transition in ^4He were based on a more accurate interatomic pair potential [7, 80]. Finite temperature QMC simulations of LJ systems have also been performed of solids, in which quantum statistics is neglected [101, 102] on account of the relative infrequency of quantum exchanges.

Although our technique is based on the finite-temperature path-integral technique [76], the ground state physics is explored by reaching sufficiently low T so that the results can be regarded as essentially for the ground state. Once the low-temperature limit is reached, the equation of state of the system is calculated by computing the energy as a function of density, and the minimum of this function is taken to be the equilibrium density, i.e., the density at which the self-bound system exists at $T = 0$. As mentioned in subsection 3.2.1, the finite temperature physics is readily accessible upon raising the temperature T , and the over(under)-pressurized system is explored by raising (lowering) the density ρ . The value of the pressure at any given T and ρ is calculated through the virial theorem (see, for instance, Ref. [103]). In this fashion, one may survey the pressure-temperature phase diagram of the system and explore the different phases thereof.

We performed simulations for values of the equivalent helium mass $1 \leq X \leq 8$. Details of the simulation are standard; we made use of the fourth-order approximation for the high-temperature density matrix (see Ch. 2), and all of the results quoted here are extrapolated to the limit of time step $\delta\tau \rightarrow 0$.

Superfluid order is detected through the direct calculation of the superfluid fraction through the well-established winding number estimator described in Ch. 2. The superfluid transition temperature is estimated by performing finite size scaling analysis of the results for the superfluid fraction, as demonstrated in Sec. 2.4. We obtained estimates for systems comprising a number of particles ranging from $N = 32$ to

$N = 512$. Crystalline order in the system is detected through i) visual inspection of the imaginary-time paths and ii) the calculation of the pair-correlation function. For computational convenience, we simulated all crystalline phases assuming a body-centered cubic structure. It is known that the energy difference between that and the hexagonal close-packed, in which, e.g., ${}^4\text{He}$ crystallizes under pressure, is small (less than 0.02ϵ in ${}^3\text{He}$ [104]).

The liquid-gas critical temperature is inferred indirectly, through the computation of the pressure as a function of volume at different temperatures. By definition, the critical temperature is the highest temperature for which there is coexistence between the liquid and gas phases, which has the signature of a flat region in the pressure-volume isotherm. This behavior, however, only occurs in an infinite system. In the case of finite systems accessible to numerical simulations, in which separation into two coexisting phases is energetically unfavorable, this behavior is reflected by the system acquiring negative compressibility, i.e., the isotherm showing positive slope in the coexistence region [105]. By plotting isotherms at different temperatures, one can identify the liquid-gas critical temperature as the highest temperature for which there is evidence of coexistence. This is illustrated in Fig. 3.1 with an example.

As a first gauge of the accuracy and reliability of our approach, we study ${}^4\text{He}$ (i.e., $\Lambda = 0.1815$). The topology of the P - T phase diagram of ${}^4\text{He}$ is well-known [5–7], with which we can compare our results. Although most microscopic calculations [7] of helium utilize the more accurate Aziz pair potential [106], the LJ potential is known to give an excellent approximation in ${}^4\text{He}$. Additionally, three-body terms have been shown [104] to account for a relatively small correction to the thermodynamic equation of state, with insignificant effect on structural or superfluid properties. Comparing our results for $X=4$ against experimental phase boundaries, as shown in Fig. 3.2, thus serves as validation for our methodology.

This phase diagram features two critical temperatures: i) the superfluid transition

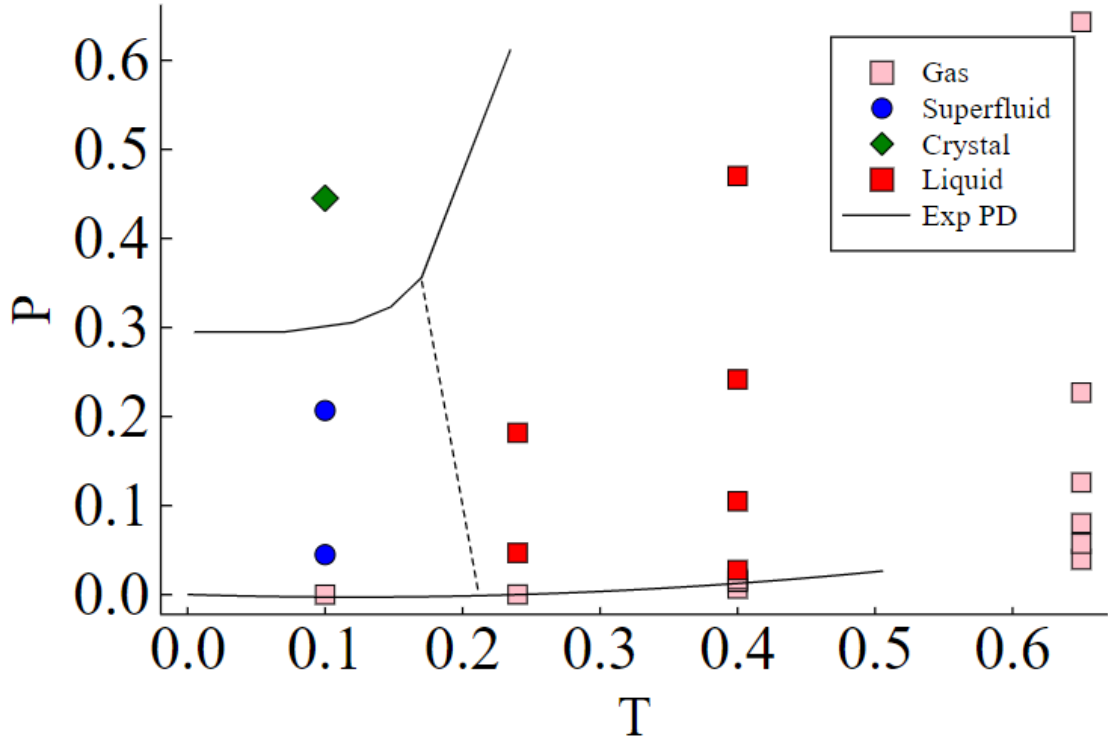


Figure 3.2: The pressure-temperature phase diagram of LJ ⁴He. Solid and dashed lines represent the experimentally determined phase boundaries. Solid lines correspond to first order transition, and dashed to second order.

temperature T_λ , and ii) the temperature that marks the end of the liquid-gas coexistence line T_{LG} , i.e., the highest temperature at which there is a phase transition between a liquid phase and a gas phase. Clearly, $T_{LG} > T_\lambda$ in this case. However, as one continues to lower the value of the mass, one expects i) quantum-mechanical effects to become more prominent, thus enhancing superfluidity and raising the value of T_λ , and ii) zero-point motion to increasingly dominate the potential energy, causing the system to become less bound and suppressing the liquid phase, causing T_{LG} to go down.

We systematically investigate these trends in Sec. 3.3.

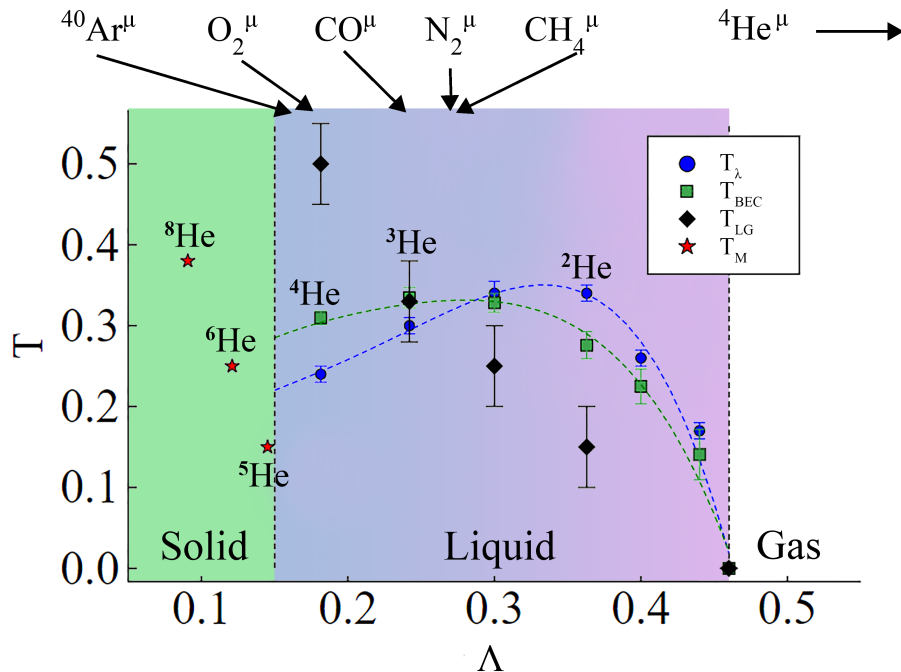


Figure 3.3: Ground state and liquid-gas critical temperature of the system as a function of Λ . The liquid-gas critical temperature (T_{LG} , diamonds) is determined by the procedure discussed in Sec. 1.B and illustrated for $X = 3$ in Fig. 3.1. Also shown are the superfluid (T_{λ} , circles) and Bose-Einstein (T_{BEC} , boxes) transition temperatures of homogeneous fluids, as well as the melting temperatures (T_{M} , stars). T_{λ} , T_{BEC} , and T_{M} are computed by holding the density fixed at the ground state equilibrium value. When not shown, statistical uncertainties are smaller than the size of the symbols. Lines are guides to the eye.

3.3 Results

3.3.1 Overview

The results of our extensive QMC computations are summarized in Fig. 3.3. In this subsection, we discuss the main ground state features of this diagram and give a brief overview of the different physical regimes at zero temperature, before moving on to describe finite temperature characteristics. The various transition temperatures in Fig. 3.3 were computed at specific values of Λ . The corresponding equivalent helium mass X values are also shown in the figure. We indicate with arrows the locations the muonic counterparts of some molecules.

The different shades in Fig. 3.3 represent the different ground states of the system,

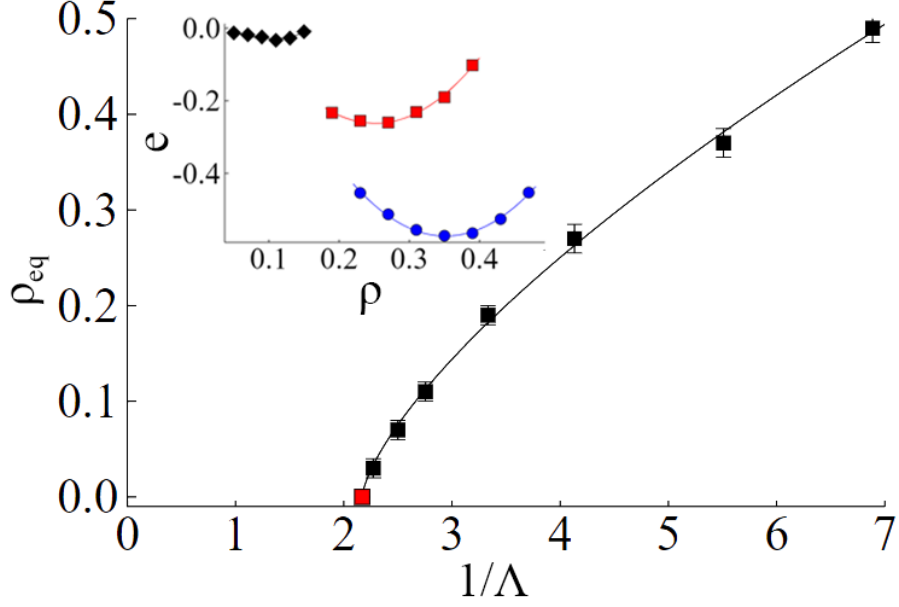


Figure 3.4: The ground state equilibrium density of the system as a function of the inverse de Boer parameter. The intercept at $\rho_{\text{eq}} = 0$ shows the minimum nuclear mass that remains self-bound at zero temperature; the red square is an exact result obtained from the two-body scattering length [107, 108]. Inset: examples of the equation of state at $\Lambda = 0.1815, 0.242, 0.363$, respectively from bottom to top.

depending on the value of Λ . Three distinct physical regimes can be identified. At low values of Λ (high values of the nuclear mass), the ground state is a crystal. At a value of $\Lambda \approx 0.15$, the system quantum melts into a superfluid that remains self-bound. As Λ is further increased, the binding is weakened. This behavior is illustrated in Fig. 3.4, which shows the equilibrium density going down as Λ grows, to finally hit zero upon reaching another critical value Λ_c , whereupon the system undergoes quantum unbinding. In the regime $\Lambda > \Lambda_c$, the ground state is a superfluid gas.

From the many-body equation of state results, we obtain an estimate of $\Lambda_c \approx 0.46$ as shown in Fig. 3.4, which corresponds to $X \approx 1.6$. This result agrees with an earlier prediction made in Ref. [108] using the zeros of the two-body scattering length [107], confirming the argument based on few-body considerations. In the series expansion of the effective potential in terms of a classical field, the three-body term has the opposite sign with respect to the two-body term, as we approach Λ_c from below. We

can also compute the three-body scattering hypervolume D , related to the three-body coefficient $\lambda_3/3$ by $\hbar^2 D/6m = \lambda_3/3$. Our estimate is obtained by fitting the energy as a function of density at a value (chosen to be $\Lambda = 0.44$) close to Λ_c with a third degree polynomial and extracting the value of the coefficient of the cubic term. This gives $D/\sigma^4 = 57 \pm 8$, which is again consistent with the estimates made from few-body calculations in Refs. [108, 109].

The finite-temperature behavior of all three physical regimes is also shown in Fig. 3.3. The crystalline phase melts into a non-superfluid liquid upon increase of the temperature. This is not surprising, and underscores the importance of quantum-mechanical exchanges, which underlie superfluidity, in the melting of the Bose solid [4]. Melting occurs at a temperature which decreases on increasing the value of Λ . In the Liquid, we computed three different temperatures: i) the liquid-gas critical temperature, ii) the superfluid transition temperature at the ground state equilibrium density, and iii) the Bose-Einstein condensation temperature of the non-interacting system $T_{\text{BEC}} \approx 3.3125 \Lambda \rho^{2/3}$, also at the ground-state equilibrium density. The interplay between the three temperatures is plotted in Fig. 3.3, and is discussed in more detail in subsection 3.3.3. Finally, we have the superfluid gas regime, in which the system behaves very similarly to a dilute Bose gas.

In the following three sub-sections, we provide more detailed descriptions of the different physical regimes in Fig. 3.3, moving from smaller to larger values of Λ . Detailed P - T phase diagrams are computed at representative Λ values to probe the different phases and the topology of the phase transitions. It is important to reiterate that our results are all using the simple LJ atom-atom interaction. Despite its generality, there will be situations, for example low-density diatomic gases or very high pressure states, where new phases emerge which are not captured by our Hamiltonian.

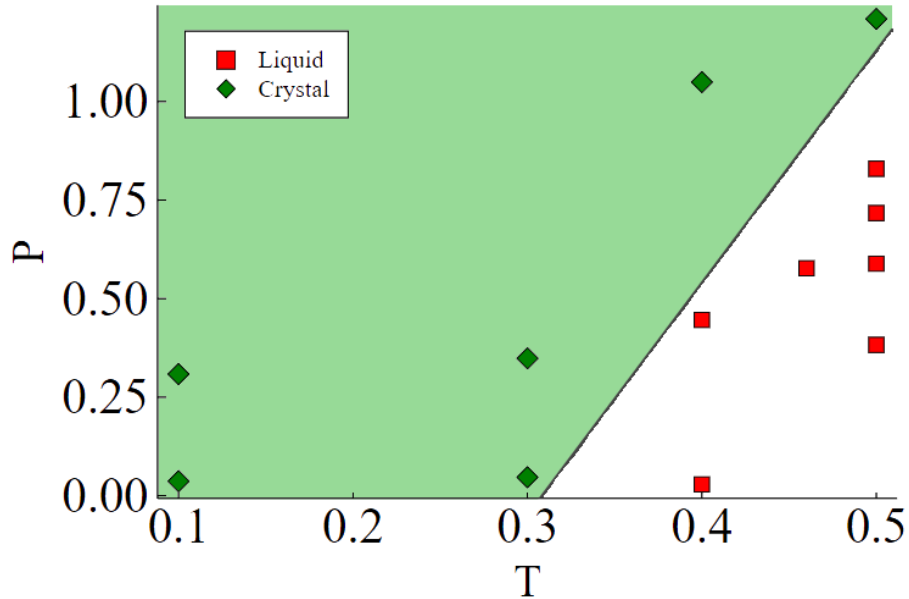


Figure 3.5: The pressure-temperature phase diagram of LJ boson ${}^8\text{He}$ ($\Lambda = 0.09075$). The solid line, drawn as a guide to the eye, corresponds to the first order transition. The low-pressure vapor region is not visible on this scale.

3.3.2 Low Λ regime

At values of Λ corresponding to $X > 4.8$, quantum mechanical exchanges are suppressed, and the ground state is primarily the result of minimizing the potential energy, i.e., a crystal. Nevertheless, as shown in Ref. [4], exchanges play a crucial role in the determination of the melting temperature. It is worth noting that the isotopes ${}^8\text{He}$ and ${}^6\text{He}$ have both been realized in the laboratory, with single nuclei half-lives of 0.12s and 0.8s, respectively.

The pressure-temperature phase diagram at $\Lambda = 0.09075$, corresponding to $X = 8$, is shown in Fig. 3.5.

The melting temperature of the equilibrium crystalline phase goes down as Λ grows, as shown in Fig. 3.3. In particular, we estimate the melting temperature of ${}^6\text{He}$ to be about 2.5 K, the lowest among naturally occurring substances.

On raising Λ , one encounters the fictitious boson isotope ${}^5\text{He}$, which still lies on the solid side of the solid-liquid boundary. Here, the crystalline ground state remains

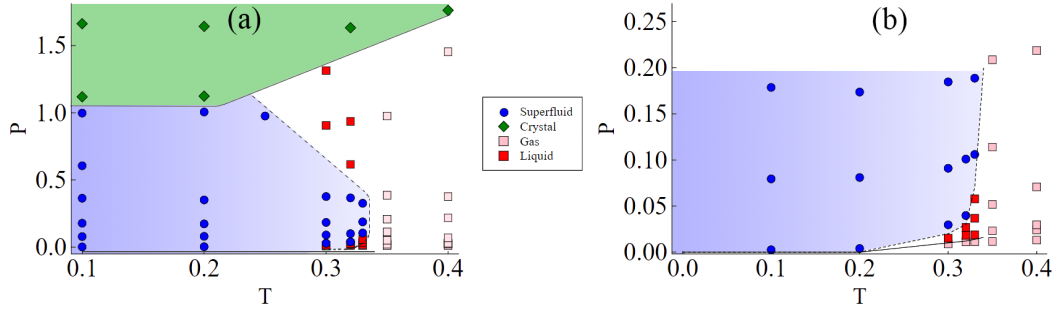


Figure 3.6: (a) The pressure-temperature phase diagram of LJ boson ${}^3\text{He}$ ($\Lambda = 0.242$). (b) Same as (a) but with a zoom into the lower pressure portion. Lines are drawn schematically based on the discrete data points to guide the eye. Solid lines correspond to first order transition, and dashed to second order.

stable against quantum fluctuations, albeit with a relatively small melting temperature of ~ 1.5 K. Interestingly, for a value of X this close to the solid-liquid boundary, we find a possibly long-lived, over-pressurized superfluid phase at the equilibrium density. Such a phase is not realized in systems deeper within the classical regime, such as parahydrogen [110], as well as ${}^6\text{He}$ and ${}^8\text{He}$. It is reminiscent of the situation of ${}^4\text{He}$, in which it is possible to achieve metastable superfluid phases at pressures much higher than the crystallization pressure [60–62, 111].

3.3.3 Intermediate Λ regime

As the value of Λ further grows, one crosses the solid-liquid boundary and encounters the well-characterized ${}^4\text{He}$, the results for which, as mentioned in section 3.2, serve as validation for our methodology, and are compared against the experimental results in Fig. 3.2.

As shown in Fig. 3.3, as one moves further to the right, the superfluid transition temperature (T_λ , computed at the ground-state equilibrium density) goes up, then plateaus and goes slightly back down. This behavior is the result of a competition between two effects that take place as Λ grows: i) the system becomes increasingly quantum mechanical, allowing superfluidity to be possible at higher temperatures, and ii) the equilibrium density decreases, which means that the particles are on av-

erage more widely spaced apart, requiring larger de Broglie wavelengths, and hence lower temperatures, to achieve Bose condensation. On the other hand, the liquid-gas critical temperature T_{LG} goes down monotonically as the value of Λ is increased, as the system experiences more zero-point fluctuations and becomes more loosely bound.

^3He is located at a point fairly close to the crossing of the two temperatures. In Fig. 3.6, we map out the pressure-temperature phase diagram of the fictitious bosonic ^3He , which is distinct from that of ^4He in a number of different ways. Overall, the superfluid region expands greatly, pushing the superfluid-crystal transition line up to higher P , while pushing the superfluid transition line to the right. The first-order line that separates the liquid and gases phases shrinks significantly as T_{LG} drops from 0.5 to around 0.34. The second-order line that separates the superfluid and normal phases, aside from moving to higher temperatures as mentioned, behaves quite differently from the monotonic line with negative slope that appears in ^4He . Instead, the line starts with a very small positive slope at low pressure, bulges out, then curves back around and acquires a negative slope as it approaches the crystalline regime.

It is useful to examine more closely the topology of the phase diagram in the vicinity of T_{LG} , as shown in Fig. 3.6b. When Λ is increased, the second-order line expands to the right and its lower part bends toward the first-order line, which shrinks as its end, the critical point T_{LG} , moves to the left. Ref. [98] studied the evolution of the phase diagram of the LJ Bose liquid in the ultra-quantum regime through mean field considerations based on Landau theory. The authors argued that a portion of the second-order line should turn first-order before the critical point T_{LG} can merge onto it, in order to prevent the superfluid and liquid-gas order parameters from becoming critical at the same point [98]. Our results show that if such a scenario occurs, it is confined to a tiny portion of the superfluid transition line for very specific values of Λ , which is challenging to target numerically.

The (P, T) phase diagram in Fig. 3.6 reveals an interesting range of temperatures near 0.32. At such a temperature, if one starts at zero pressure and continues pressur-

izing, keeping the temperature constant, one first encounters a gaseous phase, followed by a normal liquid phase, followed by a superfluid liquid phase, followed by another normal fluid phase, finally followed by a crystalline phase at the highest pressures.

Another interesting result is the minimum pressure at which bosonic ^3He is found to crystallize. As shown in Fig. 3.6b, the minimum crystallization pressure is around 1 in our units, which corresponds to roughly 84 bars in SI units. This is much higher than the minimum pressure at which the real system, obeying Fermi statistics, is experimentally known to crystallize, which is around 30 bars [112]. This result is of considerable importance, as it shows that quantum statistics indeed play a large role in determining the crystallization pressure of the system [4]. The Fermi system is a non-superfluid liquid at these temperatures, which renders it significantly more susceptible to crystallization. The Bose system, being in the more robust superfluid phase, continues to resist crystallization for much higher pressures. This result is consistent with the prediction made by the variational theory in Ref. [99], in which the authors contend that the solidification pressure of a bosonic ^3He is greater than that of the Fermi system by at least a factor of 2.

3.3.4 Low Λ regime

On further increasing Λ , one counters ^2He , which is located at the region where T_λ exceeds T_{LG} . While the system remains self-bound at zero temperature, it boils before losing its superfluidity upon increasing temperature. This is in contrast with the case of ^4He which, as the temperature is raised, loses superfluidity long before it boils.

The pressure-temperature phase diagram for ^2He is shown in Fig. 3.7, which is simpler compared to that of ^3He . At low temperatures and pressures, a first-order boundary separates the superfluid phase and the gas phase. Beyond T_{LG} , the phases are separated instead by a second order line, which continues to grow as a function of pressure. In the inset of Fig. 3.7, we present a more complete diagram that includes higher pressures. The behavior at high pressure is similar to that of ^3He , where

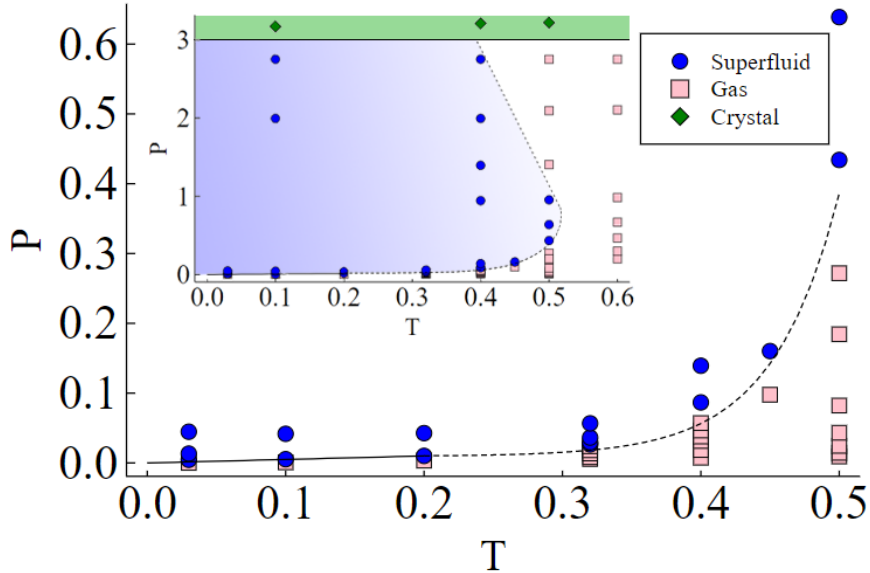


Figure 3.7: The pressure-temperature phase diagram of ${}^2\text{He}$ ($\Lambda = 0.363$). The main graph shows a zoom of the low pressure region, while the inset gives a more global view. Lines are to guide the eye. Solid lines correspond to first order phase transition, and dashed to second order.

the second-order line doubles back and intersects the solid-liquid boundary with a negative slope.

As one continues raising the value of Λ , the first order line separating superfluid and normal phases progressively recedes towards the origin, until the system no longer features a first-order phase transition. The first-order portion vanishes precisely when $\Lambda = \Lambda_c$, where quantum unbinding takes place in the ground state, as we discussed with Fig. 3.4. For $\Lambda > \Lambda_c$ there is only a second-order line separating the superfluid phase and normal gas phase. These features of the phase boundary between the superfluid and gas phases at low pressure are correctly captured by mean-field and analytic theory [98].

3.4 Conclusions

We performed extensive, numerically exact many-body computations of simple Bose systems interacting through the Lennard-Jones potential, and investigated their phys-

ical properties throughout a wide range of the “quantumness” parameter Λ . As a function of Λ , we studied the evolution of the phase diagram, and provided detailed predictions at several values of Λ representative of the different physical regimes.

One goal of this study was to establish the kind of phases, and phase diagram topology that one can encounter in this very broad class of systems. Only insulating crystal and (super)fluid phases are present; no “supersolid” is observed, consistent with a wealth of theoretical predictions pointing to the absence of a supersolid phase in a system in which the dominant interaction is pair-wise and spherically symmetric and features a “hardcore” repulsion at short distances [9, 13]. No coexistence of two superfluid phases is observed either, which is also consistent with the thermodynamics of the liquid-gas transition and our current understanding of the relation between superfluidity and Bose-Einstein condensation in gases.

Given the generality of the LJ interaction, mapping out in detail the thermodynamic phase diagram can guide in the design and interpretation of experiments aimed at observing additional phases of matter, as more experimental avenues continue to open up. Experimental realization of the systems studied here are certainly not limited to helium. Among all naturally occurring substances, significant quantum effects are observed in parahydrogen, and can also be expected in two unstable isotopes of helium which possess an even number of nucleons (i.e., they are bosons). Higher values of Λ may be achieved in a laboratory setting by preparing systems of ultracold atoms, via exotic matter, or in excitonic systems.

In addition to providing a universal phase diagram to this class of simple Bose system, we hope that this investigation also serves as an example of the progress to make definitive and comprehensive predictions on interacting quantum many-body systems. Such examples are still uncommon, but are certainly becoming increasingly possible, owing to the development of reliable and robust computational methods and more cross-fertilization between them with analytical approaches.

Chapter 4

Patterned Supersolids in Dipolar Bose Systems

4.1 Introduction

In search of the more exotic supersolid phase, whose absence in simple helium-like systems was demonstrated in Ch. 3, we now turn our attention to a more specific class of Bose systems, namely dipolar bosons. In this chapter, we present our state-of-the-art quantum Monte Carlo (QMC) investigation of the low temperature phase diagram of dipolar bosons with aligned dipole moments. We model the repulsive part of the interaction by means of an inverse power law potential, as done in previous work [14]; a straightforward connection exists between the characteristic range σ of this interaction, and the scattering length a_s . We map out the phase diagram by computing relevant correlations, as well as the superfluid density, all directly accessible in our numerical approach, as a function of particle density and σ .

The system displays several distinct phases, ranging from an essentially classical crystal of parallel, particle-thin filaments in one limit ($\sigma \rightarrow 0$), to a hard-sphere-like superfluid, reminiscent of liquid ^4He in the opposite ($\sigma \rightarrow \infty$) limit, at any particle density. An intermediate region exists between these two phases, in which the ground state displays both crystalline order and a finite superfluid response. This *supersolid* phase exists within a range of scattering length that depends monotonically on the density.

The crystal structure of the supersolid is quite distinct from that of the classical crystal, determined by quantum-mechanical effects, both zero-point motion as well as exchanges of particles (as already noted in Ref. [14]). Remarkably, the supersolid phase features different arrangements of particles (patterns) in different regions of the phase diagram. At low density, the supersolid phase consists of a crystal of prolate droplets, with quantum-mechanical exchanges of particles across droplets, as suggested in Ref. [14]. As the density is increased, on the other hand, the patterns resemble some of the periodic structures originally predicted to occur in two-dimensional dipolar systems [113, 114].

We study the elementary excitation spectrum for the superfluid phase, which features the experimentally observed “roton” minimum [11], as crystallization is approached from the superfluid side, *both* on *reducing* σ (i.e., moving toward the supersolid phase) as well as on *increasing* it, in which case the system behaves essentially as a hard sphere fluid, transitioning into a conventional (i.e., non-superfluid) crystal.

The remainder of this chapter is organized as follows: in section 4.2 we describe the model of the system; in Sec. 4.3 we briefly describe our methodology; we present and discuss our results in Sec. 4.4 and finally outline our conclusions in Sec. 4.5, where we discuss the relevance of this study to recent experimental work.

4.2 Model

The system is modeled as an ensemble of N identical particles of mass m and spin zero, hence obeying Bose statistics. These particles possess a magnetic moment d , pointing in the z -direction. We are interested in studying the phase diagram of the *bulk*; thus, unlike in a typical experiment, we do not confine the simulated system by means of an external potential. Rather, our system is enclosed in a three dimensional box, shaped like a cuboid of volume V , with periodic boundary conditions in the three directions. The shape of the cell was varied, depending on the particular structures and patterns forming at the various physical conditions. We take the characteristic length of the

dipolar interaction, $a \equiv md^2/\hbar^2$ as our unit of length, and $\epsilon \equiv \hbar^2/(ma^2)$, as that of energy and temperature. The quantum-mechanical many-body Hamiltonian in dimensionless form reads as follows:

$$\hat{H} = -\frac{1}{2} \sum_i \nabla_i^2 + \sum_{i<j} U(\mathbf{r}_i, \mathbf{r}_j) \quad (4.1)$$

where the first (second) sum runs over all particles (pairs of particles), and the pair potential consists of two parts, $U(\mathbf{r}, \mathbf{r}') = U_{sr}(|\mathbf{r} - \mathbf{r}'|) + U_d(\mathbf{r}, \mathbf{r}')$, U_{sr} being the repulsive part. As mentioned above, in most theoretical studies the repulsive part of the interaction is modeled by means of the so-called scattering length approximation, namely

$$U_{sr}(r) = \frac{4\pi\hbar^2 a_s}{m} \delta(\mathbf{r}) \quad (4.2)$$

To the extent that such a representation is valid, expression (4.2) can be replaced by any other potential that has the same scattering length a_s . In this work, we use for U_{sr} the repulsive part of the standard Lennard-Jones potential, i.e.,

$$U_{sr}(r) = (\sigma/r)^{12} \quad (4.3)$$

whose use is more convenient in numerical simulations. The parameter σ of the potential U_{sr} used here is directly related to the scattering length a_s , through

$$\frac{a_s}{\sigma} \approx 0.76 \sigma^{1/5} \quad (4.4)$$

(see, for instance, Ref. [115]). U_d is the classical dipolar interaction between two aligned dipole moments, namely

$$U_d(\mathbf{r}, \mathbf{r}') = \frac{1}{|\mathbf{r} - \mathbf{r}'|^3} \left(1 - \frac{3(z - z')^2}{|\mathbf{r} - \mathbf{r}'|^2} \right) \quad (4.5)$$

At zero temperature, there are two parameters that govern the physics of the system, namely the particle density $\rho \equiv N/V$, and the characteristic range σ of the repulsive interaction. The classical limit is approached as $\sigma \rightarrow 0$, whereupon the attractive

well of the anisotropic interaction becomes deep enough to dominate the physics, and quantum mechanical effects are small. On the other hand, as σ is increased, quantum mechanical effects are increasingly prominent, eventually destabilizing the classical ground state and giving rise to interesting physics.

4.3 Calculation

We carry out QMC simulations of the system described in section 4.2 using the continuous-space worm algorithm (see Ch. 2). Although this is a finite temperature technique, we perform simulations at sufficiently low temperatures, so that computed physical properties are essentially those of the ground state.

We survey the phase diagram of the system by performing simulations at a fixed density for different values of σ , and then repeating the process for different values of the density. We performed simulations of systems of sizes ranging from $N = 160$ to $N = 648$ particles, and densities between $\rho = 0.125$, which is close to the value of some of the current experiments [11], and up to three orders of magnitude higher, i.e., $\rho = 100$, quite likely not attainable in present time experiments but nonetheless of fundamental interest. To ensure that the physics is independent of the initial configuration of the particles, most simulations were started from high-temperature, disordered configurations.

Details of the simulation are standard; we made use of the primitive approximation for the high-temperature density matrix. Although more accurate forms exist, we found that in practice with this particular interaction the primitive approximation is the most efficient. All of the results quoted here are extrapolated to the limit of time step $\delta\tau \rightarrow 0$; quite generally we found numerical estimates for structural and superfluid properties of interest here obtained with a value of the time step $\delta\tau \sim 10^{-3}\epsilon^{-1}$ to be indistinguishable from the extrapolated ones, within the statistical uncertainties of the calculation.

Occurrence of crystalline order in the system can be detected through the calcula-

tion of the static structure factor $S(\mathbf{q})$; because of the anisotropy of the interaction and the ensuing tendency of the system to form filaments along z (the direction of alignment of the dipole moments), we computed $S(\mathbf{q})$ for \mathbf{q} -vectors lying in the xy plane. As mentioned above, distinct, characteristic patterns form for different values of the parameters ρ, σ . The identification of the various patterns is achieved through visual inspection of the configurations generated by the algorithm in the course of sufficiently long computer runs.

The superfluid response of the system is assessed through the direct calculation of the superfluid fraction $\rho_S(T)$, by means of the well-known winding number estimator [80]. Due to the anisotropic nature of the interaction, and consequently of the superfluid (and supersolid) phases observed here, we offer results for the in-plane (xy) superfluid response only. A typical result for the in-plane superfluid fraction ρ_S is shown in Fig. 4.1b.

4.4 Results

4.4.1 Phase diagram

The ground state phase diagram of the system, as it emerges from our extensive QMC simulations, is shown in Fig. 4.1a in the $\rho - \sigma$ plane. Here we outline some of its generic features, offering a more detailed discussion of the two most interesting phases (the supersolid and the superfluid) in subsections 4.4.2 and 4.4.3.

For any fixed value of the density, two clear physical limits can be easily identified, more intuitively discussed in terms of the average inter-particle distance $b \equiv \rho^{-1/3}$. Specifically, if $\sigma \ll b$, the ground state of the system consists of an ordered array (a triangular lattice) of thin filaments oriented along the z -direction. An example is shown in Fig. 4.2a, displaying the density of the system, integrated along the

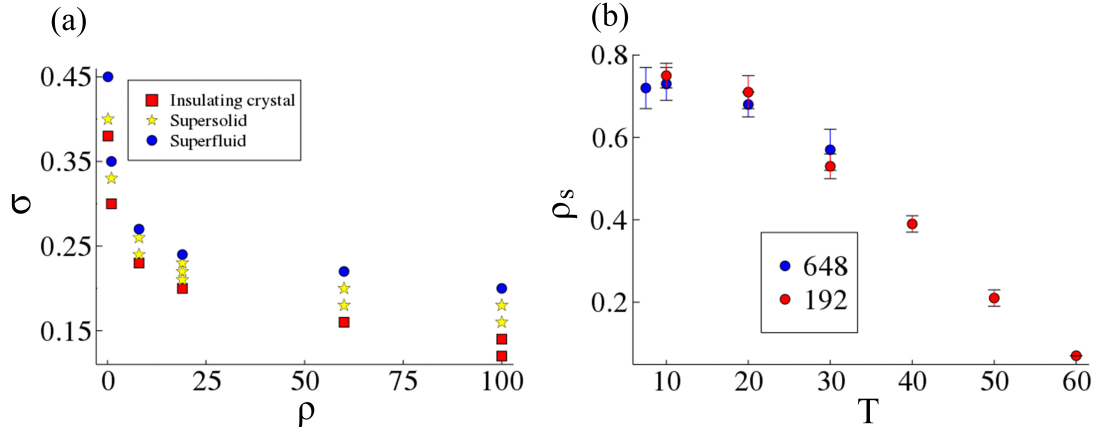


Figure 4.1: (a) Ground state phase diagram of the system in the (ρ, σ) plane. Each phase is determined through simulations as explained in the text. (b) Superfluid fraction (xy plane) of the system at $\rho = 100$ and $\sigma = 0.18$ as a function of temperature, and for two system sizes.

z -direction.¹ In this physical limit, the depth of the attractive well of the dipolar interaction causes the potential energy to dominate the behavior of the system, which can be understood and predicted quantitatively along classical lines, as shown in Ref. [14]. Specifically, the system forms an ordered array of particle-thin parallel filaments, arranged on a triangular lattice. In this case, exchanges of identical particles are suppressed, both within a filament, as well as across filaments.

Conversely, when σ becomes of the order of the inter-particle distance b , the attractive well of the dipolar interaction weakens, and the physics of the system morphs into that of a hard-sphere fluid, as the repulsive part of the interaction becomes the dominant feature. The behavior of the system in this limit is very similar to that of superfluid ^4He , which undergoes “conventional” crystallization as $\sigma \sim b$ (this part of the phase diagram is not shown in Fig. 4.1a).

As shown in Fig. 4.1a, there is in an intermediate range of σ/b wherein the system displays the most interesting, novel behavior, specifically a supersolid phase, which

¹More precisely, Fig. 4.2a, like other similar images featured in this paper, shows the particle density map (integrated over the z direction) obtained from a statistically representative configuration (i.e., particle world lines). By “statistically” representative, we mean that every configuration generated in the simulation is physically equivalent to that shown in the figure, differing at the most by a rotation and/or a translation.

we discuss in detail in subsection 4.4.2. A remarkable feature of this phase diagram is that there is no way of going from the superfluid to the insulating crystalline phase at zero temperature, by varying ρ and/or σ , without going through a supersolid phase. This is also the case in a 2D system of soft-core bosons [116].

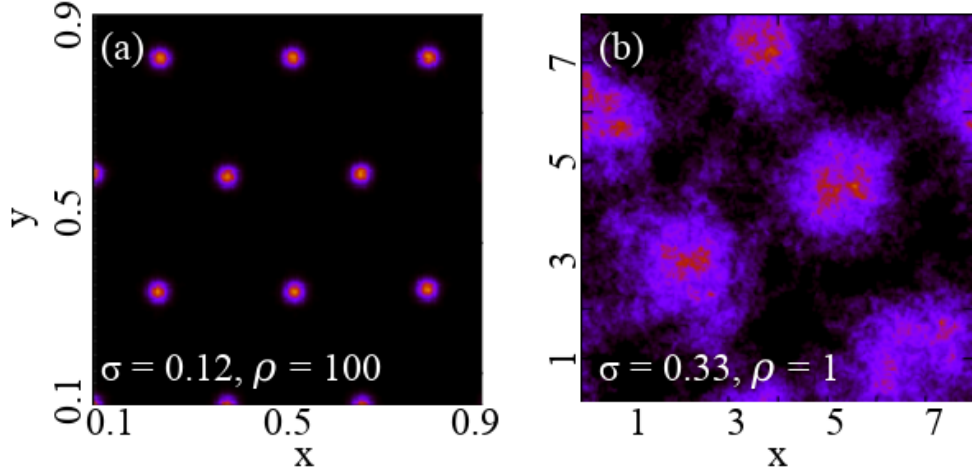


Figure 4.2: Density maps of the system at density $\rho = 100$ for $\sigma = 0.12$ (a), and $\rho = 1$ for $\sigma = 0.33$ (b), integrated along the z -direction (i.e., the direction of dipole moment alignment). Brighter areas indicate higher density. The maps are obtained from particle world lines of a single configuration. In (a), the physics of the system is dominated by the potential energy, and the ground state is essentially the classical one, consisting of an array of particle-thin, parallel filaments. In (b), the ground state is a crystal of droplets with frequent quantum mechanical exchanges among adjacent droplets, leading to a finite superfluid response (as such, displaying supersolid behavior).

4.4.2 Supersolid

The supersolid phase is generally characterized by the formation of relatively large, prolate droplets, elongated in the z -direction, arranging themselves on a triangular lattice or forming more complex structures, as we discuss below. Quantum mechanical exchanges of identical particles, largely suppressed in the classical filament crystal, become important, initially within a single filament and progressively across filaments, establishing phase coherence and leading to a finite, three-dimensional superfluid re-

sponse throughout the system. It is interesting to note that while the superfluid response is anisotropic, and in the xy plane saturates to a value lower than unity as $T \rightarrow 0$ (see Fig. 4.1b), as expected [71], it is always seen to approach unity, in the same limit, in the direction of elongation of the droplets (z).

The range of values of σ within which the system displays supersolid behavior depends on the density of the system, as shown in Fig. 4.1a. In particular, at high density the supersolid occurs for lower values of σ , as quantum-mechanical exchanges are favored by a lower inter-particle distance. The width in σ of the supersolid region, however, appears to be roughly independent of ρ .

As mentioned above, the occurrence of an ordered arrangement can be established through the calculation of the static structure factor, which develops (Bragg) peaks in correspondence of relevant wave vectors (e.g., the inverse distance between droplets). Additional information comes from the direct visual inspection of the patterns that form in the course of the simulation, which are quantum-mechanical in nature and can be markedly different, depending on both the density and the value of σ .

Fig. 4.2b shows the same type of density map as in Fig. 4.2a, but for a supersolid system. As one can see, the filaments are in this case replaced by larger droplets, which include considerably more particles than the classical filaments.² Quantum-mechanical exchanges among adjacent droplets are frequent at low temperature (i.e., $T \sim 1$ for this particular choice of ρ , σ); consequently, macroscopic exchange cycles (i.e., comprising nearly *all* the particles in the system) take place. Clearly, the density map shown in Fig. 4.2b is very reminiscent of those that appear in a purely two-dimensional (2D) system of soft-core bosons [46, 116], namely the simplest supersolid. Indeed, the physics of the system under study here, projected onto the plane perpendicular to the filaments, could be regarded as equivalent to that of a 2D soft core system, the third dimension serving the purpose of “piling up” particles, thus

²It is important to note that these objects appear *spontaneously*, i.e., they are not the result of a particular choice of starting configuration of the simulation; indeed, they form regardless of what such a starting point is.

allowing for the formation of “cluster” unit cells.

It is quite interesting to note that the supersolid phase does not always display the structure shown in Fig. 4.2b. Rather, at high particle density patterns begin to emerge, such as the inverted droplet structure shown in Fig. 4.3a, and the striped one³ of Fig. 4.3b, or others that are evocative of those predicted for 2D dipolar systems, in the context of “microemulsions” [113, 114]

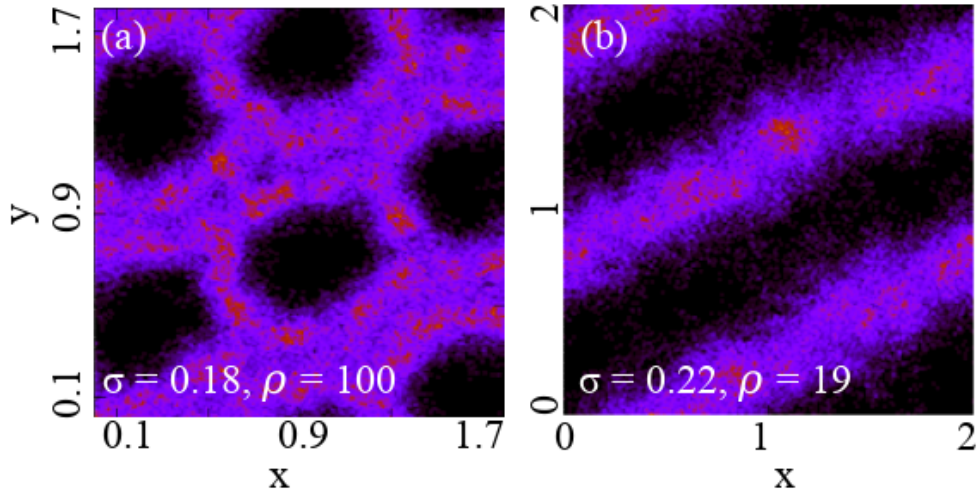


Figure 4.3: Density maps of the system at density $\rho = 100$, for $\sigma = 0.18$ (a), and $\rho = 19$, for $\sigma = 0.22$ (b), integrated along the z -direction. Brighter areas indicate higher density. These maps are obtained from particle world lines of a single configuration.

4.4.3 Superfluid

The superfluid phase arises as the range of the repulsive interaction U_{sr} (eq. 4.3) is progressively increased, at fixed density, as shown in Fig. 4.1a. As the droplets expand, due to the hardcore repulsion, they eventually merge, giving rise to a uniform superfluid phase. It is interesting to study the elementary excitation spectrum of the superfluid phase, especially as crystallization is approached.

Although it is possible to infer the excitation spectrum from the full imaginary time dynamics, computed by QMC, using an inversion method (e.g., MaxEnt as described

³It is interesting to note that in the strictly two-dimensional limit no striped supersolid phase exists in this system. See F. Cinti and M. Boninsegni, *J. Low Temp. Phys.*, vol. 196, p. 413, 2019

in Sec. 2.5), because we are only interested here in gaining qualitative understanding we make use of a simpler approach, based on the Bijl-Feynman approximation [86]. Specifically, we assume that the dynamic structure factor $S(\mathbf{q}, \omega)$ is dominated by a single peak, which allows one to obtain the elementary excitation spectrum as

$$e(q) = \frac{q^2}{2S(q)} \quad (4.6)$$

eq. 4.6, known as Bijl-Feynman formula, provides a reasonable qualitative and semi-quantitative account of the elementary excitation spectrum in superfluid ^4He , in particular of the presence and position of the roton minimum [70].

The behavior of the excitation spectrum as a function of σ is the same across all values of density investigated in our simulations. Fig 4.4 shows two examples, for $\rho = 1.0$ and $\rho = 100$. The phonon-like dispersion, that is characteristic of the superfluid phase at low q , starts acquiring a negative curvature as the superfluid-supersolid transition is approached from above (with reference to the phase diagram shown in Fig. 4.1a). At values of σ sufficiently close to the critical value, the system experiences stronger density fluctuations at that value of the momentum, giving rise to a roton minimum and signaling incipient crystallization.

These results are at least in qualitative agreement with the experimental data in Ref. [117]. As the value of σ is lowered, the roton minimum becomes progressively lower, eventually hitting the horizontal axis; that is consistent with the divergence of $S(q)$ at the roton wave vector, i.e., the formation of a dipolar crystal. We come back to a more extensive comparison of our results with experiment in the next section.

It is important to note that the presence of a roton minimum in the elementary excitation spectrum merely signals the proximity of the system to crystallization. As such, it is not a special feature of this particular system, or of the character of the interaction (dipolar). Indeed, a roton minimum can be observed in the large σ limit, in which the system is essentially a gas of hard spheres, as the crystal (in this case a conventional one, i.e., with few particles per unit cell) is approached from below.

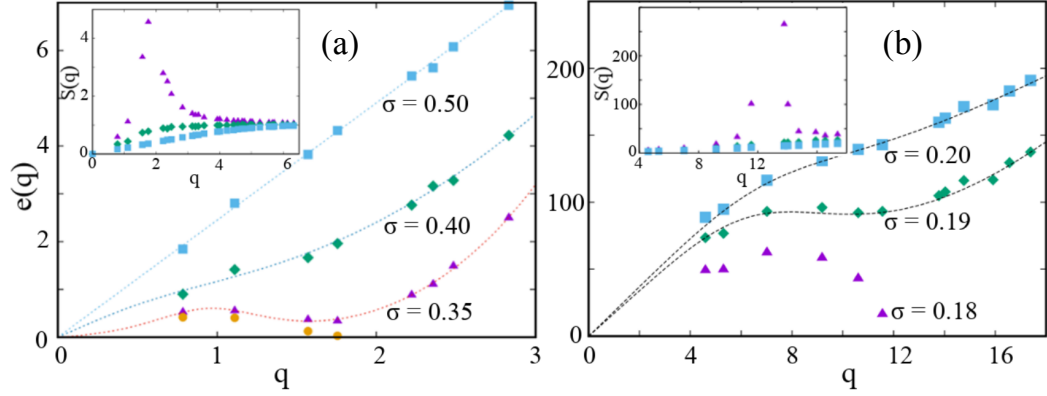


Figure 4.4: Elementary excitation spectra of a system of dipolar bosons for different values of the repulsive radius σ near the superfluid-supersolid transition, computed using eq. 4.6. Results shown here are for $\rho = 1$ (a) and $\rho = 100$ (b), in the low temperature limit. Statistical errors are smaller than the size of the symbols. Solid lines are fits to the data using Padé approximants, and are only meant as a guide to the eye. Insets show the corresponding in-plane static structure factor $S(q)$, averaged over all directions. In (a), yellow circles refer to $\sigma = 0.33$, for which crystal order appears, i.e., the system is in the supersolid phase. In (b), this happens at $\sigma = 0.18$

In the latter case, the roton minimum forms at a different, higher value of the wave vector, which reflects the fact that the ensuing crystal structure in this case has a smaller lattice constant.

4.5 Conclusions

We carried out extensive QMC simulations of a system of dipolar Bose particles of spin zero, in three dimensions, in order to gain insight into the phase diagram of this system. The anisotropic character of the interaction gives rise to novel phases, chiefly a supersolid characterized by various, intriguing density patterns.

The supersolid phase appears to be observable in a relatively broad range of parameter space, obviously making allowance for the difficulty of exploring the high density phase, as three-body recombination must be overcome.

The results presented here are consistent with recent experimental data [117–120]. In order to assess whether the density range explored here is comparable to that of recent experiments, we consider Ref. [120], reporting measurements carried out on an

assembly of ^{164}Dy atoms. Using their numbers, namely $N = 3.5 \times 10^4$ atoms confined in an anisotropic harmonic potential of characteristic frequencies equal to 300, 16 and 22 Hz, we estimate the density at the center of the trap $\sim 1.3 \times 10^{-8} \text{ \AA}^{-3}$. Expressed in units of the dipolar length a , which in this case is worth 208 \AA , this is equal to 0.117, i.e., very close to the lowest density considered in this work.⁴ Indeed, the results shown in Fig. 1g of ref. [120] indicate that the transition between a uniform BEC and a supersolid occurs in correspondence of a scattering length $a_s \sim 0.24 a$, which is in remarkable quantitative agreement with our prediction of $\sigma \sim 0.4 a$ for $\rho = 0.125$ (eq. 4.4 yields $\sigma = 0.38$ if $a_s = 0.24$).

This result provides strong quantitative support for the microscopic model utilized here, as well as for the results of our calculation. It also suggests that the experimental findings of Ref. [120] reflect the physics of the bulk, to an appreciable extent, i.e., they are not overly affected by confinement, nor by the relatively small size of the system. This observation is consistent with the conclusions of a theoretical (mean-field) study of the system confined in an elongated trap [121], whose results are in qualitative agreement with ours.

⁴It need be noted that the dipolar length defined in Ref. [117] is equivalent to 1/3 of that defined here.

Chapter 5

Dipolar Bosons in One Dimension: The Case of Longitudinal Dipole Alignment

5.1 Introduction

We now consider dipolar bosons in 1D, where quantum effects are enhanced with respect to the 3D case studied in Ch. 4. One-dimensional systems of dipoles are of interest because the interaction, while not strictly long-ranged as in three dimensions, has a much greater spatial extent than most conventional (i.e., atomic or molecular) interactions, and/or interactions for which analytical results are known. Moreover, it is anisotropic, which in principle can lead to different physical behavior on aligning dipole moments in different directions.

Dipolar bosons in 1D have been studied in previous works [122–126], typically in the case of dipole moments aligned perpendicularly to the direction of particle motion, rendering the dipolar interaction purely repulsive, i.e., with no many-body bound state. In this chapter, instead, we align the dipole moments along the direction of motion, which makes the dipolar interaction purely attractive. In order to prevent the system from collapsing, we add a hard-sphere-like repulsion of variable range σ , as we did in Ch. 4. The presence of attractive interactions qualitatively alters the physical behavior of the system, with respect to the case studied so far. By tuning

the range of the repulsive interaction, we are able to explore the different physical regimes and phases accessible to the system.

We carried out a systematic investigation of the ground state phase diagram of the system as a function of particle density and σ , by means of computer simulations. The main results of our study are the following: *a)* the system is self-bound in the $\sigma \rightarrow 0$ limit, in which the two-body interaction features a deep attractive well; the character of the many-body ground state evolves from quasi-crystalline to a non-superfluid liquid as σ is increased, and for $\sigma > \sigma_c$, a gas-liquid quantum phase transition occurs, as the system becomes unbound *b)* in the gas phase, near the critical value σ_c , attractive interactions bring the system at low density into the regime known as “weak superfluid”, i.e., unstable against infinitesimal perturbations (e.g., disorder or commensurate potentials). Interestingly, the topologically protected superfluid regime cannot be approached, as the system breaks down into coexisting gas and liquid phases in the dilute limit, despite being unbound. This behavior is reminiscent of that predicted for quasi-2D ^3He films adsorbed on weakly attractive substrates.

The remainder of this chapter is organized as follows: in section 5.2 we describe the model of the system, and briefly summarize the universal theoretical framework that describes systems in 1D; in Sec. 5.3 we describe our methodology; we present and discuss our results in Sec. 5.4 and finally outline our conclusions in Sec. 5.5.

5.2 Model

We model the system as an ensemble of N identical particles of mass m confined to the x -axis. The particles have spin zero, i.e., they obey Bose statistics, and a magnetic moment d pointing in the positive x -direction. The system is enclosed in a box of length L with periodic boundary conditions. The density of the system is $\rho = N/L$. We take the characteristic length of the dipolar interaction, $a \equiv md^2/\hbar^2$ as our unit

of length, and $\epsilon \equiv \hbar^2/(ma^2)$, as that of energy. In these units, the dimensionless quantum-mechanical many-body Hamiltonian reads as follows:

$$\hat{H} = -\frac{1}{2} \sum_i \frac{\partial^2}{\partial x_i^2} + \sum_{i < j} U(x_i, x_j) \quad (5.1)$$

where the first (second) sum runs over all particles (pairs of particles). The pair potential comprises two parts,

$$U(x, x') = U_d(x, x') + U_{sr}(x, x'). \quad (5.2)$$

U_d is the classical dipolar interaction, which, for particles confined to the x-axis with their dipole moments pointing along the same axis, reads

$$U_d(x) = -\frac{2}{|x|^3}, \quad (5.3)$$

i.e., unlike the case in which dipoles are aligned in the direction perpendicular to the line of particle motion, it is purely attractive and would lead to the collapse of the system, if a short-range, repulsive part were not included in the interaction. The physical origin of such a repulsive term can be different, depending on the physical system. As mentioned previously, any atomic or molecular interaction must feature a hardcore repulsion at short distance arising from Pauli exclusion principle, which prevents electronic clouds of different atoms from overlapping spatially. In that case, the effective hardcore diameter is $\sim 1 \text{ \AA}$, i.e., much smaller than the typical value of the characteristic dipolar length in the majority of current experiments (see, for instance, Ref. [127]) with cold dipolar atoms or molecules. Significantly greater ranges could be achieved, e.g., by means of the Feshbach resonance [25].

Here we also model U_{sr} through the repulsive part of the standard Lennard-Jones potential, i.e.,

$$U_{sr}(x) = (\sigma/x)^{12} \quad (5.4)$$

For positive scattering lengths, which is always the case for the interaction in 5.4, the effective diameter σ can be directly related to the scattering length a_s (see, for

instance, Ref. [115]). It is worth clarifying that the actual form of U_{sr} is not expected to be important; it can be regarded as a hard wall, its role being exclusively that of preventing system collapse. The physics of interest here takes place at average inter-particle separations that are significantly greater than σ , rendering the contribution of U_{sr} usually relatively small at the densities of interest. For alternative ways to treat the short-range interaction, see, for instance, Ref. [122, 124, 128].

The presence of both a repulsive and an attractive term, with very different dependencies on the inter-particle distance, make it possible for the system to be self-bound. In the $\sigma \rightarrow 0$ limit, U features a deep attractive well, $\sim -2/\sigma^3$, as a result of which the ground state of the system is a nearly classical crystal. On the other hand, as σ grows the attraction is progressively weakened; one expects the ground state of the self-bound system to become liquid-like, and that a liquid-gas quantum phase transition should occur for $\sigma > \sigma_c$, σ_c being the upper limit for the existence of a self-bound state.

We study the ground phase diagram of (5.1) by means of computer simulations, and interpret our results in terms of the LLT, i.e., the comprehensive theoretical apparatus that describes the physics of quantum many-body systems in one dimension [129]. The essence of the LLT is embodied in an effective quadratic Hamiltonian, expressed in terms of two bosonic fields $\theta(x)$ and $\phi(x)$, related to density and phase oscillations respectively (see, for instance, Ref. [130]). In terms of these fields, to leading order, the Hamiltonian reads

$$H = \frac{c}{2\pi} \int_0^L dx \left[\frac{1}{K} (\partial_x \phi)^2 + K (\partial_x \theta)^2 \right] \quad (5.5)$$

where c is the speed of sound of the linearly dispersed low energy excitations, and K is the universal Tomonaga-Luttinger parameter which characterizes the relative strength of density and phase oscillations.

In one dimension, quantum fluctuations are strong enough to destroy long-range order. However, correlation functions decay algebraically, allowing for the possibility

of quasi-long-range order, depending on the value of the decay exponent, which is K ($1/K$) in the case of phase (density) correlations; broadly speaking, in the $K \rightarrow 0$ ($K \rightarrow \infty$) limit the system possesses quasi-superfluid (quasi-crystalline) order.¹ We come back to this point below, with a more precise classification.

5.3 Calculation

As mentioned above, we carry out computer simulations of the system described in section 5.2 using the continuous-space worm algorithm described in Ch. 2. Although this is a finite temperature (T) technique, we perform simulations at sufficiently low T so that the results can be regarded as essentially ground state (we come back to this below). Experience accumulated over the past two decades shows that finite temperature techniques are a reliable option to study the ground state of Bose systems, as they are unaffected by serious limitations plaguing ground state methods [131–133].

Although the computational methodology adopted here allows for the calculation of off-diagonal correlations, the results shown in Sec. 5.4 all pertain to diagonal correlations; therefore, since exchanges of indistinguishable particles are strictly forbidden in 1D by the hardcore of the interaction, they can be obtained by means of conventional path integral Monte Carlo as well (see, for instance, Ref. [77]).

In the ground state, the physics of the system depends exclusively on the value of σ and on the density ρ , or, equivalently, the average inter-particle separation $\lambda \equiv \rho^{-1}$. We investigate the ground state of the system as a function of σ ; that is, for a given value of σ , we compute the equation of state, determining the equilibrium density of the system, and at that density compute relevant correlation functions in real and momentum space. We performed simulations for values of σ in the $[0.10, 2]$ range; our typical system sizes range from $N = 25$ to $N = 400$. Details of the simulation are standard; we made use of the fourth-order approximation for the high-temperature

¹It should be mentioned that, while the convention adopted here is the same as in many other works, elsewhere in the literature K is defined as the reciprocal of the parameter defined in this work.

density matrix (see Ch. 2), all of the results quoted here are extrapolated to the limit of time step $\delta\tau \rightarrow 0$.

As mentioned above, while true long-range order cannot exist in 1D, quasi-order can manifest itself in the form of an algebraic decay of the correlation functions, governed by the exponent K . By studying the evolution of its value as a function of σ (i.e., of the equilibrium density) we characterize the kind of (quasi) order that the system displays. Two methods were primarily utilized to extract the Tomonaga-Luttinger parameter K at the various physical conditions. The first is through the static structure factor $S(q)$, which quantifies the strength of density fluctuations with momentum q . In the units adopted here, the Tomonaga-Luttinger parameter $K = c\lambda/\pi$, where $\lambda = 1/\rho$ is the inter-particle distance and c is the speed of sound, accessible from the long-wave behavior of the static structure factor through relation

$$\frac{1}{2c} = \lim_{q \rightarrow 0} \frac{S(q)}{q} \quad (5.6)$$

The second method to calculate K is through the equation of state $e(\rho)$, i.e., the energy per particle as a function of the density at $T = 0$, from which one can obtain the compressibility $\kappa = \rho^{-1} \partial\rho/\partial P$, where P is the pressure. κ is related to K through the relation $K = (\pi^2 \lambda_o^3 \kappa)^{-1/2}$, where λ_o is the inter-particle distance at the equilibrium density [130]. The agreement of the values of K computed through the two methods serves as a self-consistency check.

5.4 Results

We compute the equation of state $e(\rho)$, where e is the energy per particle, in the $T = 0$ limit, as a function of σ . As ours is a finite temperature method, extrapolation of the results obtained at low T is required; in practice, the shape of the curve $e(\rho)$ is found not to change significantly once the temperature is of order ~ 0.1 of the average kinetic energy per particle.

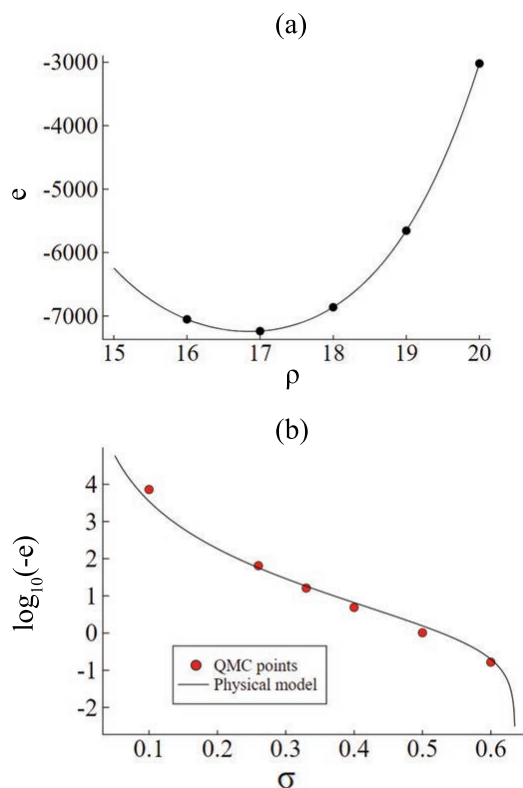


Figure 5.1: (a) Energy per particle $e(\rho)$ at $\sigma = 0.10$ as a function of density in the $T \rightarrow 0$ limit. Statistical errors are smaller than the size of the symbols. Solid line is a quartic fit to the data. (b) Logarithm of the negative energy per particle in the $T \rightarrow 0$ limit, as a function of σ . Circles are the results of the simulations, solid line is a fit based on eq. 5.7 (see text).

An example is shown in Fig. 5.1a for $\sigma = 0.10$. For this value of σ , the interaction potential possesses a deep attractive well, and as a result $e(\rho)$ displays a clear minimum at $\rho = 17$, which corresponds to the equilibrium density. Simulations at density lower than the equilibrium one can be carried out down to the spinodal density, i.e., that at which the speed of sound vanishes and below which the uniform system becomes unstable against the formation of “puddles” of fluid. The curvature of $e(\rho)$ also provides a method of computing the value of the Tomonaga-Luttinger parameter, as explained in Sec. 5.3.

As the value of σ is increased, the magnitude of the binding energy decreases, until

it hits zero at $\sigma = \sigma_c$, whereupon the system becomes unbound. In order to obtain a quantitative estimate for σ_c , we fit our computed $e(\rho)$ for the different values of σ , with the following simple expression, based on the crude approximation for the pair correlation function $g(x) = \Theta(x - \lambda/2)$ (Θ being the Heaviside's function):

$$e(\lambda) = \frac{C_1}{\lambda^2} - \frac{C_2}{\lambda^3} + 0.045 \left(\frac{2\sigma}{\lambda} \right)^{12}, \quad (5.7)$$

where C_1 and C_2 are fitting parameters. The results are shown in Fig. 5.1b. Beyond $\sigma = \sigma_c$, the first (kinetic energy) term in eq. 5.7 overtakes the second (attractive part of the potential energy) in magnitude, the system is no longer self-bound and a liquid-gas quantum phase transition occurs. We estimate $\sigma_c = 0.65 \pm 0.02$, based on the values of the fitting parameters $C_1 \approx 1.25$ and $C_2 \approx 0.76$.

The evolution of the structure of the ground state as the hardcore diameter σ is varied can be illustrated by means of the pair correlation function $g(x)$. At low σ , the depth of the attractive well favors a quasi-crystalline orderly arrangement of particles, consistent with a value of the Tomonaga-Luttinger parameter $K > 2$. Fig. 5.2a shows the result for $g(x)$ at $\sigma = 0.10$, at the equilibrium density $\rho = 0.17$. On the other hand, as σ grows and the binding energy tends to zero, the system acquires a more liquid-like character, behaving essentially like a hard-sphere fluid. This is clear in Fig. 5.2b, where $g(x)$ is displayed for $\sigma = 0.60$, at the equilibrium density $\rho = 0.6$. In both cases, the computed $g(x)$ features the expected scaling, i.e., results at a given density only depend on the product NT , in the low- T limit.

A more quantitative characterization of the physics of the ground state of the system is achieved through the determination of the Tomonaga-Luttinger parameter K . We discuss our results for the Tomonaga-Luttinger parameter for the two cases $\sigma < \sigma_c$ (i.e., where the system is self-bound) and $\sigma > \sigma_c$. As explained above, the most direct way of obtaining K from the simulation data makes use of the computed static structure factor $S(q)$, through eq. 5.6. Results for the static structure factor at the equilibrium density for different values of $\sigma < \sigma_c$, are shown in Fig. 5.3. $S(q)$ is

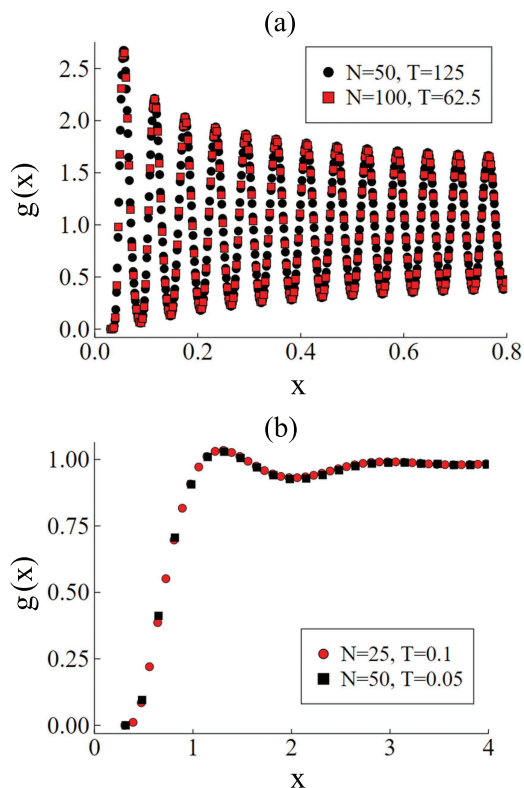


Figure 5.2: Ground state pair correlation functions $g(x)$ for the system at $\sigma = 0.10$ (a) and $\sigma = 0.60$ (b), each at two different system sizes N and temperatures T , at the computed equilibrium densities, namely $\rho = 17$ (0.6) for $\sigma = 0.10$ (0.60). Statistical errors are smaller than the size of the symbols.

computed directly and/or through the Fourier transform of $g(x)$. Fig. 5.3b illustrates an example of the calculation of K through $S(q)$, in this case at $\sigma = 0.26$.

A strongly oscillatory behaviour of the $g(x)$, e.g., as shown in Fig. 5.2a, is reflected by the appearance of divergent peaks in $S(q)$. Correspondingly, the value of K is above 2, consistently with the presence of quasi-crystalline order. As σ grows, K decreases, and becomes less than 2 at $\sigma \gtrsim 0.35$.

Our results for the Tomonaga-Luttinger parameter below σ_c are shown in Fig. 5.4. As expected, K at the equilibrium density is a monotonically decreasing function of σ , but was always observed to remain above 1 in the range of σ within which the system is self-bound. It approaches unity from above as $\sigma \rightarrow \sigma_c$, above which the

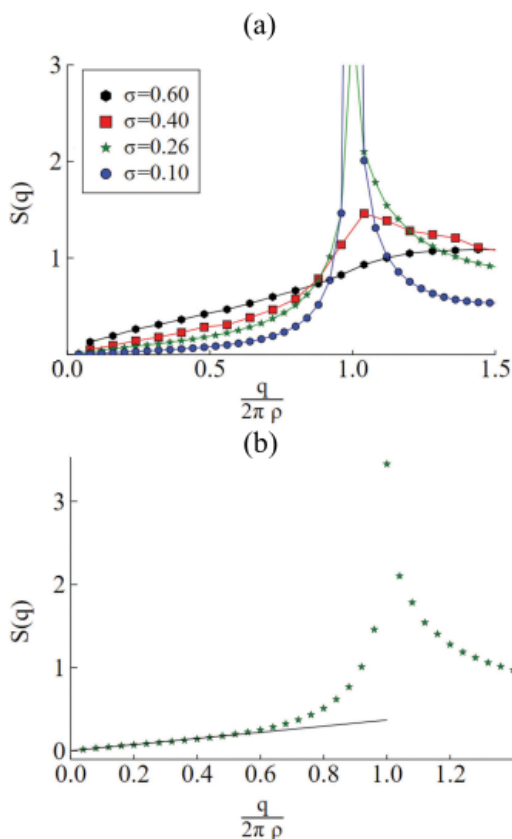


Figure 5.3: (a) The static structure factor at the equilibrium density for various values of σ , in the low temperature limit. Statistical errors are smaller than the size of the symbols. (b) Example of extraction of the Luttinger parameter K based on eq. 5.6, for $\sigma = 0.26$.

behavior of the system is dominated by repulsive interactions (the Tonks-Girardeau regime [130]). For $0.35 \lesssim \sigma \lesssim \sigma_c$, it is $2 > K > 1$, i.e., no evidence was found of topologically protected superfluid phases in the range in which the system exists as a self-bound liquid. This overall physical behavior is qualitatively distinct from that of both 1D ^4He , which is a quasi-superfluid at equilibrium [134], as well as parahydrogen, which is quasi-crystalline [8].

Our results for the Tomonaga-Luttinger parameter for $\sigma \gtrsim \sigma_c$ are shown in Fig. 5.5 for two values of σ , namely 0.7 and 1. The first value of σ is in the immediate vicinity of σ_c . While the system is no longer self-bound, the attractive part of the interaction drives K below 1, as in the case of 1D ^3He [135]. The lowest computed

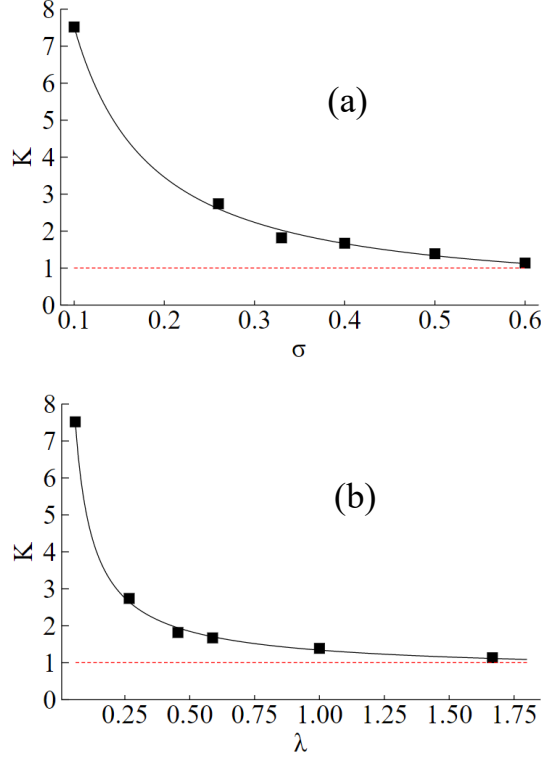


Figure 5.4: The Tomonaga-Luttinger parameter of the system as a function of σ (a) and the equilibrium density ρ (b). The red dashed line is $K = 1$, the Tonks-Girardeau limit. Statistical errors are smaller than size of the symbols. Solid lines are guides to the eyes.

value of K is ≈ 0.8 for $\rho = 0.4$; at lower density, the system is observed to break down into two coexisting phases, a low-density gas and a liquid of density $\rho = 0.4$. The same behavior is observed for $\sigma = 1$, for which K reaches a minimum value of ~ 0.9 for $\rho \approx 0.15$.

The coexistence of a low-density gas and a liquid phase in a system that is not self-bound was already reported in quasi-2D ^3He films on weakly attractive substrates [136]; it is reflected in the equation of state, as shown in Fig. 5.5b for $\sigma = 1$. The energy per particle is a nearly “flat” function of the density² in the range $0.025 < \rho < 0.15$. The width of this region of phase coexistence is found to diminish as the value of σ is increased, and for σ as high as 1.5 no coexistence is observed, but K remains

²Although this curve is computed in this work at finite temperature, it retains its shape in the low temperature limit.

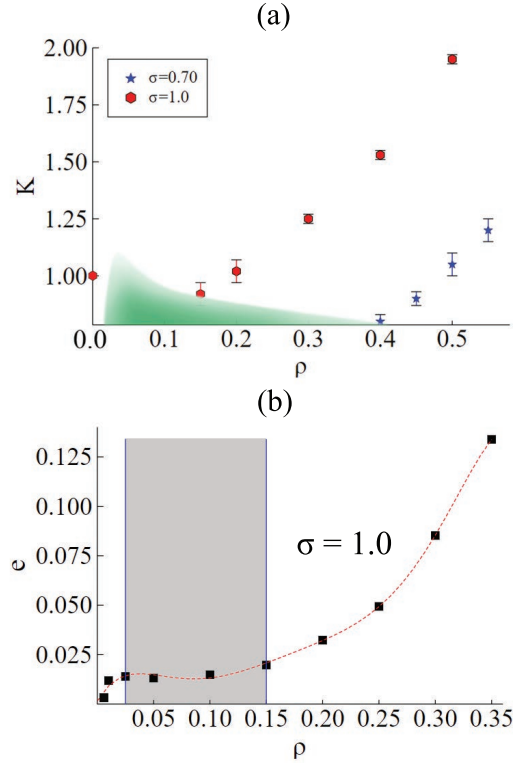


Figure 5.5: (a) The Tomonaga-Luttinger parameter of the system as a function of ρ for two values of $\sigma > \sigma_c$. The shaded area corresponds to the region of the phase diagram where phase coexistence occurs. The color gradient reflects the fact that the exact boundary of the green region was not precisely calculated. (b) Energy per particle $e(\rho)$ at $\sigma = 1$ as a function of the density. The shaded area corresponds to the range of densities where the system is found to feature phase coexistence. Statistical errors are smaller than size of the symbols.

above 1. This is illustrated in Fig. 5.5a, which features a roughly sketched shaded area corresponding to the speculated shape of the region of phase coexistence. It should be emphasized that we did not carry out a quantitative investigation of the boundaries of the region of phase coexistence, i.e., we are unable to say at what low density the system returns to a homogeneous, low-density gas phase, for a given value of σ . As a result, we have blurred out the boundary of the region of phase coexistence in Fig. 5.5a. The physics of such a dilute phase is expected to be amenable to a description in terms of a Tonks-Girardeau gas.

5.5 Conclusions

We carried out quantum Monte Carlo simulations of a system of spin zero dipolar particles in one dimension, with their dipole moments aligned along the direction of motion. The interaction also includes a hardcore, repulsive term (with a variable range σ), in order to ensure thermodynamic stability of the system against collapse. The phase diagram of the system is found to display considerably more richness with respect to the case previously investigated in previous works, with the dipoles aligned perpendicular to the direction of particle motion. In the latter case, the interaction is purely repulsive and the system has no self-bound regime, excluding the possibility of a quantum phase transition. Moreover, as reported in Ref. 37, the system with perpendicularly aligned dipoles has a value of K always above 1. Our system, on the other hand, features quasi-crystalline order at very low values of σ , and evolves into a non-superfluid liquid as σ grows. Beyond a critical value σ_c , inter-particle attraction is no longer sufficient to keep the system self-bound. Slightly above σ_c and on lowering the density, superfluidity may be achieved, albeit topologically unprotected and unstable against disorder. Further lowering the density results in gas-liquid phase coexistence. It is worth emphasizing that the investigation carried out here is not merely of academic interest, as the value of σ is experimentally tunable, and so our predictions are in principle testable in the laboratory. Obviously, important issues have to be taken into account as the 1D limit is approached. e.g., the importance of transverse modes.

Chapter 6

Dynamic structure factor of superfluid ${}^4\text{He}$ from quantum Monte Carlo: Maximum Entropy revisited

6.1 Introduction

We now shift our focus towards analytic continuation using the tools described in Sec. 2.5, and the inference of dynamical properties, specifically the dynamic structure factor. In recent years, the problem of extraction of the dynamic structure factor of superfluid ${}^4\text{He}$ from imaginary-time correlations computed by QMC has been independently revisited by two groups [137, 138], who proposed regularization schemes (RS) not making use of MaxEnt’s entropic prior. In both cases, their procedure essentially amounts to χ^2 -fitting¹, supplemented by averaging over a set of comparable images, in order to suppress some of the spurious structure that inevitably arises on carrying out χ^2 minimization in the presence of an ill-posed problem. Both works make the claim that their proposed approaches are superior to MaxEnt, in that the resulting images are sharper and in better agreement with experimental data.

In this chapter, we revisit the use of MaxEnt for the same problem, in order to assess quantitatively the claims made in Refs. [137, 138]. Specifically, we estimate the

¹The main difference between the approaches proposed in Ref. [137] and Ref. [138] is the numerical methodology adopted to identify the optimal image, i.e., to minimize the value of χ^2 .

dynamic structure factor $S(\mathbf{q}, \omega)$ for superfluid ^4He , by computing imaginary-time density correlations by QMC, and by using MaxEnt to carry out the inversion. The methodology we used is similar to that of Ref. [54], i.e., it consists of a Metropolis random walk in the space of spectral images, sampled from a probability density proportional to the standard maximum likelihood estimator, multiplied by the entropic prior (see Sec. 2.5). This procedure allows us to assign an uncertainty in the value of $S(\mathbf{q}, \omega)$, as the standard deviation of the values recorded for the different frequencies in the course of the random walk.

Compared to Ref. [54], the study presented here benefits from two decades of advances, both in computing hardware as well as in the QMC methodology utilized to generate the imaginary-time data. As a result, our statistical uncertainties are much smaller than those of the 1996 work, comparable to those of the data used in Refs. [137, 138], which is a necessary condition in order to carry out a meaningful and fair comparison. Based on the results presented here, we contend that MaxEnt does *not* prevent sharp features from appearing in the reconstructed spectral functions, as long as the accuracy of the QMC data justifies their inclusion. Indeed, the spectral images shown here are of comparable (or better) quality than those offered in Refs. [137, 138]. Ultimately, the sharpness of the spectral image almost exclusively hinges on the accuracy of the QMC data; by promoting smoothness, the entropic prior serves in our view a useful, noise-reducing purpose.

It is worth noting that a general scheme capable of tackling this kind of problem can be applied in other, rather different contexts, e.g., the determination of ground state expectation values in QMC transient estimate calculations [139]. These are typically carried out for Fermi systems, which are affected by the infamous “sign” problem, resulting in an exponential increase with imaginary time of the statistical error (see, for instance, Ref. [140]).

The remainder of this chapter is organized as follows: in section 6.2 we describe the model of the system and the QMC calculations carried out in this work, we present

and discuss our results in Sec. 6.3, and finally outline our conclusions in Sec. 6.4. For a detailed description of our inversion method, see 2.5.

6.2 Model and QMC Calculation

In this section we describe the QMC calculation of the imaginary-time correlation function which is then inverted to obtain the dynamic structure factor. The system is described as an ensemble of N point-like, identical particles with mass m equal to that of a He atom and with spin $S = 0$, thus obeying Bose statistics. It is enclosed in a cubic cell, with periodic boundary conditions in the three directions. The quantum-mechanical many-body Hamiltonian reads as follows:

$$\hat{H} = -\lambda \sum_i \nabla_i^2 + \sum_{i<j} v(r_{ij}) \quad (6.1)$$

where the first (second) sum runs over all particles (pairs of particles), $\lambda \equiv \hbar^2/2m = 6.0596415 \text{ K}\text{\AA}^2$, $r_{ij} \equiv |\mathbf{r}_i - \mathbf{r}_j|$ and $v(r)$ is a pair potential which describes the interaction between two atoms. We make use in this study of the accepted Aziz pair potential [141], which has been utilized in most simulation studies of superfluid helium. A more accurate model would also include interactions among triplets of atoms; however, published numerical work has given strong indications that three-body corrections have a relatively small effect on the structure and dynamics of the system, of interest here [104].

We carried out QMC simulations of the system described by eq. (6.1) at temperature $T = 1 \text{ K}$, using the continuous-space worm algorithm described in Ch. 2. The details of the simulation are standard; we adopted the usual the short-time approximation to the imaginary-time propagator accurate to fourth order in the time step $\delta\tau$ (see Ch. 2). All of the results presented here are extrapolated to the $\delta\tau \rightarrow 0$ limit; just like for other observables, the numerical estimates of the quantities of interest here, namely the imaginary-time correlation functions described below, computed with a value of the time step $\delta\tau = (1/640) \text{ K}^{-1}$ are indistinguishable from the extrapolated

ones, within the statistical uncertainties of the calculation.

Calculations were carried out at two different densities, namely $0.021834 \text{ \AA}^{-3}$, which is that at saturated vapor pressure (SVP) [6], and 0.0260 \AA^{-3} , which is very close to the freezing density (at a pressure of approximately 25 bars). All calculations were carried out at $T = 1 \text{ K}$. The experimental and theoretical data we compare our results against are at temperatures that range from 0 K to 1.3 K. All such temperatures are well below the lambda transition, and at that level the excitations are essentially independent of temperature (see, for instance, Refs. [67, 142]). We took advantage of space and time symmetry to improve statistics; a rough estimate of the statistical error on the generic value of $F(\mathbf{q}, \tau)$ is given by $5 \times 10^{-4} F(\mathbf{q}, 0)$.

The bulk of the results shown here was obtained on a system comprising $N = 64$ particles, a number which is not particularly large but that allows us to collect good statistics in a given simulation time; experience with previous work [54] suggests that this system size is sufficient to extract information at the wave vectors of interest here (see below). However, we have also repeated the simulation with $N = 256$ particles, and found no statistically significant difference in the values of $F(\mathbf{q}, \tau)$, within the statistical errors of our calculation.

$F(\mathbf{q}, 0) \equiv S_{\mathbf{q}}$ is known as the *static structure factor*, which is experimentally accessible and it is related via a Fourier transformation to the atomic pair correlation function. The values of $S_{\mathbf{q}}$ obtained here are in quantitative agreement with previous calculations, i.e., in excellent agreement with experiment (see Ref. [7]).

Typical results for $F(\mathbf{q}, \tau)$ are shown in Fig. 6.1; because $F(\mathbf{q}, \tau) = F(\mathbf{q}, \beta - \tau)$ (see, for instance, Ref. [88]), one need only compute this quantity in the $0 \leq \tau \leq \beta/2$ interval.

6.3 Results

Fig. 6.2 shows results for $S(\mathbf{q}, \omega)$ for the roton wave vector ($q = 1.963 \text{ \AA}^{-1}$) at $T = 1 \text{ K}$ and at saturated vapor pressure (SVP). Squares represent the values of \mathbf{S}_{\circ} defined

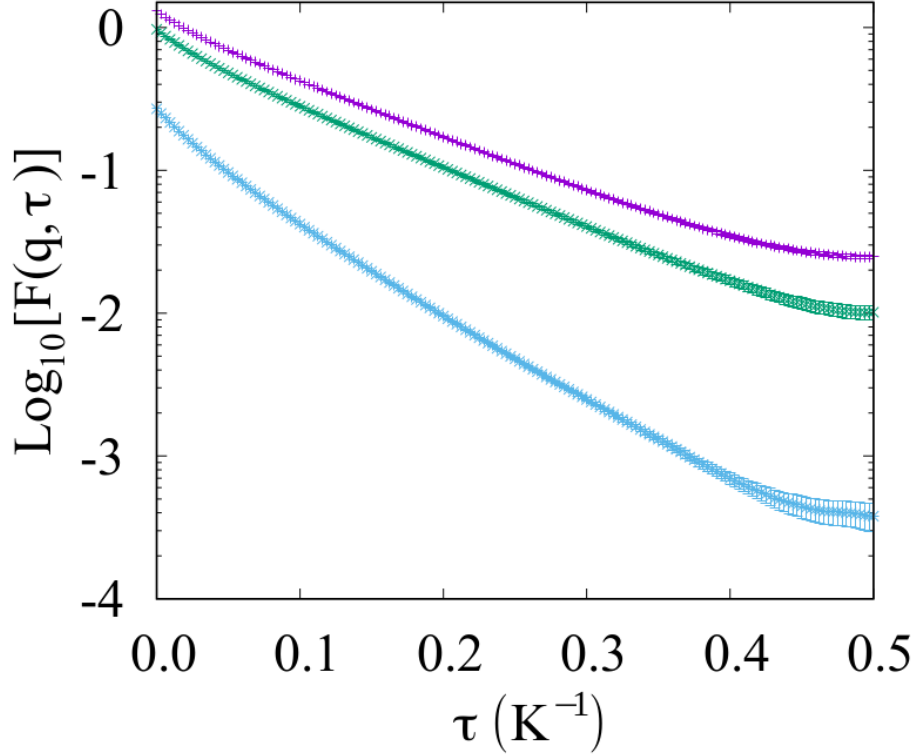


Figure 6.1: Typical $F(\mathbf{q}, \tau)$ results computed in a simulation of superfluid ${}^4\text{He}$ at $T = 1$ K at density $0.021834 \text{ \AA}^{-3}$. Results shown here are for the wave vectors $q = 1.075 \text{ \AA}^{-1}$ (bottom curve), $q = 1.756 \text{ \AA}^{-1}$ (middle curve) and $q = 1.964 \text{ \AA}^{-1}$ (top curve). When not shown, statistical errors are smaller than the size of the symbols.

through eq. 2.27, computed by means of the Monte Carlo Metropolis procedure described in Sec. 2.5. The statistical errors on the values of \mathbf{S}_o are smaller than the sizes of the symbols. Also shown in the figure are experimental data² from Ref. [66] at $T = 1.3$ K and for the wave vector $q = 1.90 \text{ \AA}^{-1}$. Agreement between theory and experiment seems fairly good; not only the position, but also the width of the peak is rather well reproduced, unlike in previous applications of MaxEnt [54]. This result shows that MaxEnt does not prevent the reconstructed spectral image from developing sharp features, if the quality of the underlying QMC data justifies their inclusion.

²We focus our presentation on the coherent part of the dynamic structure factor, because it is that which is physically more interesting, and also more challenging to recover. In general, the incoherent part of the spectrum yielded by our approach is in broad quantitative agreement with experiment.

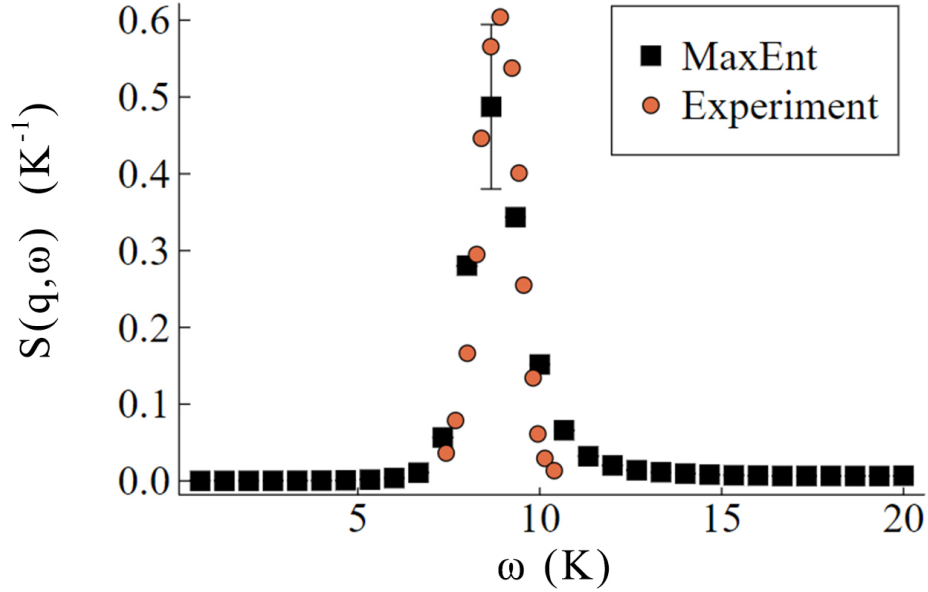


Figure 6.2: $S(\mathbf{q}, \omega)$ in superfluid ${}^4\text{He}$ at $T = 1$ K (at SVP) for the roton wave vector ($q = 1.963 \text{ \AA}^{-1}$), computed by inversion of QMC data based on MaxEnt (eq. 2.27, squares). Statistical errors on $S(\mathbf{q}, \omega)$ are smaller than the sizes of the symbols; the error bar on the square represents the *standard deviation* (see text), which has similar values for the two data points adjacent to the peak, and is comparable to, or smaller than, symbol sizes for all other data points. Circles show experimental data from Ref. [66] (only the coherent part is shown) at $T = 1.3$ K for the wave vector $q = 1.90 \text{ \AA}^{-1}$.

In the presence of greater statistical uncertainties, on the other hand, MaxEnt implies a more conservative choice, namely one in which smoother images are privileged.

As mentioned above, the statistical errors on \mathbf{S}_o are comparable to, or smaller than the sizes of the symbols, and can always be rendered negligible with modest computing resources. Obviously, however, the issue arises of assessing *systematic* errors, which are inherent to this image reconstruction problem. In other words, how far off can the optimal image \mathbf{S}_o be expected to be from the actual spectral function? The Metropolis procedure adopted here allows us to offer an estimate of that through the standard deviation of the values of \mathbf{S}_o for each and every value of the energy. In Fig. 6.2 we show one such standard deviation, corresponding to the energy interval ω_m in which \mathbf{S}_o takes on its highest value. Although not shown in the figure for clarity,

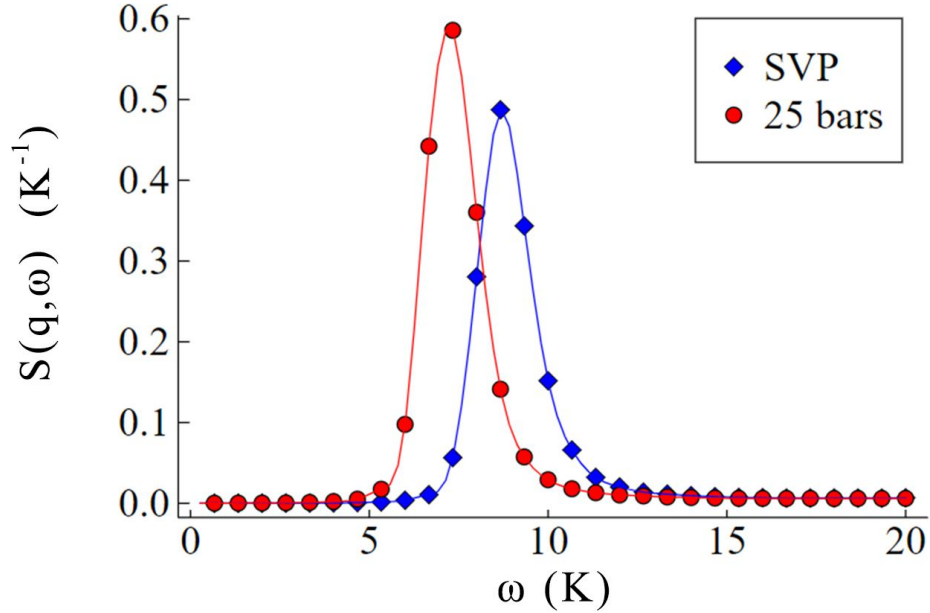


Figure 6.3: $S(\mathbf{q}, \omega)$, defined as \mathbf{S}_\circ (eq. 2.27) and computed as illustrated in the text, for superfluid ${}^4\text{He}$ at $T = 1$ K for the roton wave vector at SVP (diamonds, $q = 1.963 \text{ \AA}^{-1}$) and at 25 bars (circles, $q = 2.081 \text{ \AA}^{-1}$). Statistical errors on $S(\mathbf{q}, \omega)$ are comparable to the sizes of the symbols for both curves.

\mathbf{S}_\circ for the two energy intervals adjacent to ω_m have comparable standard deviations, whereas the standard deviation for all other values is much smaller (of the order of symbol sizes in Fig. 6.2). This is generally found to be the case, i.e., the (typically relatively few) values of \mathbf{S}_\circ for which it is most important, are affected by the largest uncertainty. Thus, at least for the roton wave vector MaxEnt yields a reasonably accurate estimate of the position and the width of the peak, with some remaining uncertainty regarding its height.

It is interesting to note that, despite the uncertainty, nevertheless relative comparisons of data obtained with the procedure illustrated here are still meaningful. For example, Fig. 6.3 shows $S(\mathbf{q}, \omega)$ for the roton wave vector at two different pressures, namely SVP and 25 bars. The roton minimum shifts from $\sim 1.9 \text{ \AA}^{-1}$ at SVP to $\sim 2.1 \text{ \AA}^{-1}$ at 25 bars [143]. Our results show that the position of the peak moves to lower energy and the peak itself gains strength, in remarkable quantitative agreement with

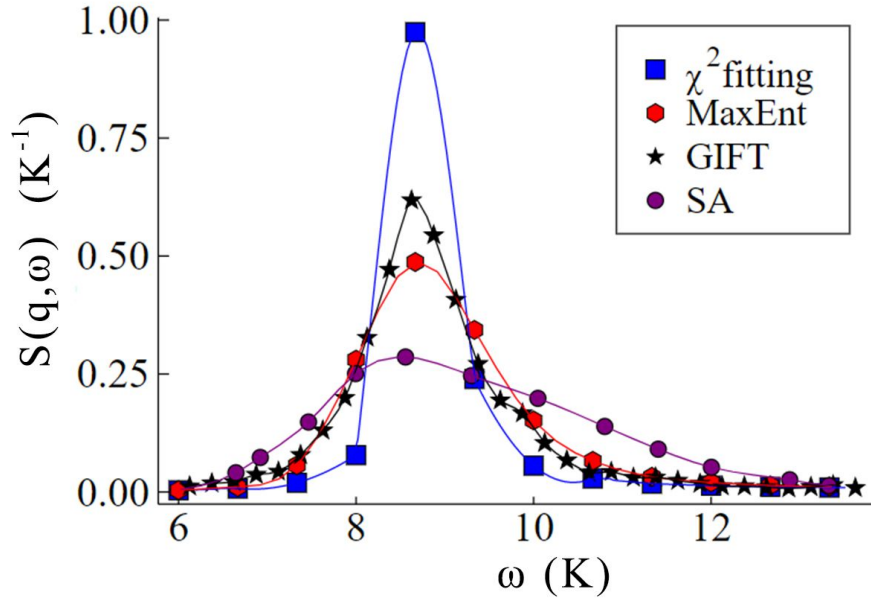


Figure 6.4: $S(\mathbf{q}, \omega)$ in superfluid ${}^4\text{He}$ for the roton wave vector ($q = 1.963 \text{ \AA}^{-1}$) calculated through the inversion of QMC data based on four different methods. Hexagons show the result of the inversion using MaxEnt (eq. 2.27), whereas squares show that with $\alpha = 0$ (which amounts to standard χ^2 fitting). Stars show the result of the inversion using GIFT [137] for the wave vector $q = 1.977 \text{ \AA}^{-1}$ at $T = 0 \text{ K}$. Dark circles show the result of χ^2 -minimization using simulated annealing (SA) [138] for the wave vector $q = 1.91 \text{ \AA}^{-1}$ at $T = 0.8 \text{ K}$.

experimental observation [67].

In Fig. 6.4, we compare our results with those of other authors who made use of different approaches (not based on MaxEnt) to tackle the inversion of QMC data.³ The wave vectors are not identical but are reasonably close to the roton minimum in all cases; all calculations are carried out in the low temperature limit (see caption of Fig. 6.4 for details). There is nearly perfect agreement between our image and that of Ref. [137], especially if the standard deviation of our result is taken into account. On the other hand, the spectral image obtained in Ref. [138] is much broader, with a significantly lower peak. It is interesting to compare these curves with that arising from χ^2 -fitting carried out in the context of our procedure, namely by simply setting

³Data from Ref. [137] were supplied by D. E. Galli, private communication. Data from Ref. [138] were read off Figs. 4 and 7 therein.

$\alpha = 0$. In this case, the average value of χ^2 is $\sim 0.2 L$, i.e., slightly lower than that obtained with finite α . However, as can be seen in Fig. 6.4, the peak is significantly higher (in fact its height exceeds that of the experimental result by almost a factor two) and also narrower than what is observed experimentally. This is consistent with the general notion that “brute force” χ^2 minimization, while yielding sharp features, is all too likely to result in unphysical behavior. The use of the entropic prior emphasizes the contribution from smoother images (still consistent with the QMC data), which in this case results in better agreement with experiment.

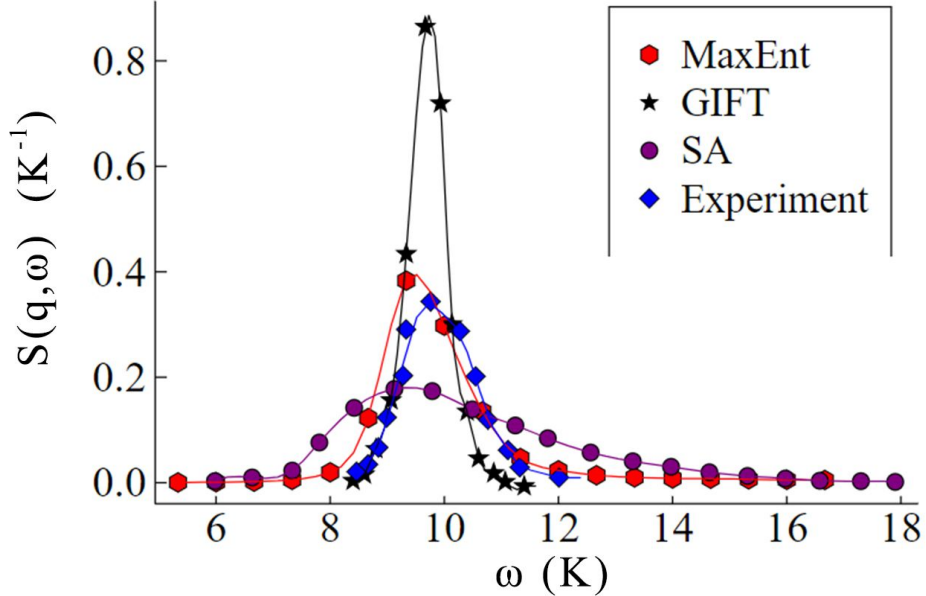


Figure 6.5: $S(\mathbf{q}, \omega)$ in superfluid ${}^4\text{He}$ for the wave vector $q = 1.756 \text{ \AA}^{-1}$ calculated through the inversion of QMC data based on three different methods. Hexagons show the result of the inversion using MaxEnt (eq. 2.27). Stars show the result of the inversion using GIFT [137] for the wave vector $q = 1.755 \text{ \AA}^{-1}$ at $T = 0 \text{ K}$. Dark circles show the result of χ^2 -minimization using simulated annealing (SA) [138] for the wave vector $q = 1.76 \text{ \AA}^{-1}$ at $T = 1.2 \text{ K}$. Diamonds show experimental data from Ref. [66] (only the coherent part is shown) at $T = 1.3 \text{ K}$ for the wave vector $q = 1.70 \text{ \AA}^{-1}$.

Let us now consider a second wave vector, namely $q = 1.756 \text{ \AA}^{-1}$. In Fig. 6.5, we compare again the result of our MaxEnt inversion with those of Refs. [137, 138], as well as experimental data from Ref. [66]. Our procedure yields a spectral image

in much closer agreement with experiment than the other two. In particular, both the shape of the curve and the location of the main peak are in excellent agreement with experiment, taking into account the slight difference in wave vectors [144] and the resolution of our spectral image. On the other hand, the spectral image reported in Ref. [138] is once again much too broad compared to the experimentally observed one, while that of Ref. [137] is considerably sharper.

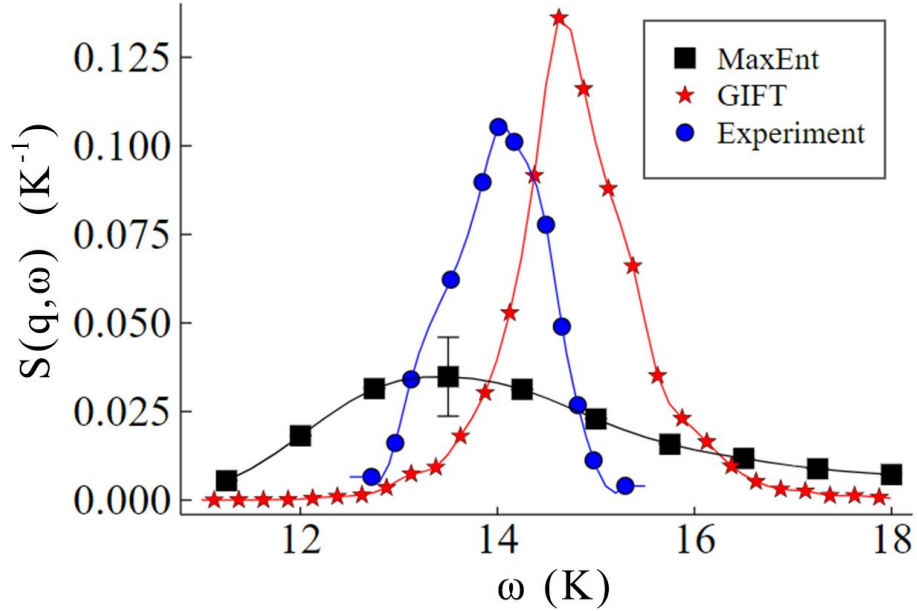


Figure 6.6: $S(\mathbf{q}, \omega)$ in superfluid ${}^4\text{He}$ for the maxon wave vector ($q = 1.075 \text{ \AA}^{-1}$). Squares show the result calculated through the inversion of QMC data based on MaxEnt (eq. 2.27). Stars show the result of the inversion using GIFT [137, 145], calculated for the wave vector $q = 1.107 \text{ \AA}^{-1}$ at $T = 0 \text{ K}$. Circles show experimental data from Ref. [66] (only the coherent part is shown) at $T = 1.3 \text{ K}$ for the wave vector $q = 1.10 \text{ \AA}^{-1}$. Statistical errors are of the order of the symbol sizes. The error bar on the square data point close to the peak represents a typical standard deviation.

Finally, let us examine results at a third wave vector, namely $q = 1.075 \text{ \AA}^{-1}$, which corresponds to the maxon. In this case, our spectral image features a single peak, which is however nowhere near as sharp as in the experimentally observed dynamic structure factor [66], as shown in Fig. 6.6. The considerably greater difficulty in extracting sharp features for this wave vector is a direct consequence of the behavior

in imaginary time for $F(\mathbf{q}, \tau)$, namely the much faster decay in the maxon case (Fig. 6.1). Indeed, we find that the difficulty of reconstructing $S(\mathbf{q}, \omega)$ from QMC data is particularly severe for wave vectors near the maxon. For our procedure to recover sharp features at this wave vector, it appears that the underlying QMC data should possess errors that are significantly smaller than those which we could achieve within this project. This illustrates the difficulty of an a priori, even semi-quantitative assessment of the required precision of the QMC data.

Interestingly, the procedure illustrated in Ref. [137] does yield a sharp peak in this case as well, of width comparable to that of the experimental image, and $\sim 30\%$ greater height (data from Ref. [138] for this wave vector were not available). However, the position of the peak itself is off, compared to experiment, by roughly as much as that estimated by MaxEnt (in the case of GIFT the peak is detected at higher energy). Thus, although the shape of the GIFT image is certainly closer to the experimental result, in quantitative terms (e.g., position of the peak and area in the experimentally observed peak region), a comparison between the two results may not be so straightforward; in particular, one ought to think of situations in which this procedure is to be used in a *predictive* way, i.e., no experimental data are available for comparison.

Thus, we conclude that for this particular wave vector the precision required in the QMC data, in order to achieve a spectral image reconstruction of quality comparable to that of the other two wave vectors, is significantly greater than that afforded by the computational resources available to this project. It is incorrect to attribute the lack of sharpness of the reconstructed spectral image in this case to the inversion scheme utilized, which proves equally or more effective than the alternatives at other wave vectors.

6.4 Conclusions

We have revisited the use of MaxEnt to extract the dynamic structure factor of superfluid ^4He from imaginary-time density correlation functions computed by QMC. This method was first applied to this problem over two decades ago, yielding results that were deemed “only qualitatively interesting”, as the sharper features of the experimentally measured spectra were not fully recovered. In recent years, alternative schemes [137, 138] have been proposed to tackle the same problem; although they are based on different numerical optimization strategies, these schemes ultimately amount to χ^2 -fitting.

We adopted in this work a procedure similar to that first proposed in Ref. [54], i.e, we performed a random walk in the space of spectral images, using the entropic prior in the context of “classic” MaxEnt. Our study benefits from the availability of new QMC data obtained using state-of-the-art techniques and obviously far more powerful computing resources than those available two decades ago. The accuracy of our QMC data is, to the best of our determination, comparable to that of the data used in Refs. [137, 138].

Our spectral images are of quality at least comparable (and often superior) to that of those yielded by the methods proposed in Refs. [137, 138]. In particular, spectral images provided in Ref. [138] are too broad, and compare poorly to experiment, whereas those of Ref. [137] are at times much sharper than the experimental ones.

We showed that the use of the entropic prior does *not* cause the reconstructed spectral images to be unphysically smooth and featureless. Rather, it is the precision of the underlying QMC data that determines by itself whether the reconstructed spectra should display sharp peaks or not. In general, the elimination of the entropy from the inversion process indeed promotes sharper features, but we argue that that often comes at the expense of accuracy, as such sharpness is ultimately not warranted by the data. This means that some sharp features might appear at incorrect locations,

or even be downright spurious. One is therefore left with no real justification to choose a “sharper” over a more conservative, smoother image, if both are consistent with the data (*a posteriori* validation based on agreement with available experiments for one particular physical system being a dubious criterion to compare different methodologies).

Chapter 7

Roton Excitation in Overpressurized Superfluid ^4He

7.1 Introduction

In Ch. 6, we demonstrated the effectiveness of Maximum Entropy (MaxEnt) as a technique for the inference of the dynamic structure factor from QMC data, at least in the roton region of the excitation spectrum of superfluid ^4He . Inspired by this conclusion, we applied this technique to more extensively study the roton excitation in superfluid ^4He and its overpressurized metastable phases.

We report in this chapter the results of a theoretical investigation of overpressurized superfluid ^4He , carried out by means of first principle QMC simulations at temperature $T = 1$ K. The goal of this QMC study is to examine the structural and superfluid properties of the metastable superfluid phase at very high pressures, as well as to calculate the energy associated to the roton minimum of the elementary excitation spectrum. We accomplish this by computing imaginary-time correlation functions, and converting them to real-frequency spectral functions through an inverse Laplace transform, relying on MaxEnt as our regularization scheme of choice.

Our main result is that the energy of the roton excitation vanishes at a density $\rho_{sp} = 0.0320(2) \text{ \AA}^{-3}$. This is also the highest density for which the simulation of a metastable, overpressurized superfluid phase of ^4He is feasible, as spontaneous crystallization rapidly occurs at higher density, not allowing us to collect meaningful

statistics. We can therefore identify ρ_{sp} with the spinodal density, in agreement with the hypothesis of Ref. [64]. The pressure corresponding to ρ_{sp} is equal to 104 bars, to be compared to that (67 bars) of the equilibrium crystalline phase at the same density.

We report estimates for the condensate fraction n_0 as a function of the density, and we find them to be in quantitative agreement with previous ground state studies, up to a pressure of approximately 60 bars; significant deviations are observed from the previously predicted exponential decay, at higher pressure, i.e., the condensate fraction decays considerably more rapidly with density. Analogously, the computed superfluid fraction ρ_S remains relatively close to 100% as the density is increased, but falls off abruptly on approaching ρ_{sp} .

The remainder of this chapter is organized as follows: in section 7.2 we describe the model of the system; in Sec. 7.3 we describe our QMC methodology; we present and discuss our results in Sec. 7.4 and finally outline our conclusions in Sec. 7.5.

7.2 Model

We model the system as an ensemble of N point-like, identical particles with mass m equal to that of a ^4He atom and with spin $S = 0$, thus obeying Bose statistics. The system is enclosed in a cubic cell of volume V with periodic boundary conditions in the three directions. The density of the system is $\rho = N/V$. The quantum-mechanical many-body Hamiltonian reads as follows:

$$\hat{H} = -\lambda \sum_i \nabla_i^2 + \sum_{i<j} v(r_{ij}) \quad (7.1)$$

where the first (second) sum runs over all particles (pairs of particles), $\lambda \equiv \hbar^2/2m = 6.06 \text{ K\AA}^2$, $r_{ij} \equiv |\mathbf{r}_i - \mathbf{r}_j|$ and $v(r)$ denotes the pairwise interaction between the helium atoms. In this investigation, we model this interaction using the well-established Aziz pair potential [141], which is the canonical model utilized in most numerical studies

of superfluid helium. This pair-wise potential affords an accurate reproduction of the equation of state of condensed helium in the range of densities considered in this work. To put it more quantitatively, three-body terms, which provide the leading correction to the interaction, are estimated to contribute no more than 1-2% of the pressure, at or below 100 bars. Their effect on structural and dynamical properties is negligible [104, 146].

7.3 Calculation

As mentioned above, we carried out QMC simulations of the system described by eq. (7.1), using the continuous-space worm algorithm described in Ch. 2. The details of the QMC simulation are standard; we adopted the usual the short-time approximation for the imaginary-time propagator accurate to fourth order in the time step $\delta\tau$ (see Ch. 2). All of the results presented here are extrapolated to the limit of vanishing $\delta\tau$. The numerical estimates of the quantities of interest computed with $\delta\tau = 1.6 \times 10^{-3} \text{ K}^{-1}$ are indistinguishable from the extrapolated ones, within the statistical uncertainties of the calculation. The results shown here were obtained for systems comprising $N = 256$ particles. Experience with previous work [54] suggests that this system size is sufficient to extract information at the roton wave vector, of interest here.

All calculations were carried out at $T = 1 \text{ K}$. For densities up to freezing, such a value of the temperature is well below the superfluid transition temperature T_c , and therefore our physical estimates may be expected to approach closely ground state values. For example, the excitation spectrum of the system is experimentally observed to be essentially independent of temperature, in this range of density (see, for instance, Refs. [67, 142]). On the other hand, at higher density, in the overpressurized metastable regime, this is no longer guaranteed, as pressurization is expected to suppress T_c (there are no experimental data nor theoretical estimates of which we are aware).

The properties of the system are studied as a function of the density; below the freezing density ρ_f , equal to $\sim 0.0262 \text{ \AA}^{-3}$, simulations are straightforward, as one is studying the thermodynamic equilibrium phase. On the other hand, above the freezing and melting density ($\rho_m \sim 0.0286 \text{ \AA}^{-3}$), the system starts displaying a marked tendency to crystallize, and an appropriate simulation protocol has to be adopted in order to prevent that from happening too quickly, in order to accumulate enough statistics for the metastable, homogeneous superfluid phase. We adopted the same protocol as in Ref. [110], i.e., we increase the density of the system in steps, by rescaling all particle coordinates (i.e., along imaginary-time world lines [82]) in a many-particle configuration coming from a simulation at a slightly lower density (the immediately previous step).

The advantage of this approach is that one is starting from configurations that are already “entangled”, i.e., they feature permutations of large numbers of particles. In order to reach the crystalline, equilibrium phase, the simulation algorithm must “disentangle” all of these world lines, and although this will of course eventually happen, the metastable phase may be sufficiently “long-lived” (in the computer) that one may still arrive at physically meaningful expectation values. Of course, there will always be a drift in the averages over the course of the simulation, as the true equilibrium phase inevitably emerges, but in most cases it is small enough not to be a concern.

In order to study the elementary excitations of the system, one can estimate the dynamic structure factor $S(\mathbf{q}, \omega)$, by calculating by QMC the imaginary-time correlation function $F(\mathbf{q}, \tau)$ defined through eq. 2.23. As explained previously, the inversion constitutes a mathematically ill-posed problem, and hence we rely again on MaxEnt to obtain the position of the main peak of $S(\mathbf{q}, \omega)$ (i.e., the energy of the excitation dominating the spectrum) as a function of density.

In this work, we have not attempted the full reconstruction of the spectral image $S(\mathbf{q}, \omega)$ as a function of the wave vector \mathbf{q} , in order to obtain the energy dispersion curve $\omega(\mathbf{q})$, thereby identifying the position of the roton minimum for each and every

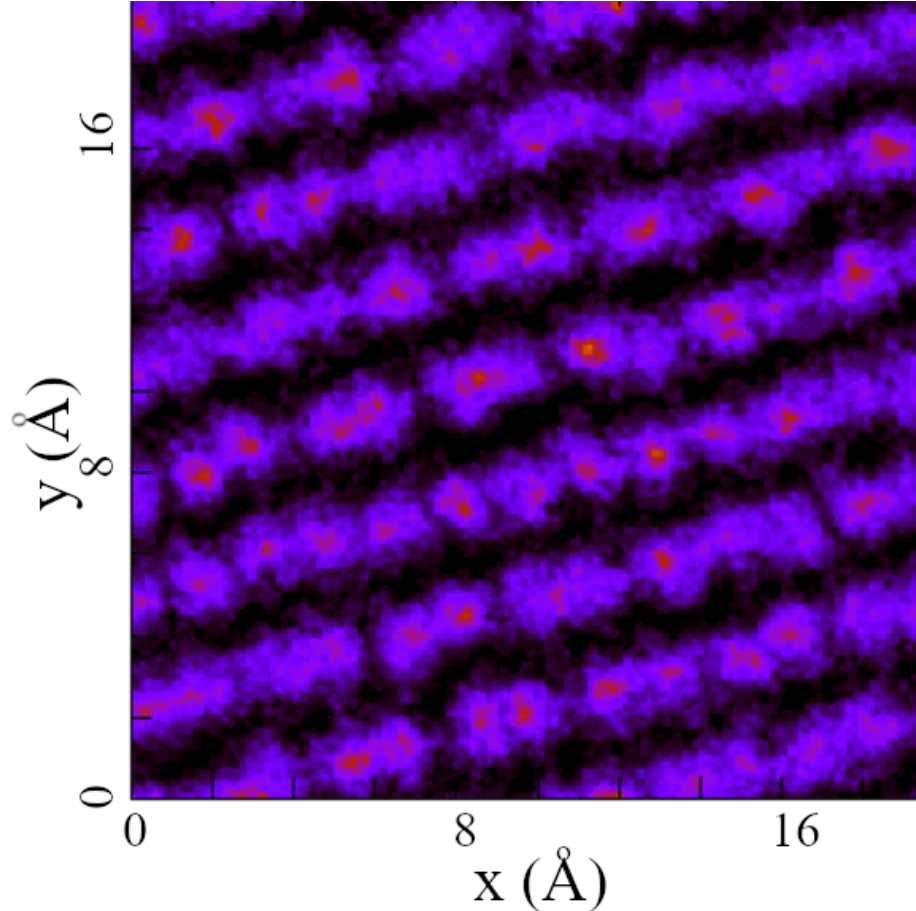


Figure 7.1: Instantaneous density map of a system of $N = 256$ ${}^4\text{He}$ atoms (view is along the z direction) in a cubic box, at $T = 1$ K and density 0.0336 \AA^{-3} . Clearly, in this case the system has crystallized.

one of the densities considered. Rather, we have focused for simplicity on a single wave vector for each density, assuming that the magnitudes of the roton wave vectors q, q' at two different densities ρ and ρ' be related through $(q'/q) = (\rho'/\rho)^{1/3}$, as is experimentally found to be the case for the equilibrium superfluid phase below freezing [143].

As mentioned above, since we are using an equilibrium simulation technique, on simulating the system for a sufficiently long time eventually crystalline order is bound to emerge. It is therefore necessary to monitor the simulation in order to ensure that one is actually studying a metastable superfluid phase, and that crystal order has not yet set in. This is accomplished first and foremost by visual inspection of the

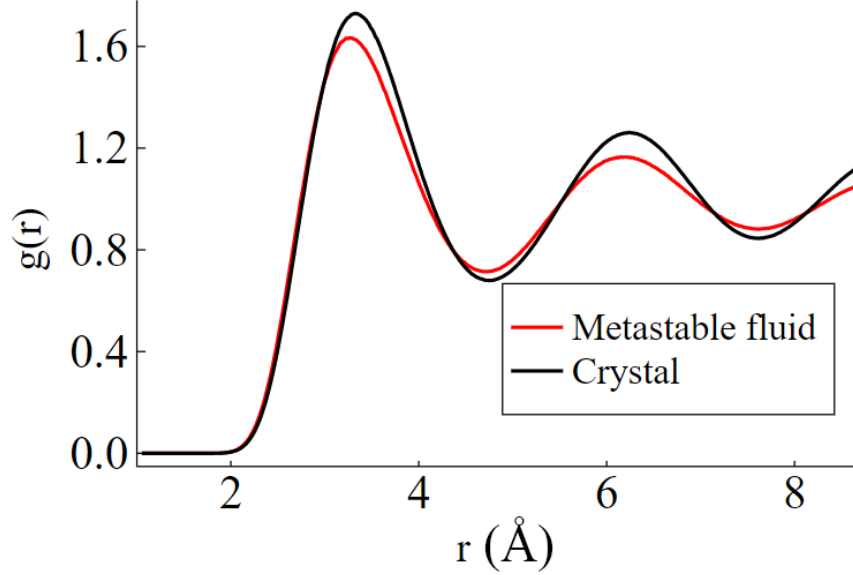


Figure 7.2: Pair correlation function of ${}^4\text{He}$ at $T = 1$ K and a density of $\rho = 0.0319$ \AA^{-3} , for both the metastable superfluid and the equilibrium (*hcp*) crystalline phase (darker curve).

many-particle configurations (i.e., imaginary-time paths) generated in the course of the simulation. As shown in Fig. 7.1, it is possible to detect the appearance of order rather easily, as it sets in even if the geometry of the box (cubic) is not specifically designed to accommodate a crystal of the known equilibrium structure (*hcp* in the case of ${}^4\text{He}$). Another way to monitor the appearance of crystalline order is through the calculation of the pair correlation function, and the comparison with that (computed separately) of the equilibrium crystalline phase at the same density. An example of this is shown in Fig. 7.2; although the two functions follow one another quite closely, that of the crystal has noticeably higher peaks.

Another important indicator that one is simulating a metastable superfluid phase, besides of course the value of the superfluid fraction (ρ_S), which is computed through the well-established winding number estimator [80], is the one-body density matrix $n(r)$, which is expected to plateau at long distances in a superfluid, while decaying exponentially in a crystal.

7.4 Results

In this section, we present our results for structural, superfluid, and dynamical properties of the overpressurized metastable phase of ^4He .

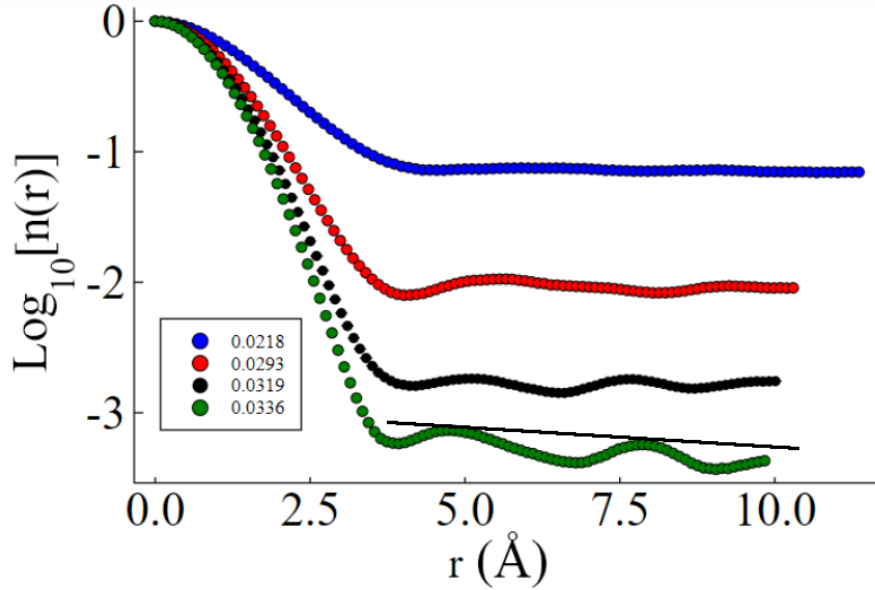


Figure 7.3: One-body density matrix of the metastable liquid phase of ^4He at $T = 1$ K and at various increasing densities (higher density shown by lower curve). The lowest density for which results are shown is the equilibrium density, the highest (bottom curve) 0.0336 \AA^{-3} . The straight line through the peaks of the bottom curve illustrates the consistency of the data with exponential decay.

Fig. 7.3 shows the one-body density matrix $n(r)$ for a few different densities explored in this work. The lowest density for which results are shown is the equilibrium density, $\rho_{eq} = 0.021834 \text{ \AA}^{-3}$. For the highest density, namely 0.0336 \AA^{-3} , data are consistent with an exponential decay, suggesting that this density is above the spinodal. For all other densities, $n(r)$ plateaus at long distances to a value corresponding to the condensate fraction n_0 .

Fig. 7.4 shows our results for the condensate fraction as a function of density, comparing them with those for the ground state, obtained in Ref. [62]. The results of the two calculations are in perfect agreement, i.e., consistent with an exponential decay of the condensate fraction with density. However, in this work we considered

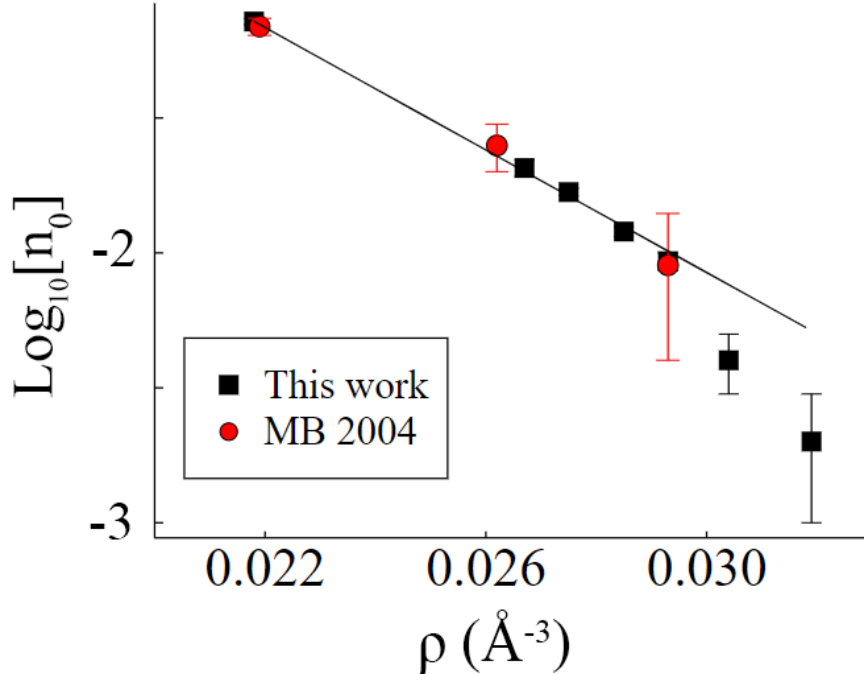


Figure 7.4: Condensate fraction (n_0) of the metastable liquid phase of ^4He at $T = 1$ K, as a function of density (squares). Also shown are the ground state estimates of Ref. [62] (circles).

densities $\sim 15\%$ higher than in Ref. [62]; the data shown in Fig. 7.4 show significant deviations from the exponential decay, i.e., the condensate fraction decays more rapidly on approaching ρ_{sp} . Assuming that our statistical and systematic errors are not significantly underestimated (we believe this to be unlikely), one possibility [147] to account for such deviations is that T_c may be substantially suppressed, as the density approaches ρ_{sp} , and therefore the comparison of our results with ground state estimates may be complicated by thermal effects.

The suppression of T_c is corroborated by the values of the superfluid fraction, reported in Fig. 7.5. As one can see, while ρ_S depends very weakly on ρ , remaining relatively large up to the highest density considered in Ref. [62] (0.0293 \AA^{-3} , corresponding to a pressure of approximately 60 bars), it decays abruptly above it, barely reaching $\sim 10\%$ at the highest density for which a metastable superfluid phase can be simulated, using our protocol, namely 0.0319 \AA^{-3} .

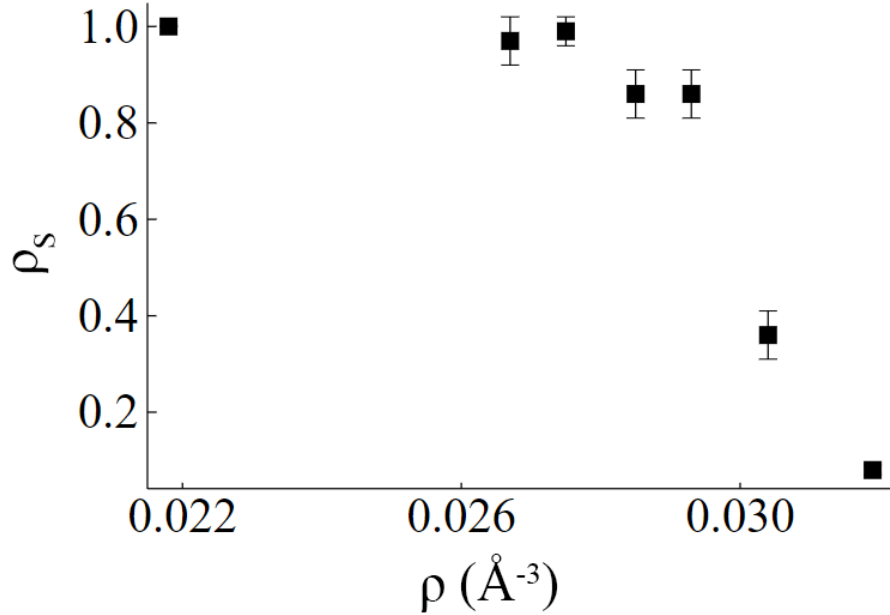


Figure 7.5: The superfluid fraction of the metastable fluid phase of ${}^4\text{He}$ at $T = 1$ K, as a function of density.

We report in Table 7.1 values of the superfluid and condensate fraction, as well as computed pressure (in bars) for two different densities. Also shown for comparison are the values of the pressure for the corresponding equilibrium (crystalline *hcp*) phase, obtained separately in this work. As expected, the pressure is considerably higher for the metastable superfluid phase.

Next, we discuss the results for $S(q_R, \omega)$, which constitute the most important part of this study (q_R is the magnitude of the roton wave vector). Fig. 7.6 shows our results for $S(q_R, \omega)$, inferred through the MEM for the metastable superfluid phase at three different densities, including the equilibrium density ρ_{eq} defined above. The results for the two higher densities are for two overpressurized superfluid phase.

All of the curves feature a well-defined maximum, whose position corresponds to the energy of the excitation. We estimate the position of the peak and assign a statistical uncertainty following the procedure outlined in Ref. [148]. Namely, we perform a Metropolis Monte Carlo simulation in the space of spectral images and accumulate statistics on the position of the maximum of the curve, also obtaining

ρ (\AA^{-3})	Superfluid			<i>hcp</i>
	ρ_s	n_0	P	P
0.0293	0.86(5)	0.0090(5)	62.0(3)	32.2(2)
0.0304	0.36(5)	0.0040(5)	71.4(9)	45.2(3)
0.0319	0.08(1)	0.0020(4)	96(1)	67.1(7)

Table 7.1: Superfluid (ρ_s) and condensate fraction (n_0), as well as the computed value of the pressure (P , in bars) for metastable superfluid ${}^4\text{He}$ at $T = 1$ K at different densities above the melting density. Statistical errors (in parentheses) are on the last digit. Also shown for comparison is the computed pressure for the equilibrium crystalline (*hcp*) phase.

the uncertainty of its position as the standard deviation. As expected, and as shown in Fig. 7.7, the roton energy goes down as a function of density. In addition, the height of the peak grows as one approaches the spinodal density, and the onset of crystallization.

In Fig. 7.7, we map out the roton energy as a function of density, $\omega_R(\rho)$. In order to estimate the density at which $\omega_R = 0$, we make the assumption that that occurs in concomitance with the divergence of the static structure factor, consistently with Bijl-Feynman theory of the elementary excitations [86]. This leads us to posit the following form [64]:

$$\omega_R(\rho) = A(\rho_{sp} - \rho)^\gamma \quad (7.2)$$

We use this expression to fit the data in Fig. 7.7, using A , ρ_{sp} and the unknown exponent γ as fitting parameters. This yields $\rho_{sp} = 0.0320(2) \text{\AA}^{-3}$, with a value of the critical exponent $\gamma = 0.12(5)$. This is consistent with the observed instability of the simulated fluid phase at $\rho = 0.0336 \text{\AA}^{-3}$, and yields a value of approximately 100 bars for the upper limit to which the superfluid phase can be overpressurized.

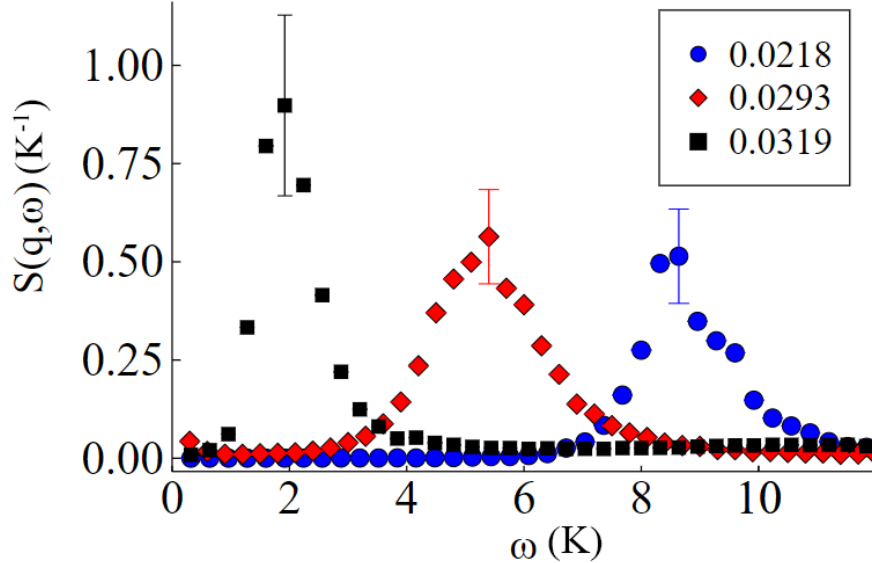


Figure 7.6: The dynamic structure factor $S(\mathbf{q}, \omega)$ of superfluid ${}^4\text{He}$ at $T = 1$ K, evaluated at densities of ρ_{eq} ($q_R = 1.963 \text{ \AA}^{-1}$, circles), $\rho = 0.0293 \text{ \AA}^{-3}$ ($q_R = 2.159 \text{ \AA}^{-1}$, diamonds), and $\rho = 0.0319 \text{ \AA}^{-3}$ ($q_R = 2.219 \text{ \AA}^{-1}$, squares). The standard deviation associated with the inversion process is shown only for the peaks of the curves, with the understanding that the adjacent points have comparable or smaller standard deviations.

7.5 Conclusions

We presented state-of-the-art QMC results for metastable superfluid phases of ${}^4\text{He}$, pressurized above melting, at a temperature $T = 1$ K. These metastable phases can be rendered stable in a computer simulation (and presumably in Nature as well [4, 111]) by the presence of long cycles of exchange of ${}^4\text{He}$ atoms, acting to prevent particles from becoming localized in space. This confers to the simulated metastable phase an appreciable “lifetime” (i.e., in the computer), that allows the meaningful measurement of physical observables.

The condensate fraction in the metastable overpressurized superfluid phase decays as a function of density, in a way that is consistent with the exponential decay predicted in previous ground state studies [62], up to a pressure of approximately 67 bars; concurrently, the superfluid fraction remains relatively close to 100%. At higher pressures, not explored in previous calculations, we find that both the condensate

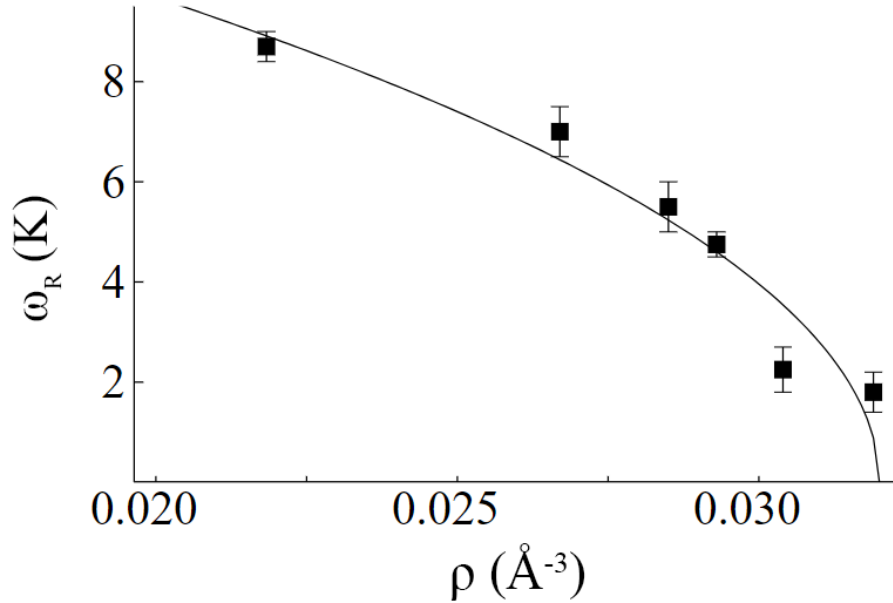


Figure 7.7: The roton energy of superfluid ${}^4\text{He}$ as a function of density, at $T = 1$ K.

and superfluid fractions decay more rapidly. This suggests that the superfluid transition temperature, relatively unaffected by pressure in the equilibrium superfluid phase, and even in the overpressurized phase for pressures below ~ 67 bars, becomes strongly suppressed at higher pressure.

We computed the energy of the roton excitation in the overpressurized superfluid phase, as a function of density. Our results are consistent with the hypothesis [64] that the roton energy should vanish at the spinodal density ρ_{sp} , in correspondence to a pressure of approximately 100 bars. Above such a pressure, an overpressurized superfluid phase is unstable against crystallization.

The results of our study open up the possibility of more detailed experimental investigations of the overpressurized metastable liquid phases of helium, including in confined geometries. While the high pressures studied here are not necessarily directly measurable in some experimental settings such as nanoporous media, the roton energies that we compute are indeed measurable through neutron scattering techniques. The results we present here could therefore allow an indirect estimate of the local pressure of a metastable sample of overpressurized superfluid.

Chapter 8

Conclusions

In this thesis, we presented the results of a number of investigations in which we utilized first-principle computer simulations to study a wide variety of Bose systems. We explored the phases of matter that emerge, the familiar among them (gases, liquids, solids), and the exotic (Bose-Einstein condensates, superfluids, and supersolids). We studied the transitions between these phases and the excitations that underlie them, as well as the connections between the microscopic physics and the macroscopic phenomena that arise as a result. These investigations are enabled by the exceedingly powerful toolbox of quantum Monte Carlo, which allows us to compute numerically exact estimates of thermodynamic quantities and structural correlations at finite temperature.

We started by considering a broad albeit simple class of Bose systems that is characterized by a central pairwise interaction with hardcore repulsion and a long attractive tail. We mapped out a universal phase diagram that encapsulates a wide spectrum of such physical systems that vary in their degree of quantumness. The classical regime is descriptive of most natural substances, which crystallize at absolute zero temperature. As the systems get more quantum, one encounters a transition to an intermediate regime in which the systems fail to crystallize at zero temperature, forming instead a superfluid phase. Finally, a third regime is found beyond the point of quantum unbinding, which describes systems that are unbound at zero tempera-

ture, such as ultracold gases. We studied the evolution of the pressure-temperature phase diagram as we went from one extreme to the other.

In the phase diagram of the hypothetical isotope ^5He , we encountered an intriguing phenomenon which we did not explore deeply enough. While the true ground state of such a system is indeed a crystal, we found evidence of a metastable over-pressurized superfluid phase at the equilibrium density. It is also distinct from the situation in ^4He , explored extensively in Ch. 7, where the metastable superfluid phases are realizable at densities significantly higher than the equilibrium density. No evidence of such a phase was found deeper into the classical regime, i.e., for systems like ^6He , ^8He , and parahydrogen, which suggests that this behavior is unique to the systems that lie close to the solid-liquid boundary in Fig. 3.3. This phase is potentially long-lived, and could be the subject of a future study that explores it in greater depth.

This broad class of Lennard-Jones systems was shown to be filled with a variety of rich physics, and to feature phases ranging from solids to normal fluids to superfluids and gases. Motivated by the search for the more exotic supersolid phase, we also studied systems of dipolar particles with aligned dipole moments. These systems were speculated to be candidates for the realization of simultaneous crystalline and superfluid order due to the unique nature of the inter-particle interaction, which is long-ranged and anisotropic in character. We studied the phase diagram of the bulk system in three dimensions, which indeed featured a supersolid phase sandwiched between an insulating crystal and a hard sphere-like superfluid. We also studied the system in 1D within the framework of Luttinger Liquid Theory, in the previously unexplored case in which the dipoles are aligned parallel to the direction of particle motion. The latter study revealed a rich phase diagram compared to the thoroughly investigated case in which the dipoles are aligned perpendicular to the direction of particle motion.

There are multiple avenues of future work related to the study of these dipolar systems. Our three-dimension study was limited to the ground state of the bulk sys-

tem, so it would be interesting, for instance, to investigate the relationship between the melting temperature and the superfluid transition temperature across the super-solid regime. Another avenue to explore would be dipolar systems under confinement and investigating the effect of trap geometry on the physics, which is not currently well-understood. Another object of great interest is the self-bound dipolar droplet, how its geometry evolves as a function of the number of particles and the scattering length, and how it connects to the bulk physics.

Finally, we addressed the problem of analytic continuation and the extraction of real-time behavior. Our QMC methodology allowed us to compute correlations in imaginary time, from which real-time dynamical information may, in principle, be inferred through an inverse Laplace transform. This is an ill-posed problem in the presence of the inevitable statistical uncertainties associated with the QMC calculation. We utilized Maximum Entropy as our choice of regularization scheme to extract the dynamical structure factor, and we compared this method to others proposed in the literature, as well as to experimental data. After establishing the effectiveness of this technique in the presence of high quality QMC data, we applied it to study the roton excitation in overpressurized ^4He as we probed the limits of the metastable liquid phase. Our predictions of the vanishing of the roton excitation were consistent with a previously proposed hypothesis.

The problem of analytic continuation of imaginary time data is still far from solved. Maximum Entropy, our method of choice, relies on the quality of the QMC data being sufficiently high. Indeed, in the maxon region of the excitation spectrum, where density correlations decay rapidly in imaginary time, the extracted spectral image is much too broad compared to the experimental result. A future study seeking a precise construction of the full excitation spectrum would therefore need to address this problematic region, either through brute force reduction of the QMC errors by the utilization of greater computational resources, or through some other means.

The studies presented here constitute a journey through a number of quantum

many-body systems filled with a wide range of physical behavior, enabled by a remarkably effective and accurate numerical framework. We have utilized our ability to control the physical conditions to which these simulated systems are subject in order to study how their behavior becomes increasingly exotic as quantum effects are made increasingly prominent. Thus we contribute to mankind's understanding of the relationship between the bizarre quantum nature of reality and the classical picture familiar to our intuitions, and how the latter emerges as a limiting case of the former. Thus we cast a glimmer of light into the great dark that lies beyond the boundary of enlightenment.

Bibliography

- [1] V. F. Weisskopf, “About Liquids,” *Trans. N. Y. Acad. Sci.*, vol. 38, pp. 202–218,
- [2] P. A. M. Dirac, *Proc. Royal Soc. London. A*, vol. 123, pp. 714–733, 1929.
- [3] R. P. Feynman, *Phys. Rev.*, vol. 91, pp. 1291–1301, 1953.
- [4] M. Boninsegni, L. Pollet, N. Prokof’ev, and B. Svistunov, *Phys. Rev. Lett.*, vol. 109, p. 025 302, 2012.
- [5] J. Wilks, *The Properties of Liquid and Solid Helium*. New York: Oxford University Press, 1967.
- [6] R. J. Donnelly and C. F. Barenghi, *J. Phys. Chem. Ref. Data*, vol. 27, p. 1217, 1998.
- [7] D. M. Ceperley, *Rev. Mod. Phys.*, vol. 67, p. 279, 1995.
- [8] M. Boninsegni, *Phys. Rev. Lett.*, vol. 111, p. 235 303, 2013.
- [9] M. Boninsegni and N. V. Prokof’ev, *Rev. Mod. Phys.*, vol. 84, pp. 759–776, 2012.
- [10] M. Wenzel, F. Böttcher, T. Langen, I. Ferrier-Barbu, and T. Pfau, *Phys. Rev. A*, vol. 86, p. 053 630, 2017.
- [11] L. Chomaz, R. M. W. van Bijnen, D. Petter, G. Faraoni, S. Baier, J. H. Becher, M. J. Mark, F. Wächtler, L. Santos, and F. Ferlino, *Nature Physics*, vol. 14, p. 442, 2018.
- [12] F. Cinti, P. Jain, M. Boninsegni, A. Micheli, P. Zoller, and G. Pupillo, *Phys. Rev. Lett.*, vol. 105, p. 135 301, 2010.
- [13] M. Boninsegni, *J. Low Temp. Phys.*, vol. 168, pp. 137–149, 2012.
- [14] F. Cinti and M. Boninsegni, *Phys. Rev. A*, vol. 96, p. 013 627, 2017.
- [15] T. Lahaye, C. Menotti, L. Santos, M. Lewenstein, and T. Pfau, *Rep. Prog. Phys.*, vol. 72, p. 126 401, 2009.
- [16] A. Griesmaier, J. Werner, S. Hensler, J. Stuhler, and T. Pfau, *Phys. Rev. Lett.*, vol. 94, p. 160 401, 2005.
- [17] M. Lu, N. Q. Burdick, S. H. Youn, and B. L. Lev, *Phys. Rev. Lett.*, vol. 107, p. 190 401, 2011.

- [18] K. Aikawa, A. Frisch, M. Mark, S. Baier, A. Rietzler, R. Grimm, and F. Ferlaino, *Phys. Rev. Lett.*, vol. 108, p. 210 401, 2012.
- [19] A. de Paz, A. Sharma, A. Chotia, E. Maréchal, J. Huckans, P. Pedri, L. Santos, O. Gorceix, L. Vernac, and B. Laburthe-Tolra, *Phys. Rev. Lett.*, vol. 111, p. 185 305, 2013.
- [20] K.-K. Ni, S. Ospelkaus, M. H. G. de Miranda, A. Peér, B. Neyenhuis, J. J. Zirbel, S. Kotochigova, P. S. Julienne, D. S. Jin, and J. Ye, *Science*, vol. 322, p. 231, 2008.
- [21] B. Yan, S. A. Moses, B. Gadway, J. P. Covey, K. R. A. Hazzard, A. M. Rey, D. S. Jin, and J. Ye, *Nature (London)*, vol. 501, p. 521, 2013.
- [22] T. Takekoshi, L. Reichsöllner, A. Schindewolf, J. M. Hutson, C. R. Le Sueur, O. Dulieu, F. Ferlaino, R. Grimm, and H.-C. Nägerl, *Phys. Rev. Lett.*, vol. 113, p. 205 301, 2014.
- [23] J. W. Park, S. A. Will, and M. W. Zwierlein, *Phys. Rev. Lett.*, vol. 114, p. 205 302, 2015.
- [24] J. B. Balewski, A. T. Krupp, A. Gaj, S. Hofferberth, R. Löw, and T. Pfau, *New J. Phys.*, vol. 16, p. 063 012, 2014.
- [25] C. J. Pethik and H. Smith, *Bose-Einstein Condensation in Dilute Gases*. Cambridge: Cambridge University Press, 2005.
- [26] I. Ferrier-Barbut, H. Kadau, M. Schmitt, M. Wenzel, and T. Pfau, *Phys. Rev. Lett.*, vol. 116, p. 215 301, 2016.
- [27] M. Schmitt, M. Wenzel, F. Böttcher, I. Ferrier-Barbut, and T. Pfau, *Nature (London)*, vol. 539, p. 259, 2016.
- [28] L. Chomaz, S. Baier, D. Petter, M. J. Mark, F. Wächtler, L. Santos, and F. Ferlaino, *Phys. Rev. X*, vol. 6, p. 041 039, 2016.
- [29] A. Trautmann, P. Ilzhöfer, G. Durastante, C. Politi, M. Sohmen, M. J. Mark, and F. Ferlaino, *Phys. Rev. Lett.*, vol. 121, p. 213 601, 2018.
- [30] S. Ronen, D. C. E. Bortolotti, and J. L. Bohn, *Phys. Rev. Lett.*, vol. 98, p. 030 406, 2007.
- [31] D. Edler, C. Mishra, F. Wächtler, R. Nath, S. Sinha, and L. Santos, *Phys. Rev. Lett.*, vol. 119, p. 050 403, 2017.
- [32] R. Oldziejewski, W. Gorecki, K. Pawlowski, and K. Rzazewski, *Phys. Rev. A*, vol. 97, p. 063 617, 2018.
- [33] See, for instance, *The Many-Body Problem*, edited by D. C. Mattis (World Scientific, Singapore, 1993).
- [34] Y. Vekhov and R. B. Hallock, *Phys. Rev. Lett.*, vol. 109, p. 045 303, 2012.
- [35] Y. Vekhov, W. J. Mullin, and R. B. Hallock, *Phys. Rev. Lett.*, vol. 113, p. 035 302, 2014.

- [36] M Boninsegni, A. B. Kuklov, L. Pollet, N. V. Prokof'ev, B. V. Svistunov, and M. Troyer, *Phys. Rev. Lett.*, vol. 99, p. 035 301, 2007.
- [37] R. B. Hallock and Y. H. Kahng, *J. Low Temp. Phys.*, vol. 134, p. 21, 2004.
- [38] G. Stan, M. Gatica S.and Boninsegni, S. Curtarolo, and M. W. Cole, *Am. J. Phys.*, vol. 67, p. 1170, 1999.
- [39] J. R. Beamish, A. Hikata, L. Tell, and C. Elbaum, *Phys. Rev. Lett.*, vol. 50, p. 425, 1983.
- [40] E. Krotscheck and M. D. Miller, *Phys. Rev. B*, vol. 60, p. 13 038, 1999.
- [41] M. Boninsegni and S. Moroni, *J. Low Temp. Phys.*, vol. 118, p. 1, 2000.
- [42] A. Del Maestro, M. Boninsegni, and I. Affleck, *Phys. Rev. Lett.*, vol. 106, p. 105 303, 2011.
- [43] L. Vranješ Markić, H. Vrcan, Z. Zuhrianda, and H. R. Glyde, *Phys. Rev. B.*, vol. 97, p. 014 513, 2018.
- [44] T. Omiyinka and M. Boninsegni, *Phys. Rev. B.*, vol. 93, p. 104 501, 2016.
- [45] M. Boninsegni, S.-Y. Lee, and V. H. Crespi, *Phys. Rev. Lett.*, vol. 86, p. 3360, 2001.
- [46] S. Saccani, S. Moroni, and M. Boninsegni, *Phys. Rev. Lett.*, vol. 108, p. 175 301, 2012.
- [47] A Papoulis, *Probability and Statistics*. New York: Prentice Hall, 1990.
- [48] M. Jarrel and J. Gubernatis, *Phys. Rep.*, vol. 269, pp. 133–195, 1996.
- [49] R. N. Silver, J. E. Gubernatis, D. S. Sivia, and M. Jarrell, *Phys. Rev. Lett.*, vol. 65, p. 496, 1990.
- [50] S. R. White, *Phys. Rev. B*, vol. 44, p. 4670, 1991.
- [51] M. Makivić and M. Jarrell, *Phys. Rev. Lett.*, vol. 68, p. 1770, 1992.
- [52] N. Bulut, D. J. Scalapino, and S. R. White, *Phys. Rev. Lett.*, vol. 72, p. 705, 1994.
- [53] R Preuss, A. Muramatsu, W. von der Linden, P. Dieterich, F. F. Assaad, and W. Hanke, *Phys. Rev. Lett.*, vol. 73, p. 732, 1994.
- [54] M. Boninsegni and D. M. Ceperley, *J. Low Temp. Phys.*, vol. 104, p. 339, 1996.
- [55] A. W. Sandvik, *Phys. Rev. B*, vol. 57, p. 10 287, 1998.
- [56] O. F. Syljuåsen, *Phys. Rev. B*, vol. 78, p. 174 429, 2008.
- [57] A. S. Mishchenko, N. V. Prokof'ev, A. Sakamoto, and B. V. Svistunov, *Phys. Rev. B*, vol. 62, p. 6317, 2000.
- [58] D. R Reichman and E. Rabani, *J. Chem. Phys.*, vol. 131, p. 054 502, 2009.
- [59] S. Fuchs, T. Pruschke, and M. Jarrell, *Phys. Rev. E*, vol. 81, p. 056 701, 2010.
- [60] F. Caupin, S. Balibar, and H. J. Maris, *Physica B: Condens. Matter*, vol. 329–333, pp. 356–359, 2003.

- [61] F. Werner, G. Beaume, A. Hobeika, S. Nascimbène, C. Herrmann, F. Caupin, and S. Balibar, *J. Low Temp. Phys.*, vol. 136, pp. 93–116, 2004.
- [62] S. Moroni and M. Boninsegni, *J. Low Temp. Phys.*, vol. 136, pp. 129–137, 2004.
- [63] T. Schneider and C. P. Enz, *Phys. Rev. Lett.*, vol. 27, pp. 1186–1188, 1971.
- [64] P. Nozières, *J. Low Temp. Phys.*, vol. 142, pp. 91–99, 2006.
- [65] H. Glyde, *Excitations in Liquid and Solid Helium*. CRC Press, 1994.
- [66] K. H. Andersen, W. G. Stirling, R. Scherm, A. Stunault, B. Fak, H. Godfrin, and A. J. Dianoux, “Coherent excitations in liquid ^4He : I. experiment and presentation of data,” *J. Phys.: Condens. Matter*, vol. 6, p. 821, 1994.
- [67] M. R. Gibbs, K. H. Andersen, W. G. Stirling, and H. Schober, *J. Phys.: Condens. Matter*, vol. 11, p. 603, 1999.
- [68] E. Molz, A. P. Y. Wong, M. H. W. Chan, and J. R. Beamish, *Phys. Rev. B*, vol. 48, pp. 5741–5750, 1993.
- [69] *Phys. Rev. Lett.*, vol. 101, p. 025 301, 2008.
- [70] H. R. Glyde, *Rep. Prog. Phys.*, vol. 81, p. 014 501, 2018.
- [71] A. Leggett, *Phys. Rev. Lett.*, vol. 25, p. 1543, 1970.
- [72] J. Toulouse, R. Assaraf, and C. Umrigar, *Chapter fifteen - introduction to the variational and diffusion monte carlo methods*, P. E. Hoggan and T. Ozdogan, Eds., 2016.
- [73] U. Schollwöck, *Rev. Mod. Phys.*, vol. 77, 259–315, 2005.
- [74] R. P. Feynman, *Rev. Mod. Phys.*, vol. 20, pp. 367–387, 1948.
- [75] N. Metropolis, N. Rosenbluth, A. W. Rosenbluth, A. H. Teller, and E. Teller, *J. Chem. Phys.*, vol. 21, pp. 1087–1092, 1953.
- [76] R. P. Feynman and A. R. Hibbs, *Quantum Mechanics and Path Integrals*. New York: McGraw-Hill, 1965, ch. 10.
- [77] M. Boninsegni, *J. Low Temp. Phys.*, vol. 141, pp. 27–46, 2005.
- [78] S. Chin, *Phys. Lett. A*, vol. 226, p. 344, 1997.
- [79] S. Jang, S. Jang, and G. A. Voth, *J. Chem. Phys.*, vol. 115, p. 7832, 2001.
- [80] E. L. Pollock and D. M. Ceperley, *Phys. Rev. B*, vol. 36, pp. 8343–8352, 1987.
- [81] M. Boninsegni, N. V. Prokof’ev, and B. V. Svistunov, *Phys. Rev. Lett.*, vol. 96, p. 070 601, 2006.
- [82] M. Boninsegni, N. V. Prokof’ev, and B. V. Svistunov, *Phys. Rev. E*, vol. 74, p. 036 701, 2006.
- [83] F. Mezzacapo and M. Boninsegni, *Phys. Rev. Lett.*, vol. 97, p. 045 301, 2006.
- [84] F. Mezzacapo and M. Boninsegni, *Phys. Rev. A*, vol. 75, p. 033 201, 2007.
- [85] L. D. Landau, *J. Phys. USSR*, vol. 5, p. 71, 1941.

- [86] R. P. Feynman, *Phys. Rev.*, vol. 94, p. 262, 1954.
- [87] R. P. Feynman and M. Cohen, *Phys. Rev.*, vol. 102, p. 1189, 1956.
- [88] S. W. Lovesey, *Condensed matter physics : dynamic correlations*. Menlo Park, California: Benjamin/Cummings, 1986.
- [89] H. Flyvbjerg and H. G. Petersen, *J. Chem. Phys.*, vol. 91, p. 461, 1989.
- [90] E. T. Jaynes, *Phys. Rev.*, vol. 106, p. 620, 1957.
- [91] J. De Boer, *Physica*, vol. 14, pp. 139–148, 1948.
- [92] M. Dusseault and M. Boninsegni, *Phys. Rev. B*, vol. 95, p. 104518, 2017.
- [93] M. Boninsegni, *Phys. Rev. Lett.*, vol. 111, p. 205303, 2013.
- [94] P. O. Egan, “Muonic Helium,” in *Atomic Physics 7*, D. Kleppner and F. M. Pipkin, Eds., New York: Plenum Press, 1981, pp. 373–384.
- [95] H. Masaki, H. Aghai-Khozani, A. Sótér, A. Dax, and D. Barna, *Nature*, vol. 581, pp. 37–41, 2020.
- [96] T. Tajima, *Muon Cat. Fusion*, vol. 1, p. 257, 1987.
- [97] J. A. Wheeler, “Nanosecond matter,” in *Energy in Physics, War and Peace: A Festschrift Celebrating Edward Teller’s 80th Birthday*, H. Mark and L. Wood, Eds., Dordrecht, The Netherlands: Kluwer, 1988, ch. 10, pp. 266–290.
- [98] D. T. Son, M. Stephanov, and H.-U. Yee, *The phase diagram of ultra quantum liquids*, 2020. arXiv: 2006.01156 [cond-mat.quant-gas].
- [99] L. H. Nosanow, L. J. Parish, and F. J. Pinski, *Phys. Rev. B*, vol. 11, pp. 191–204, 1975.
- [100] M. D. Miller, L. H. Nosanow, and L. J. Parish, *Phys. Rev. B*, vol. 15, pp. 214–229, 1977.
- [101] A. Cuccoli, A. Macchi, V. Tognetti, and R. Vaia, *Phys. Rev. B*, vol. 47, pp. 14923–14931, 1993.
- [102] M. H. Müser, P. Nielaba, and K. Binder, “Path-integral Monte Carlo study of crystalline Lennard-Jones systems,” *Phys. Rev. B*, vol. 51, pp. 2723–2731, 1995.
- [103] M. Takahashi and M. Imada, *J. Phys. Soc. Japan*, vol. 53, pp. 3871–3877, 1984.
- [104] S. Moroni, F. Pederiva, S. Fantoni, and M. Boninsegni, *Phys. Rev. Lett.*, vol. 84, p. 2650, 2000.
- [105] R. K. Pathria and P. D. Beale, *Statistical Mechanics*, Third. Boston: Academic Press, 2011, ch. 12.
- [106] R. Aziz, V. Nain, J. Carley, W. Taylor, and G. McConville, *J. Chem. Phys.*, vol. 70, pp. 4330–4342, 1979.
- [107] F. Gómez and J. Sesma, *Eur. Phys. J. D*, vol. 66, p. 6, 2012.

- [108] W. Zwerger, *J. Stat. Mech. Theory Exp.*, vol. 2019, p. 103 104, 2019.
- [109] P. M. A. Mestrom, V. E. Colussi, T. Secker, G. P. Groeneveld, and S. J. J. M. F. Kokkelmans, *Phys. Rev. Lett.*, vol. 124, p. 143 401, 2020.
- [110] M. Boninsegni, *Phys. Rev. B*, vol. 97, p. 054 517, 2018.
- [111] M. Boninsegni, N. Prokof'ev, and B. Svistunov, *Phys. Rev. Lett.*, vol. 96, p. 105 301, 2006.
- [112] E. Grilly and R. Mills, *Ann. Phys. (N.Y.)*, vol. 8, pp. 1–23, 1959.
- [113] K.-O. Ng and D. Vanderbilt, *Phys. Rev. B*, vol. 52, p. 2177, 1995.
- [114] B. Spivak and S. A. Kivelson, *Phys. Rev. B*, vol. 70, p. 155 114, 2004.
- [115] S. Flügge, *Practical Quantum Mechanics*. Berlin: Springer-Verlag, 1971.
- [116] S. Saccani, S. Moroni, and M. Boninsegni, *Phys. Rev. B*, vol. 83, p. 092 506, 2011.
- [117] D. Petter, G. Natale, R. M. W. van Bijnen, A. Patscheider, M. J. Mark, L. Chomaz, and F. Ferlaino, *Phys. Rev. Lett.*, vol. 122, p. 183 401, 2019.
- [118] L. Tanzi, E. Lucioni, F. Famá, J. Catani, A. Fioretti, C. Gabbanini, R. N. Bisset, L. Santos, and G. Modugno, *Phys. Rev. Lett.*, vol. 122, p. 130 405, 2019.
- [119] F. Böttcher, J.-N. Schmidt, M. Wenzel, J. Hertkorn, M. Guo, T. Langen, and T. Pfau, *Phys. Rev. X*, vol. 9, p. 011 051, 2019.
- [120] L. Chomaz, D. Petter, P. Ilzhöfer, G. Natale, A. Trautmann, C. Politi, G. Durastante, R. M. W. van Bijnen, A. Patscheider, M. Sohmen, M. J. Mark, and F. Ferlaino, *Phys. Rev. X*, vol. 9, p. 021 012, 2019.
- [121] S. M. Roccuzzo and F. Ancilotto, *Phys. Rev. A*, vol. 99, 041601(R), 2019.
- [122] S. Sinha and L. Santos, *Phys. Rev. Lett.*, vol. 99, p. 140 406, 2007.
- [123] R. Citro, E. Orignac, S. De Palo, and M. L. Chiofalo, *Phys. Rev. A*, vol. 75, 051602(R), 2007.
- [124] F. Deuretzbacher, J. C. Cremon, and S. M. Reimann, *Phys. Rev. A*, vol. 81, p. 063 616, 2010.
- [125] T. Roscilde and M. Boninsegni, *New. J. Phys.*, vol. 12, p. 033 032, 2010.
- [126] L. Guan, X. Cui, R. Qi, and H. Zhai, *Phys. Rev. A.*, vol. 89, p. 023 604, 2014.
- [127] Y. Kora and M. Boninsegni, *J. Low Temp. Phys.*, vol. 197, p. 337, 2019.
- [128] J. M. Schurer, P. Schmelcher, and A. Negretti, *Phys. Rev. A.*, vol. 90, p. 033 601, 2014.
- [129] F. D. M. Haldane, *Phys. Rev. Lett.*, vol. 47, p. 1840, 1981.
- [130] M. A. Cazalilla, *J. Phys. B: At. Mol. Opt. Phys.*, vol. 37, S1, 2004.
- [131] G. L. Warren and R. J. Hinde, *Phys. Rev. E*, vol. 73, p. 056 706, 2006.
- [132] M. Boninsegni and S. Moroni, *Phys. Rev. E*, vol. 86, p. 056 712, 2012.

- [133] M. Boninsegni, *Phys. Rev. Lett.*, vol. 87, p. 087 201, 2001.
- [134] G. Bertaina, M. Motta, M. Rossi, E. Vitali, and D. E. Galli, *Phys. Rev. Lett.*, vol. 116, p. 135 302, 2016.
- [135] G. E. Astrakharchik and J. Boronat, *Phys. Rev. B*, vol. 90, p. 235 439, 2014.
- [136] M. Ruggeri, S. Moroni, and M. Boninsegni, *Phys. Rev. Lett.*, vol. 111, p. 045 303, 2013.
- [137] E. Vitali, M. Rossi, L. Reatto, and D. E. Galli, *Phys. Rev. B*, vol. 82, p. 174 510, 2010.
- [138] G. Ferré and J. Boronat, *Phys. Rev. B*, vol. 93, p. 104 510, 2016.
- [139] M. Caffarel and D. M. Ceperley, *J. Chem. Phys.*, vol. 97, p. 8415, 1992.
- [140] M. Boninsegni and E. Manousakis, *Phys. Rev. B*, vol. 46, p. 560, 1992.
- [141] R. Aziz, V. P. S. Nain, J. S. Carley, W. L. Taylor, and G. T. McConville, *J. Chem. Phys.*, vol. 70, p. 4330, 1979.
- [142] O. Dietrich, E. Graf, C. Huang, and L. Passell, *Phys. Rev. A*, vol. 5, p. 1377, 1972.
- [143] J. V. Pearce and H. R. Glyde, *J. Low Temp. Phys.*, vol. 138, p. 37, 2005.
- [144] R. J. Donnelly, J. A. Donnelly, and R. N. Hills, *J. Low Temp. Phys.*, vol. 44, p. 471, 1981.
- [145] Data from Ref. [137] were supplied by D. E. Galli, private communication. Data from Ref. [138] were read off Figs. 4 and 7 therein.
- [146] M. Boninsegni, C. Pierleoni, and D. M. Ceperley, *Phys. Rev. Lett.*, vol. 72, pp. 1854–1857, 1994.
- [147] F. Caupin and S. Balibar, “Quantum statistics of metastable liquid helium,” in *Liquids Under Negative Pressure*, Springer, 2002, pp. 201–214.
- [148] Y. Kora and M. Boninsegni, *Phys. Rev. B*, vol. 98, no. 13, 2018.